Frequency conversion in two-dimensional photonic structures

Ljubiša Babić

Frequency conversion
in
two-dimensional photonic structures

PROEFSCHRIFT

ter verkrijging van
de graad van Doctor aan de Universiteit Leiden,
op gezag van Rector Magnificus prof. mr. P. F. van der Heijden,
volgens besluit van het College voor Promoties
te verdedigen op dinsdag 17 mei 2011
klokke 13:45 uur

door

Ljubiša Babić

geboren te Dubrovnik, Croatia
in 1982

Promotiecommissie:

Promotor:	Prof. Dr. J. P. Woerdman	Universiteit Leiden
Copromotor:	Dr. M. J. A. de Dood	Universiteit Leiden
Leden:	Prof. Dr. J. Gómez Rivas	Technische Universiteit Eindhoven
	Prof. Dr. H. W. M. Salemink	Technische Universiteit Delft
	Dr. Ir. T. H. Oosterkamp	Universiteit Leiden
	Prof. Dr. D. Bouwmeester	Universiteit Leiden
		en University of California
		at Santa Barbara (UCSB)
	Prof. Dr. E. R. Eliel	Universiteit Leiden
	Prof. Dr. J. M. van Ruitenbeek	Universiteit Leiden

An electronic version of this dissertation is available at the Leiden University Repository (https://openaccess.leidenuniv.nl).

Casimir PhD series, Delft-Leiden 2011-10

S ljubavlju mojim roditeljima,
Nikolini i Nedeljku

With love to my parents,
Nikolina and Nedeljko

Contents

x

CHAPTER 1

Introduction

1.1 Photonic structures

Photonic structures that show features on a wavelength or even subwavelength scale are widespread in nature. For example, the wings of *Morpho* butterflies, the scales of the Brazilian beetle *Lamprocyphus augustus*, and opal gemstones all derive their iridescent colors from variations in the refractive index on a microscopic scale, comparable to the wavelength of visible light. The shimmering blue color of the *Morpho* butterfly, the sparkling green color of the Brazilian beetle, and attractive iridescent colors of an opal gemstone are to a large extent produced by their internal structure, not by pigments [1–3]. Over the course of millions of years, life has evolved to make nanostructures of astonishing complexity that exhibit striking optical properties [4]. Slowly, but with great determination, human beings are catching up with Nature by artificially creating nanostructures with wavelength and subwavelength feature sizes in materials with a high refractive index.

1.1.1 Photonic crystals

In 1987, Eli Yablonovitch [5] and Sajeev John [6], independent from each other, proposed a novel type of periodic photonic structures called photonic crystals to control the propagation of light. Yablonovitch proposed to inhibit spontaneous emission of an atom placed inside these structures, while John predicted that photonic crystals can be used to localize light in three dimensions.

The first photonic crystals were made on centimeter length scales [7] for experimental investigation in the microwave region. Later on, using semiconductor fabrication techniques to structure material on a scale of hundreds of nanometers, photonic crystals operating at near-infrared wavelengths

(800–900 nm) were realized [8]. Today, photonic crystals are recognized as structures that can tailor the propagation of light in a unique way and provide enhanced light-matter interaction. As such, photonic crystals find application in lasers, single photon emitters, waveguides, filters, frequency convertors, nonlinear switches, sensors, and slow-light media [9–11].

Propagation of light in a photonic crystal is analogous to the propagation of electrons in a semiconductor crystal. Figure 1.1(a) shows constructive interference of light waves reflected from a one-dimensional periodic structure with a spatial period a. For an appropriate frequency of light ω, the reflected waves from all the interfaces are in phase and the interference is constructive, similar to Bragg reflection of X-rays from a crystalline solid [12]. When this Bragg condition is met, light is totally reflected, and it cannot propagate through the structure. For a realistic photonic structure with a finite index contrast the Bragg peaks are significantly broadened and form frequency ranges for which the propagation of light in the periodic structure is forbidden in a particular direction. These forbidden gaps, called photonic stop gaps or photonic band gaps, can be described by a photonic band structure.

Figure 1.1(b) shows the photonic band structure (frequency ω as a function
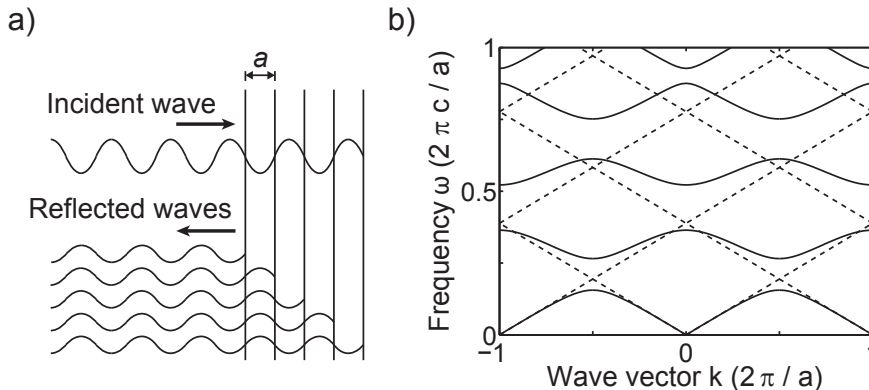
Figure 1.1. (a) Constructive interference of light waves reflected from a one-dimensional periodic structure, with a spatial period a. For an appropriate choice of frequency ω and periodicity a, the reflected waves from each interface are in phase and the total reflection adds up to unity. (b) Photonic band structure (solid lines) for light propagating along the direction of periodicity in a one-dimensional photonic crystal, a multilayer structure. The dashed lines indicate dispersion relation for a homogenous dielectric with a refractive index equal to the effective refractive index of the photonic crystal ($\omega = ck/n_{eff}$).

of the wave vector k) for light waves propagating through a one-dimensional photonic crystal along the direction of periodicity. The structure has a spatial period a and consists of alternating layers of materials with refractive indices of $n_1 = 1$ (air) and $n_2 = 3.5$, and equal thicknesses $d_1 = d_2 = a/2$. The frequency ω and the wave vector k are plotted in dimensionless units $\omega a/(2\pi c)$ and $ka/(2\pi)$, respectively. As can be seen, the photonic band structure repeats every reciprocal lattice vector $G = 2\pi/a$ due to periodicity of the structure. The discrete translational symmetry of the structure conserves the wave vector k modulo the addition of reciprocal lattice vectors, i.e., $k = k \pm mG$, where m is an integer. The region of non-redundant values of wave vector k, $-\pi/a < k \leq \pi/a$, is called the first Brillouin zone.

For comparison, the dispersion relation of a homogeneous dielectric material with a refractive index equal to the effective refractive index of the photonic crystal ($\omega = ck/n_{eff}$) is also shown in the figure with dashed lines. Here, n_{eff} is equal to the volume average of the dielectric constants of the constituent materials of the multilayer structure. For the periodic structure discussed here $n_{eff} = 2.6$. The dispersion relation of the homogeneous dielectric is repeated every reciprocal lattice vector G. As can be seen, the propagation of light in a photonic crystal is very different from the propagation of light in a homogeneous dielectric material. In a photonic crystal, light can be slowed down close to the edges of the first Brillouin zone ($k = \pm\pi/a$) or forbidden to propagate through the structure. By tuning the period (a), thicknesses of the layers (d_1 and d_2), and refractive indices of the layers (n_1 and n_2), it is possible to tune the dispersion of light in a photonic crystal.

Two-dimensional photonic crystals are periodic in two directions and can have a photonic band gap for light waves propagating in the plane of periodicity. Only three-dimensional photonic crystals, periodic in all three spatial directions, can have a complete photonic band gap, which prohibits light propagation in any direction in the structure. However, three-dimensional structures are difficult to make. Since they are compatible with planar semiconductor nanofabrication techniques, two-dimensional photonic crystal slabs are easier to make while offering some aspects of three-dimensional control of light propagation. These structures are usually semiconductor waveguide slabs perforated by a two-dimensional periodic arrays of holes. A photonic band gap may exist for the guided modes of the slab that are confined by total internal reflection. These structures have additional waveguide dispersion compared to infinitely long two-dimensional photonic crystals due to the vertical confinement of the modes.

1.1.2 Nanowires

Semiconductor nanowires are one-dimensional nanostructures that can be epitaxially grown using small, typically subwavelength, gold particles as a catalyst [13]. The actual nanowire grows under the gold particle and typical, as-grown wires, have a diameter of a few tens of nanometers and can be several micrometers long. The optical and electrical properties of the wires may be tuned by controlling their growth. Both regular and random arrays of nanowires as well as single nanowires can be grown for nanowire-based optoelectronic devices that include lasers [14–16], waveguides [17, 18], photodetectors [19–21], solar cells [22, 23], nonlinear optical converters [24, 25], biological and chemical sensors [26].

Nanowires made in a high refractive index semiconductor material (e.g., gallium phosphide) interact strongly with light. One of the examples of this strong light-matter interaction is the record high optical birefringence of $\Delta n = 0.8$ observed in random arrays of aligned gallium phosphide nanowires with a wire volume fraction of 40% [27]. The physical origin of this large birefringence is the anisotropic nature of the individual nanowires. This birefringence is common to all two-dimensional and one-dimensional photonic structures and is present in both periodic and non-periodic structures. This form birefringence, as introduced by van der Ziel in 1975 [28], is most easily explained for a multilayer structure consisting of alternating layers of two materials with different refractive indices (one-dimensional photonic crystal). For light propagating parallel to layers, the light-matter interaction depends strongly on the polarization state of the light and two cases can be distinguished: the electric field vector is either parallel or perpendicular to the layers. In both cases an effective dielectric constant can be defined that is analogous to either a set of resistors in series or a set of capacitors connected in series [28]. The effective dielectric constant is equal to the volume average of the dielectric constants of the constituent materials for the electric field parallel to the layers. The inverse of the effective dielectric constant is equal to the volume average of the inverse of the dielectric constants of the constituent materials for the electric field perpendicular to the layers. Similarly, for random arrays of nanowires the effective dielectric constant is strongly polarization dependent and is given by an appropriate average over the polarizability of each of the nanowires that form the array.

1.2 Frequency conversion

Frequency conversion refers to a process in which the incoming radiation generates radiation at a different frequency by interacting with a nonlinear medium [29]. This nonlinear process can be used to generate coherent radiation in the spectral regions where there are no convenient laser sources [30]. For instance, sum frequency generation can be used to produce tunable radiation at ultraviolet wavelengths by mixing the output of a fixed-frequency visible laser and the output of a frequency-tunable visible laser. The generated radiation can be used in biomedical applications because most organic materials absorb in the ultraviolet region. Difference frequency generation can be used to obtain tunable mid-infrared coherent radiation in the wavelength range of 3–12 μm. Since most molecules in the atmosphere have their strong absorption lines in this wavelength region, the mid-infrared radiation can be used for remote sensing of the atmosphere.

Besides practical applications, the process of frequency conversion is of great interest for fundamental science as well. A pump photon from an intense blue laser can spontaneously produce two photons at a red wavelength via a process called spontaneous parametric down-conversion. Since these twin photons are generated in pairs, strong correlations exist between the photons. Under appropriately chosen conditions this may lead to the generation of entangled photon pairs, which can be used to test the fundamental laws of quantum mechanics.

In this thesis we will constrain ourselves to the particular case of second harmonic generation (SHG), also known as frequency doubling. This is a relatively strong second-order nonlinear process that exists only in materials where the inversion symmetry is broken. These materials show a nonzero second-order nonlinear coefficient d.

In order to achieve efficient frequency conversion a phase-matching condition has to be satisfied [29]. Phase matching ensures that all the generated waves in the nonlinear medium are in phase and interfere constructively. For collinear second harmonic generation, the phase-matching condition is given by $\Delta k = 2k(\omega) - k(2\omega) = 0$, where $k(\omega)$ is the wave vector of the fundamental beam, and $k(2\omega)$ is the wave vector of the second harmonic beam. In optically isotropic materials, such as III-V semiconductors, the phase-matching condition can be reduced to $n(\omega) = n(2\omega)$, where $n(\omega)$ and $n(2\omega)$ are the refractive indices of the material at the fundamental and the second harmonic frequency respectively. In general, due to material dispersion, $n(\omega) < n(2\omega)$, and the phase-matching condition is not satisfied. Common ways to achieve a phase-matched interaction are via angle or temperature tuning of birefringent

materials such as beta-barium borate (BBO), potassium titanyl phosphate (KTP), or lithium niobate (LiNbO$_3$) [29]. However, this solution excludes optically isotropic materials with a much larger second-order nonlinearity. For example, the nonlinear coefficients d of gallium arsenide (GaAs) and gallium phosphide (GaP) are respectively about 70 and 30 times larger than the coefficient d of a BBO crystal [31, 32].

Bloembergen et al. [33] were the first to propose a periodic photonic structure with alternating layers of GaP and GaAs as a way to satisfy the phase-matching condition in III-V materials. By a proper choice of the parameters of the multilayer structure the dispersion of light can be tuned in such a way that the waves at the fundamental and the second harmonic frequency are phase-matched ($\Delta k = 2k(\omega) - k(2\omega) = 0$). Furthermore, an existing phase mismatch in a periodic structure can be compensated by adding an appropriate reciprocal lattice vector of the photonic lattice ($\Delta k = 2k(\omega) - k(2\omega) + mG = 0$). This latter mechanism is called quasi-phase-matching.

To summarize, we identify three different mechanisms by which a photonic structure can reduce a phase mismatch in a nonlinear optical process:

(i) Form birefringence, related to the anisotropy of the fundamental building blocks of the structure, can reduce a phase mismatch if different polarization states are used.

(ii) The strong light-matter interaction for materials with a large index contrast gives additional dispersion. This additional dispersion is due to a combination of Bragg diffraction leading to standing wave patterns and waveguide dispersion [34] that originates from the vertical confinement. Both contributions may be tuned via design of the structure.

(iii) In periodic structures discrete translational symmetry conserves the wave vector modulo the addition of a reciprocal lattice vector. This leads to quasi-phase-matching and allows to add a reciprocal lattice vector to the phase mismatch.

1.3 Thesis outline

This thesis describes an experimental investigation of second harmonic generation in III-V semiconductor photonic structures with wavelength and subwavelength feature sizes exploring possibilities (i)–(iii). The extra dispersion due to the special arrangement of dielectric material may be used to compensate a phase mismatch in a nonlinear process. To this end, we study two-dimensional

aluminum gallium arsenide ($Al_xGa_{1-x}As$) photonic crystal slabs in Chapters 3–6 and ensembles of aligned gallium phosphide (GaP) nanowires randomly grown in two dimensions in Chapter 2. All the chapters can be read independently of each other. A short description of each chapter is given below.

- **Chapter 2:** Ensembles of aligned gallium phosphide nanowires randomly grown on a gallium phosphide substrate show strong birefringence originating from the optical anisotropy of the wires. In this chapter we investigate if this birefringence can be used to reduce the phase mismatch in the nonlinear process of second harmonic generation. We describe a number of experiments that aim at separating the second harmonic light generated by the wires from the second harmonic light generated by the substrate. However, we were not successful in separating the nanowire contribution and showing the effect of the reduced phase mismatch for nanowires that are shorter than the coherence length.

- **Chapter 3:** This chapter describes the fabrication of freestanding, two-dimensional photonic crystal slabs made in $Al_{0.35}Ga_{0.65}As$. Light can resonantly couple to leaky modes of these structures, and the dispersion relations of these resonances can be extracted from the measured linear reflection spectra. The nonlinear reflection spectra show that resonant coupling of a pulsed laser at a wavelength of 1.535 μm can significantly enhance the second harmonic signal. By tuning the angle of incidence the pulsed laser beam is tuned into resonance with one of the leaky modes of the structure, and a second harmonic enhancement of more than 4500 $\times$ the non-resonant contribution is measured.

- **Chapter 4:** A novel method to transfer freestanding photonic crystal slabs to a transparent gel substrate is presented in this chapter. Compared to the freestanding structures of Chapter 3, transferred structures allow for both reflection and transmission measurements. The resonant features in measured reflection spectra of a structure on the gel are much more prominent than those in reflection spectra of a freestanding structure. We show that the measured quality factor of one of the leaky modes, $Q = 300$, is limited by the finite size of the $\sim 300 \times 300 \ \mu m^2$ photonic crystal slab.

- **Chapter 5:** Resonant coupling of light to leaky modes of a photonic crystal slab leads to asymmetric Fano lineshapes in the reflection and transmission spectra. These lineshapes can be explained in terms of

the Fano model. Within this model, the interference between the non-resonant and the resonant contribution leads to the asymmetric line-shape in the spectra. For lossless and symmetric structures, the sign of the real-valued parameter q of the Fano model, which can be interpreted as the ratio between the resonant and the non-resonant contribution, controls the asymmetry of the resonance. For a symmetric air-slab-air structure parameter q changes its sign if the amplitude reflection coefficient of the slab goes through zero. We show that for an asymmetric air-slab-gel structure it is also possible to change the asymmetry of a resonance by angle tuning without reaching the condition of zero amplitude. This behavior requires a complex-valued q parameter and demonstrates that a complex q is not necessarily a sign of the microscopic processes of decoherence and/or dephasing.

- **Chapter 6:** In this chapter we investigate second harmonic generation from photonic crystal slabs transferred to a transparent gel substrate. The second harmonic is measured in transmission as a function of the angle of incidence of the fundamental beam. Compared to Chapter 3 we go a step further in understanding the influence of the resonant coupling of both the fundamental and the second harmonic field to the second harmonic generation. A relatively simple coupled mode theory rather than full numerical calculations is used to explain the measured second harmonic. This model does not assume parameters of an ideal two-dimensional photonic crystal slab. Instead, it uses experimental dispersion relations and quality factors of relevant modes as well as the experimental non-resonant second harmonic signal, obtained by measuring the linear and nonlinear optical properties of our structure. At normal incidence, both the fundamental and the second harmonic wave are resonant with leaky modes of the structure, and we measure an enhancement of more than $10000 \times$ compared to the non-resonant contribution. The measurements convincingly show the effect of resonant coupling to a leaky mode at the second harmonic frequency. The angular width of the measured second harmonic signal is significantly smaller than the width predicted from the linear optical properties of the leaky mode at the fundamental frequency. Furthermore, two additional satellite peaks appear at angles of incidence of $\pm 9.1°$. Using the coupled mode theory we show that also the resonant coupling to a leaky mode at the second harmonic frequency has to be taken into account in order to explain the reduced width of the measured second harmonic signal at normal incidence and the two satellite peaks. This shows the importance of a double resonant

condition for efficient second harmonic generation from photonic crystal slabs.

CHAPTER 2

Second harmonic generation in gallium phosphide nanowires

2.1 Introduction

Semiconductor nanowires are essentially one-dimensional (1D) nanostructures that have subwavelength lateral dimensions and typical lengths of several micrometers. Since the introduction of nanowires by Yazawa et al. [35], many advances have been made in tuning their electrical and optical properties by controlling their growth. Today, nanowires represent a class of metamaterials that shows promise for many device applications compatible with on-chip technologies. The list of nanowire-based optoelectronic devices includes lasers [14–16], waveguides [17, 18], photodetectors [19–21], solar cells [22, 23], nonlinear optical converters [24, 25], biological and chemical sensors [26].

The high length-to-width aspect ratios of the nanowires combined with the high refractive index of semiconductors can lead to strong polarization anisotropy that facilitates some of their applications. Wang et al. [19] were the first to experimentally demonstrate the optical anisotropy of a single indium phosphide (InP) nanowire by measuring its photoluminescence (PL) properties. The authors point out the possibility of using InP nanowires as polarization sensitive photodetectors incorporated into photonic-based circuits.

Recent advances in the bottom-up fabrication method of metal-organic vapor phase epitaxy (MOVPE) [13], made it possible to grow a high density of aligned gallium phosphide (GaP) nanowires. These nanowire metamaterials, made out of an optically isotropic material, exhibit extremely large birefringence solely due to the anisotropy of the nanowire building blocks [27, 36]. The resulting birefringence is determined by the volume fraction, length and the orientation of the nanowires. Inducing form birefringence by nanostruc-

turing bulk materials represents an important approach in making III-V materials, like gallium arsenide (GaAs) and GaP, more attractive for nonlinear optics [28, 37].

A large *optical nonlinearity* as well as perfect *phase-matching conditions* are necessary in order to achieve large nonlinear yields [29]. Phase matching ensures that all the waves generated inside the nonlinear medium interfere constructively. In most materials, this phase-matching condition is not met due to material dispersion. Therefore, birefringent materials are commonly used to compensate material dispersion and phase-match the nonlinear interaction. Although bulk GaP has about 30 times larger effective second-order nonlinear susceptibility, $\chi_{eff}^{(2)}$, than that of a BBO crystal, it doesn't possess birefringence. The second harmonic (SH) signal, generated in bulk GaP, is much smaller than that of bulk BBO. The large geometrical anisotropy of aligned GaP nanowires, combined with a high refractive index contrast between the GaP and the surrounding air, gives rise to strong form birefringence and has been extensively studied by Muskens et al. [27, 36]. However, little is known about using the birefringence of these photonic metamaterials to achieve phase matching in nonlinear optical processes.

In this chapter we study second harmonic generation (SHG) in samples containing ensembles of aligned GaP nanowires randomly grown on a GaP substrate. We investigate the influence of the birefringence of the nanowire layer on second harmonic generation. We consider the symmetry of the second-order nonlinear tensor $\chi^{(2)}$ of the nanowire metamaterials as well. The symmetry of the nonlinear tensor $\chi^{(2)}$ of the nanowires maybe differs from that of bulk GaP due to the numerous stacking faults in the nanowires [13].

2.2   Sample description

Figures 2.1(a), (b) and (c) show cross-sectional SEM images of aligned GaP nanowires, randomly grown on a (111)B (phosphorous terminated) GaP facet. The nanowires were grown in the facilities of Philips Research. The nanowires grow preferentially along the <111>B directions and are therefore perpendicular to the surface of the substrate. The existence of a preferential growth direction can be exploited to make samples with a non-vertical orientation of the nanowires by choosing a substrate with different crystallographic orientation. For example, a (100) oriented GaP substrate can be used to grow nanowires, as shown schematically in Figure 2.2. A brief summary of the fabrication process and birefringent properties of these structures is given in this section. Additional details can be found in References [13, 27, 36].
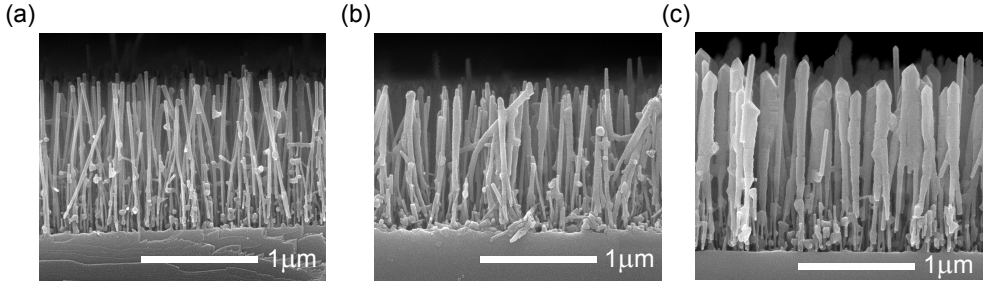
(a)   (b)   (c)

1μm   1μm   1μm

Figure 2.1. Cross-sectional SEM images of aligned GaP nanowires epitaxially grown on a (111)B GaP substrate, with a length of ≈ 1.3 μm and lateral shell growth times of 100 sec. (a), 350 sec. (b) and 1100 sec. (c) [38].
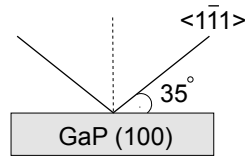

$<1\bar{1}1>$

$35°$

GaP (100)

Figure 2.2. A schematic presentation of the nanowire growth on a (100) GaP substrate. Nanowires grow preferentially along the <111>B directions.

GaP nanowires are epitaxially grown using a bottom-up process of metal-organic vapor phase epitaxy (MOVPE) [13]. After depositing a 0.3 nm thick gold film on the substrate, the wafer is inserted into a MOVPE chamber and heated to a temperature of 420°C. At this temperature, the gold film breaks into ~ 20 nm droplets that serve as a catalyst. Immediately after that, the precursors, tri-methyl-gallium (GaC_3H_9) and phosphine (PH_3), are introduced into the chamber and the nanowires start growing underneath the gold droplets. The length of the wires is determined by the growth time and the initial wire diameter is determined by the size of the gold droplets. The thickness of the wires can be increased by a lateral growth mechanism at an elevated temperature of 630°C. Figures 2.1(a), (b) and (c) show different wires obtained by lateral growth times of 100, 350 and 1100 seconds, resulting in volume filling fractions of nanowires f of 0.07, 0.15 and 0.4, respectively [38].

Figure 2.3 shows the experimentally determined birefringence at a wavelength of 632.8 nm (points) as a function of the nanowire volume fraction for GaP nanowires grown on a (111)B GaP substrate [27]. The birefringence in-
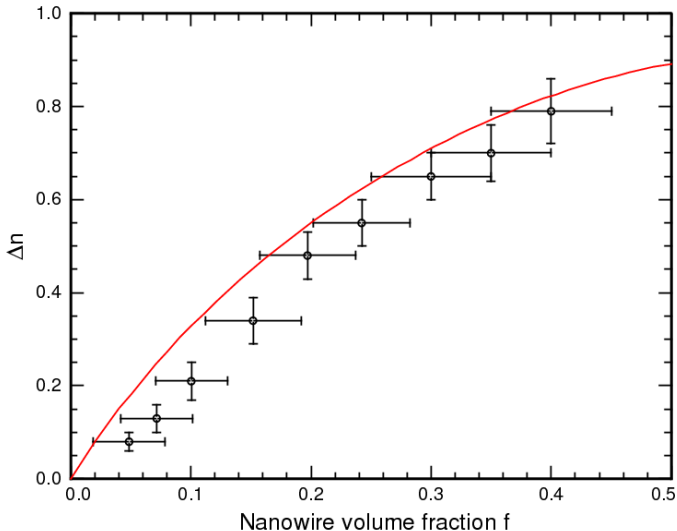
Figure 2.3. Birefringence (Δn) at a wavelength of 632.8 nm, as a function of the nanowire volume fraction (f), for GaP nanowires grown on a (111)B oriented GaP substrate. The theoretical curve (red line), calculated using Maxwell-Garnet effective medium theory, is plotted on top of the experimental data (points) taken from Ref. [27].

creases strongly with volume fraction reaching values as large as 0.79 ± 0.07 for a volume fraction of 0.4 ± 0.05.

The layer of subwavelength GaP nanowires grown on a (111)B gallium phosphide substrate can be treated as a *positive uniaxial* crystal. The birefringence $\Delta n = n_e - n_o$, with the ordinary (n_o) and the extraordinary (n_e) index of refraction, is positive, reflecting the stronger interaction with light when the **E**-field vector is parallel to the long axis of the wires. We approximate the nanowires by infinitely long cylindrical pillars, and assume that the nanowire volume fraction f is low, and use Maxwell-Garnett effective medium theory [39,40] to calculate the refractive indices n_o and n_e using the following expressions:

$$n_o^2 = \left(1 + \frac{2f\alpha}{1 - f\alpha}\right), \tag{2.1}$$

$$n_e^2 = fn^2 + (1 - f), \tag{2.2}$$

where $\alpha = (n^2 - 1)/(n^2 + 1)$ is the polarizability of cylindrical pillars, and n is the index of refraction of bulk GaP. The calculated birefringence is indicated by the red line in Fig. 2.3, and agrees very well with the experimental data.

The nanowires that we studied all have a similar length of ≈ 1.3 μm, but different samples have different volume fractions f. The wires are grown on ~ 500 μm thick (111)B oriented substrates. The relevant parameters of samples B9138 (Fig. 2.1(b)) and B9165 (Fig. 2.1(c)) are summarized in Table 2.1.

Table 2.1. Parameters of the nanowire metamaterials used in our experiments.

Sample label	GaP substrate orientation	Length (μm)	Volume fraction f (%)	Birefringence Δn
B9138	(111)B	1.26	15	0.34
B9165	(111)B	≈ 1.3	40	0.79

2.3 Setup

2.3.1 Description of the setup

Figure 2.4(a) shows a schematic of the setup used to study second harmonic generation in transmission from ensembles of aligned GaP nanowires. A Q-switched diode-pumped solid state laser (Cobolt Tango) is employed as the source of radiation at the fundamental wavelength. The laser uses an Er:Yb-doped glass as the gain medium to produce a laser beam operating in the TEM$_{00}$ mode (M^2<1.2). The fundamental beam has a specified center wavelength of 1535 ± 1 nm and a narrow linewidth (< 0.04 nm). Short pulses, with a duration of ≈ 3.8 ns (full width at half maximum) and a ~ 1.3 kW peak power, are generated at a repetition rate of 5 kHz.

The divergent laser beam is collimated by lens L1 with a focal length of 60 mm and sent through an optical isolator (OFR IO-4-1535-HP-Z) to eliminate instability of the laser power output due to the optical feedback. During the measurements, we check for laser power fluctuations by monitoring the output of the internal laser photodiode using a Lab View program.

The combination of a half-wave ($\lambda/2$) plate and a Glan-Thompson polarizing beamsplitter cube (POLARIZER) is used to define the polarization and can be used to attenuate the power of the incident fundamental beam if desired. The fundamental beam is focused onto the sample by lens L2 with a focal length of 175 mm, and the generated second harmonic is collected and collimated in transmission by lens L3 (focal length of 175 mm). We can set the angle of incidence θ, the azimuthal angle φ, and the position of the sample
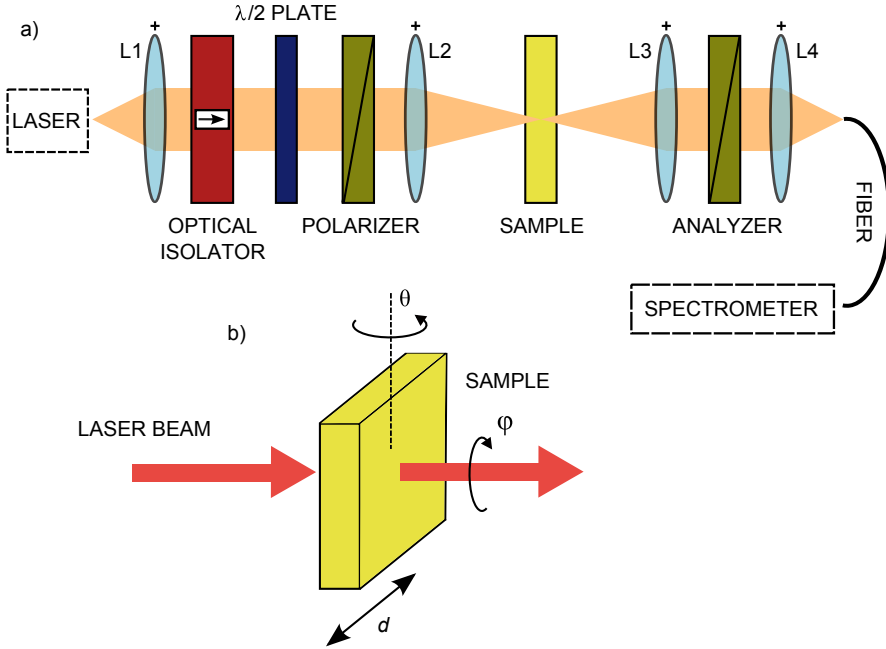
Figure 2.4. (a) Setup used for investigating the second harmonic generation in transmission from nanowire metamaterials. The fundamental beam is focused on the sample and the generated second harmonic is collected in transmission and forwarded to a fiber-coupled spectrometer. Lenses L1–L4 serve to focus and collimate the light. The polarization of the incident fundamental is defined using a combination of a $\lambda/2$ plate and a polarizer. The polarization state of the second harmonic is studied with a second polarizer (analyzer). An optical isolator is employed to prevent optical feedback caused by the light reflecting back into the laser cavity. (b) Details of the sample stage. The angle of incidence θ, the azimuthal angle φ, and the position of the sample d, can be set individually using motorized stages.

d, individually, using motorized stages, as sketched in Figure 2.4(b). A second Glan-Thompson polarizing beamsplitter cube (ANALYZER) is used to study the polarization properties of the SH light. In the end, the second harmonic is focused by lens L4 (focal length of 15.3 mm) onto a 600 μm multimode fiber and sent to a fiber-coupled grating spectrometer USB4000 (resolution $\approx$ 1.3 nm).

2.3.2 Second harmonic generation from BBO

In order to test the setup and our 1535 nm laser we generated second harmonic using a 1 mm BBO crystal. Figure 2.5 shows the measured second harmonic signal as a function of angle of incidence (black dots). The phase matching in this standard crystal is well-known. For a collinear second harmonic generation the power at the SH frequency $P(2\nu)$ is proportional to the square of the power at the fundamental frequency $P(\nu)$, and can be expressed as [29]:

$$P(2\nu) \propto L^2 \text{sinc}^2\left(\Delta k L/2\right) P(\nu)^2, \tag{2.3}$$

where

$$\text{sinc}^2\left(\Delta k L/2\right) = \frac{\sin^2\left(\Delta k L/2\right)}{\left(\Delta k L/2\right)^2}, \tag{2.4}$$

and

$$\Delta k = 2k(\nu) - k(2\nu) = \frac{4\pi\nu}{c}\left(n(\nu) - n(2\nu)\right). \tag{2.5}$$
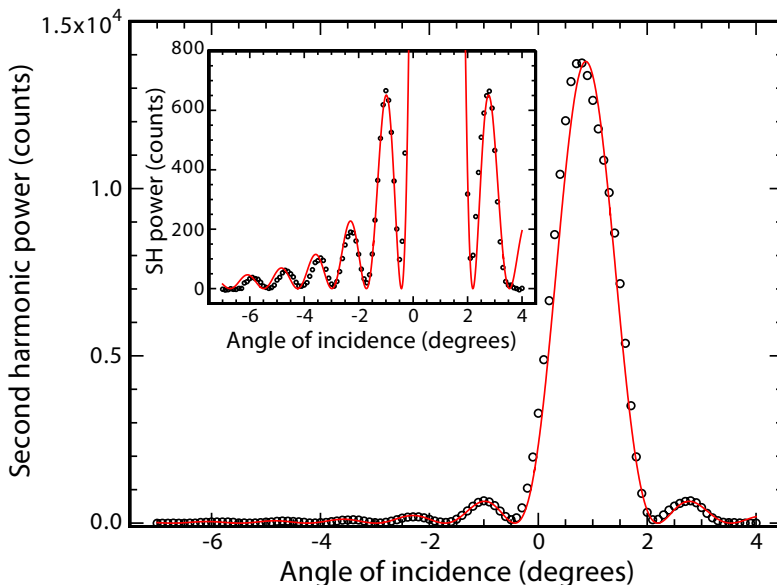
Figure 2.5. Second harmonic power as a function of angle of incidence (black dots), generated in a 1 mm BBO crystal, and measured in transmission. The red line is a fit obtained by considering the phase-matching condition in a negative uniaxial crystal (see text). The SH signal reaches maximum when the phase-matching condition is satisfied. The inset zooms in on lower values of SH power emphasizing the good agreement of higher order maxima.

Here $k(\nu)$ and $k(2\nu)$ are the wave vectors at the fundamental and the second harmonic frequency, respectively. Thickness of the crystal is denoted by L. When the refractive index at the fundamental frequency $(n(\nu))$ is equal to the refractive index at the SH frequency $(n(2\nu))$, $\Delta k = 0$ and the phase-matching condition is satisfied resulting in maximum SH yield. For a BBO crystal, phase matching can be achieved by choosing the polarization of the SH wave to be extraordinary so that it experiences the lower of the two refractive indices. We employ type II phase matching where one of the waves at the fundamental frequency is an extraordinary wave while the other wave is an ordinary wave. The phase-matching condition $\Delta k = 0$ can then be expressed as:

$$n_o(\nu) + n_e(\nu, \psi) - 2n_e(2\nu, \psi) = 0, \tag{2.6}$$

where ψ is the angle between the wave vector $\mathbf{k}$ and the optic axis of the BBO crystal. The refractive index $n_e(\nu, \psi)$ is given by

$$\frac{1}{n_e(\nu, \psi)^2} = \frac{\sin^2 \psi}{n_e(\nu, 90°)^2} + \frac{\cos^2 \psi}{n_o(\nu)^2}. \tag{2.7}$$

In the experiment, the fundamental beam is polarized under an angle of $45°$ with respect to the plane containing the wave vector $\mathbf{k}$ of the incident light and the optic axis. The crystal is cut so that the type II phase-matching condition is satisfied close to normal incidence. The fundamental beam is focused to a spot of ≈ 120 μm with a numerical aperture (NA) ≈ 0.01, and the angle of incidence θ is varied from -7° to 4° in steps of 0.1°. By varying the angle of incidence θ we vary the angle ψ between the wave vector $\mathbf{k}$ and the optic axis.

To fit the experimental data, we use Equation 2.3 with $A = L^2 P(\nu)^2$ as a fitting parameter. The phase mismatch Δk is given by the known refractive indices of BBO:

$$\Delta k = \frac{2\pi\nu}{c} \left(n_o(\nu) + n_e(\nu, \psi) - 2n_e(2\nu, \psi) \right). \tag{2.8}$$

Here ψ is the angle between the wave vector $\mathbf{k}$ and the optic axis inside the material. We use an additional fitting parameter which describes the angle between the optic axis and the surface normal. As can be seen from Figure 2.5, the obtained fit (red solid line), agrees well with the experimental data. The inset shows that even the secondary maxima of the sinc^2 function are nicely reproduced.

2.4   SHG in samples with GaP nanowires

Figure 2.6 shows the measured power of the signal at a frequency of 390.9 THz (wavelength of 767.5 nm) as a function of the power of the incident fundamental beam (black dots), generated in transmission from sample B9165. The inset shows a typical spectrum of the signal detected by a fiber-coupled spectrometer USB4000. We focus the fundamental beam to a spot of ≈ 120 μm with a numerical aperture ≈ 0.01, and keep the angle of incidence as well as the polarization of the incident fundamental constant throughout the measurement. The power at the second harmonic frequency grows with the square of the fundamental power, as indicated in Fig. 2.6 with a linear fit (red line) of a slope of 1.975$\pm$0.008.

The crucial question is whether this second harmonic signal is generated in the nanowire layer or in the underlying substrate. One possibility is to use the birefringence of the nanowires to achieve phase matching via angle tuning of
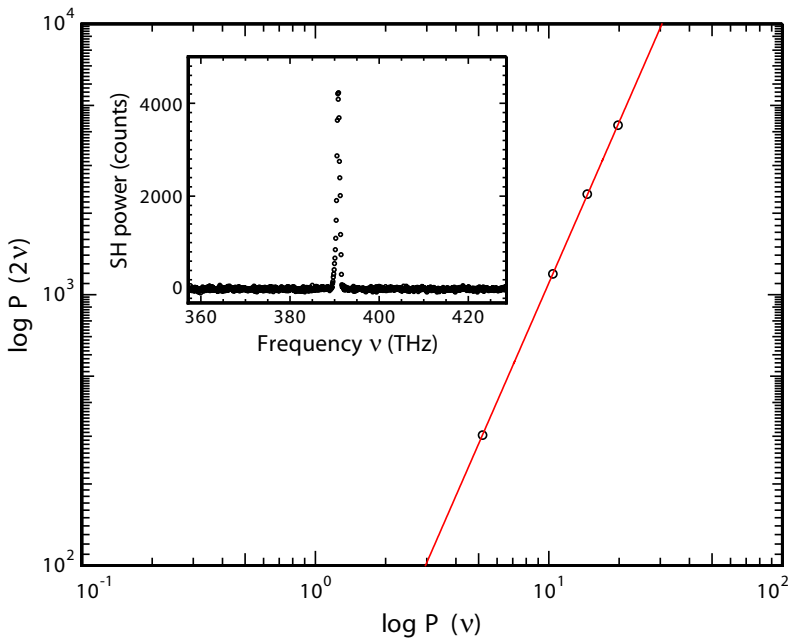

Figure 2.6. Measured power of the signal at a frequency of 390.9 THz (wavelength of 767.5 nm) as a function of the fundamental power (black dots), generated in transmission from sample B9165. The red line represents a linear fit confirming the quadratic power dependence. A typical spectrum of the SH signal is shown in the inset.

the sample. When successful, a much more efficient SHG would be obtained from the nanowire layer than from the substrate. Unfortunately, it is not possible to demonstrate this with short nanowires with a length of ≈ 1.3 μm, which is smaller than the coherence length L_c. This coherence length is defined as $L_c = 2/\Delta k$ [29], where Δk is given by Equation 2.5, and defines a length over which the fundamental and second harmonic waves are in phase. For a bulk GaP crystal used for frequency doubling of 1535 nm light, the coherence length L_c is about 3 μm. The large value of Δk for bulk GaP is due to the strong dispersion of the material. For a nanowire layer that contains mostly air, the effective refractive index and consequently also the dispersion are lower than that of the bulk. Therefore, we expect a smaller Δk and thus a longer coherence length. Phase matching which reduces Δk and increases L_c is only effective if the crystal thickness L is much larger than L_c ($L >> L_c$). To enhance the second harmonic signal due to the nanowires by phase matching, we could make the nanowires much longer than the coherence length. However, long nanowires (> 10 μm) have a significantly reduced birefringence due to the bending of the wires [27]. Therefore, a sample with these long nanowires is not a good candidate for efficient second harmonic generation.

In the remainder of the chapter we will discuss two possibilities to find out whether the measured second harmonic signal in Figure 2.6 is generated in the nanowire layer or in the underlying substrate. In Section 2.4.1 we discuss a possible difference in tensor properties of $\boldsymbol{\chi}^{(2)}$ between the bulk material and the nanowires. In Section 2.4.2 we discuss an experiment where we use the strong absorption of blue light in GaP to get rid of the substrate contribution.

2.4.1   Tensor properties of nanowires

Figures 2.7(a) and (b) show polar plots of the measured SH signal in transmission as a function of the azimuthal angle φ for sample B9165 and a (111) oriented GaP reference substrate, respectively. The experimental data are offset by 500 counts for clarity. The fundamental beam is at normal incidence, and is focused to a spot of ≈ 120 μm with a numerical aperture ≈ 0.01. The azimuthal angle φ (Fig. 2.4(b)) is varied from 0° to 360° in steps of 3°. The black dots and red triangles in Figure 2.7 correspond to the experimental data points for the parallel and the orthogonal orientation of the polarizer and the analyzer. In this way we probe some of the symmetry properties of the nonlinear susceptibility tensor $\boldsymbol{\chi}^{(2)}$.

Bulk gallium phosphide crystalizes in zincblende structure, which has point group $\bar{4}3m$ symmetry. The crystal structure of the nanowires is also predominantly zincblende, as determined by high resolution transmission electron
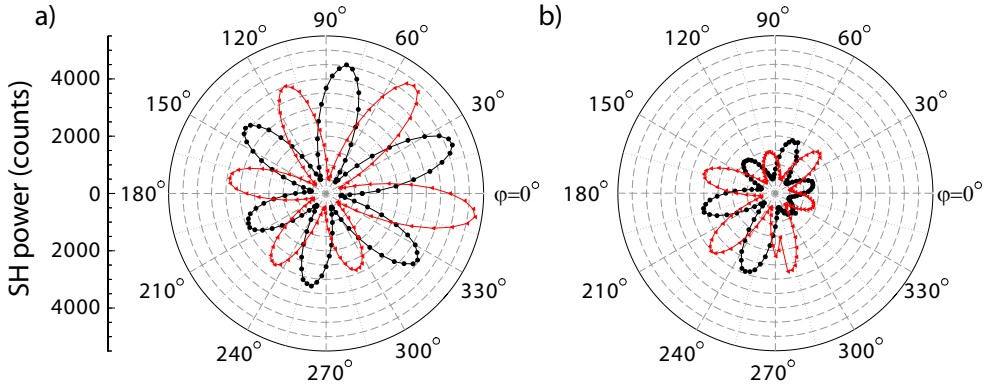
Figure 2.7. Measured SH power as a function of the azimuthal angle φ for (a) sample B9165 and (b) a (111) oriented GaP reference substrate, offset by 500 counts for clarity. The SH signal is measured in transmission at normal incidence. Black dots (red triangles) correspond to experimental data points for the parallel (orthogonal) orientation of the polarizer and the analyzer (Fig. 2.4(a)). Solid lines serve only as a guide to the eye. As expected, the power at the SH frequency is proportional to $\sin^2(3\varphi)$ ($\cos^2(3\varphi)$).

microscopy (HRTEM) [36]. At the same time, the crystal structure of the nanowires contains many stacking faults [13]. To understand the nature of these defects let us consider the stacking sequence of atomic layers in a cubic zincblende structure [12]. In a perfect zincblende structure the atomic layers are stacked in an ...ABCABC... (fcc) sequence along the [111] direction. A stacking fault of the hexagonal layers locally changes the stacking sequence to ...ABAB... (hcp), and as a result a hexagonal wurtzite crystal structure is formed. For GaP nanowires that grow along a [111] direction of the cubic lattice, the wurtzite domains are oriented along a [0001] direction of the hexagonal lattice [12]. The wurtzite structure belongs to a $6mm$ point group symmetry, and has a different second-order nonlinear susceptibility tensor compared to a zincblende structure. To appreciate the difference we use a contracted notation for the nonlinear susceptibility tensor. Instead of the rank 3 tensor $\boldsymbol{\chi}^{(2)}$ we use a 6×3 rank 2 tensor $\boldsymbol{d}$ with elements d_{ij} [29]. For zincblende (group $\bar{4}3m$) the elements d_{14}, d_{25}, and d_{36} are all equal and nonzero. For wurtzite (group $6mm$) the nonzero elements are $d_{15} = d_{24}$, $d_{31} = d_{32}$, and d_{33}.

Let's calculate the SH power as a function of the azimuthal angle φ, generated in transmission from a (111) oriented GaP slab, at normal incidence of

21

the fundamental beam. Instead investigating a system in which the sample is rotated, we study an equivalent problem where both the incident polarization of the fundamental and the analyzer are rotated by the same angle φ while the sample is fixed.

The nonlinear polarization $\mathbf{P}^{NL}(2\nu)$ generated by the electric field $\mathbf{E}(\nu)$ in the medium is given by [29]

$$\mathbf{P}^{NL}(2\nu) = 4d_{14} \begin{pmatrix} E_y(\nu)E_z(\nu) \\ E_x(\nu)E_z(\nu) \\ E_x(\nu)E_y(\nu) \end{pmatrix}, \tag{2.9}$$

where $E_x(\nu)$, $E_y(\nu)$, and $E_z(\nu)$ are the electric field components along the x, y, and z-axis of the Cartesian coordinate system, respectively. Here, we define x, y, and z-axis to coincide with the crystallographic axes [100], [010], and [001].

We chose unit vectors $\frac{1}{\sqrt{2}}(1,-1,0)$, $\frac{1}{\sqrt{6}}(1,1,-2)$, and $\frac{1}{\sqrt{3}}(1,1,1)$, denoted by $\mathbf{e}_1$, $\mathbf{e}_2$, and $\mathbf{e}_3$, respectively, to form an orthonormal basis of $\mathbf{R}^3$. At normal incidence, the wave vector $\mathbf{k}$ of the incident fundamental is parallel to $\mathbf{e}_3$ with the $\mathbf{E}$-field in the plane spanned by $\mathbf{e}_1$ and $\mathbf{e}_2$. Consequently, the incident electric field $\mathbf{E}(\mathbf{r}, t)$ as a function of the azimuthal angle φ is given by

$$\mathbf{E}(\mathbf{r}, t) = \mathbf{E}(\nu, \varphi)e^{-i2\pi\nu t} + \mathbf{E}(-\nu, \varphi)e^{+i2\pi\nu t}, \tag{2.10}$$

where

$$\begin{aligned} \mathbf{E}(\nu, \varphi) &= \frac{1}{2}E_0 e^{i\mathbf{kr}}\left(\cos(\varphi)\mathbf{e}_1 + \sin(\varphi)\mathbf{e}_2\right) \\ &= \frac{1}{2}E_0 e^{i\mathbf{kr}} \begin{pmatrix} \frac{\cos(\varphi)}{\sqrt{2}} + \frac{\sin(\varphi)}{\sqrt{6}} \\ \frac{\sin(\varphi)}{\sqrt{6}} - \frac{\cos(\varphi)}{\sqrt{2}} \\ -\sqrt{\frac{2}{3}}\sin(\varphi) \end{pmatrix}. \end{aligned} \tag{2.11}$$

Here, $\mathbf{E}(-\nu, \varphi)$ is the complex conjugate of $\mathbf{E}(\nu, \varphi)$, and E_0 is the amplitude of the electric field. Combining Equations 2.9 and 2.11, we arrive to the following expression for the Cartesian components of the nonlinear polarization $\mathbf{P}^{NL}(2\nu)$ as a function of the azimuthal angle φ:

$$\begin{aligned} P_x^{NL}(2\nu, \varphi) &= \tfrac{2}{3}E_0^2 d_{14}\sin(\varphi)\left(\sqrt{3}\cos(\varphi) - \sin(\varphi)\right), \\ P_y^{NL}(2\nu, \varphi) &= -\tfrac{2}{3}E_0^2 d_{14}\sin(\varphi)\left(\sqrt{3}\cos(\varphi) + \sin(\varphi)\right), \\ P_z^{NL}(2\nu, \varphi) &= -\tfrac{1}{3}E_0^2 d_{14}\left(1 + 2\cos(2\varphi)\right). \end{aligned} \tag{2.12}$$

The measurement scheme with the parallel (orthogonal) orientation of the polarization of the incident fundamental and the analyzer, filters through the nonlinear polarization $P_{\parallel}^{NL}(2\nu, \varphi)$ $(P_{\perp}^{NL}(2\nu, \varphi))$, given by

$$
\begin{aligned}
P_{\parallel}^{NL}(2\nu, \varphi) &= \mathbf{P}^{NL}(2\nu)\left(\cos(\varphi)\mathbf{e}_1 + \sin(\varphi)\mathbf{e}_2\right) \\
&= -\sqrt{\frac{2}{3}}E_0^2 d_{14}\cos(3\varphi), \tag{2.13}
\end{aligned}
$$

$$
\begin{aligned}
P_{\perp}^{NL}(2\nu, \varphi) &= \mathbf{P}^{NL}(2\nu)\left(\sin(\varphi)\mathbf{e}_1 - \cos(\varphi)\mathbf{e}_2\right) \\
&= \sqrt{\frac{2}{3}}E_0^2 d_{14}\sin(3\varphi). \tag{2.14}
\end{aligned}
$$

The corresponding expressions for the SH power as a function of the azimuthal angle φ, $P_{\parallel}(2\nu, \varphi)$ and $P_{\perp}(2\nu, \varphi)$, are proportional to the square of the nonlinear polarizations $P_{\parallel}^{NL}(2\nu, \varphi)$ and $P_{\perp}^{NL}(2\nu, \varphi)$, respectively:

$$
P_{\parallel}(2\nu, \varphi) \propto \cos^2(3\varphi), \tag{2.15}
$$

$$
P_{\perp}(2\nu, \varphi) \propto \sin^2(3\varphi). \tag{2.16}
$$

As can be seen from Fig. 2.7, the experimentally obtained SH signal qualitatively exhibits the $\sin^2(3\varphi)$ $(\cos^2(3\varphi))$ dependence, for both the reference (111) GaP substrate and sample B9165. We observe six lobes in the polar plots and the fact that all the minima really go to zero, once the offset of 500 counts is subtracted. However, the amplitudes of the lobes vary, probably due to a non-perfect alignment. Namely, the wave vector $\mathbf{k}$ of the incident fundamental does not exactly coincide with the rotation axis of the sample. As a result, the fundamental beam describes a circle on the sample during the measurement. Most probably, the SH signal fluctuates from spot to spot on the sample due to the variation in the sample thickness. These fluctuations of the second harmonic signal are essentially *Maker fringes* [41].

With currently available samples, one might be tempted to employ an experimental scheme where the wave vector $\mathbf{k}$ of the fundamental beam is perpendicular to a (100) substrate from which the nanowires grow preferentially in the <111>B directions (Fig. 2.2). If a Cartesian coordinate system with a z-axis parallel to the vector $\mathbf{k}$ is adopted, the only component of the nonlinear polarization that can be generated in the substrate is $P_z^{NL}(2\nu)$, and this cannot give rise to a SH signal in transmission. Let's consider now a single pair of nanowires that form a *V*-shaped structure in the <111>B directions (Fig. 2.2) on top of the substrate. In principle, the symmetry of the $\boldsymbol{\chi}^{(2)}$ tensor is such that a SH signal can be generated in transmission from the

wurtzite domains in a single nanowire. However, due to a geometric symmetry of the V shape, the components of the nonlinear polarization perpendicular to the wave vector **k** of the fundamental, generated in the two nanowires, cancel each other. Thus, there is no SH signal generated in transmission from the nanowires either.

2.4.2 Second harmonic generation at 425 nm

Figure 2.8 shows the SH signal at a wavelength of 425 nm as a function of the position of the fundamental beam on the sample (black dots), measured in transmission for sample B9138 with a 15% volume fraction of nanowires. The fundamental beam at a wavelength of 850 nm enters the sample at normal incidence from the substrate side (see inset) generating second harmonic as it propagates. Since the absorption length at a wavelength of 425 nm is only $\sim$ 200 nm for bulk GaP, we can assume that the SH signal in transmission is due to a thin layer ($< 1~\mu$m) of the side of the sample facing the detector.
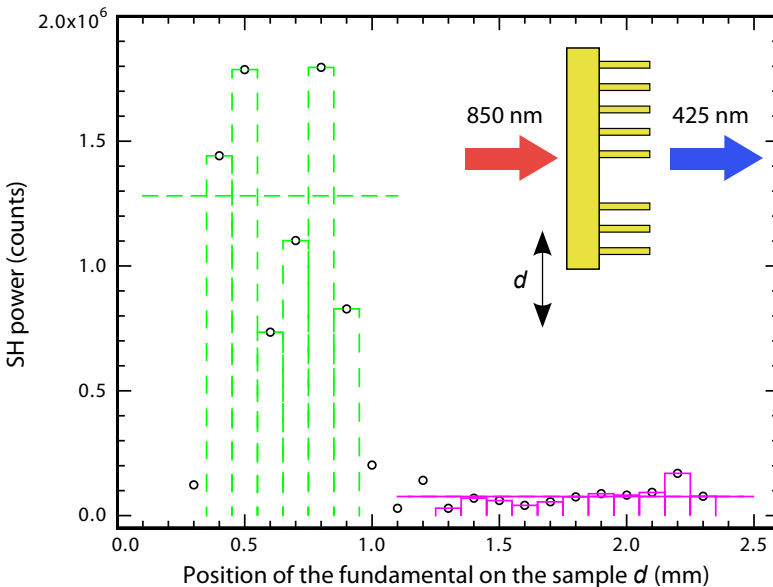

Figure 2.8. Measured SH signal in transmission as a function of the position of the fundamental beam on sample B9138. A scheme of the experimental geometry is presented in the inset. The dashed (solid) bars indicate the signal generated from a region without (with) the nanowires. The horizontal dashed (solid) line indicates the average SH signal.

Therefore, for the fundamental beam exiting the sample through the nanowire layer, the SH signal should have a large component due to the nanowires. By translating the sample relative to the fundamental beam we probe regions with and without the nanowires, without changing the angle of incidence on the sample.

In the experiment, the setup from Fig. 2.4(a) is slightly modified. A Ti:Sapphire laser is used to generate pulses at 850 nm with a duration of ~ 2 ps full width at half maximum at a repetition rate of 80 MHz. The fundamental is focused to a spot of ~ 30 μm by a lens with a focal length of 100 mm. Since the nanowire layer acts as a highly scattering medium for radiation at 425 nm [36], a lens with a high NA of 0.5 and a focal length of 8 mm is used to collect the SH signal in transmission. The collimated second harmonic is focused onto a Peltier cooled CCD. A combination of the Newport bandpass filter FSR-BG39, with a transmission region of $\approx$ 350–600 nm, and the Thorlabs shortpass filter FES0550, with a cut-on wavelength of about 550 nm, is inserted before the CCD to filter out the fundamental beam, and ensure the detection of the second harmonic signal only.

The dashed and solid bars in Figure 2.8 correspond to the SH signal originating from the region without and with nanowires, respectively. The average second harmonic signal generated in the region without nanowires (horizontal dashed line) is ≈ 17 times larger than the average second harmonic signal generated in the region with nanowires (horizontal solid line). Apparently, nanowires on the sample do not lead to enhanced second harmonic generation in the forward direction. We speculate that the main contribution of the nanowires is to scatter the second harmonic generated in bulk GaP to angles inside the high refractive index substrate. This scattered second harmonic signal is not collected by our setup. Unfortunately, the current experimental data do not distinguish between scattered light and light generated by the nanowires, preventing a more detailed quantitative analysis.

2.5   Conclusion

The coherence length for second harmonic generation in bulk GaP at a wavelength of 1535 nm is more than two times larger then the wire length of short GaP nanowires with a length of ≈ 1.3 μm. As a result, the contribution to the SH signal originating from the substrate is likely to be larger than the contribution originating from the nanowire layer.

In order to separate and identify the second harmonic due to the nanowires, we tried to eliminate the substrate contribution to the SH signal by exploring

the symmetry of the nonlinear tensor $\boldsymbol{\chi}^{(2)}$, and by an experiment at a second harmonic wavelength of 425 nm at which GaP is highly absorbing. Stacking faults in the nanowires lead to a locally different crystal structure (wurtzite) compared to bulk GaP (zincblende). With currently available samples, we were unable to define an appropriate experimental geometry to exploit this symmetry and generate signal from nanowires only. For second harmonic generation at an absorbing wavelength, the obtained experimental data can be explained by SH generated in the substrate and scattered by the nanowires.

Replacing the GaP substrate with another substrate that has a very low, if not zero, second-order nonlinear susceptibility, while maintaining the original orientation of the nanowires, is probably the best way to study the second harmonic generation in ensembles of aligned nanowires [42].

CHAPTER 3

Second harmonic generation in freestanding AlGaAs photonic crystal slabs

3.1 Introduction

Ever since the introduction as materials that can inhibit spontaneous emission [5] or localize light [6], photonic crystals have been recognized as structures that are able to tailor the propagation of light [9, 10]. These photonic crystals consist of a dielectric material arranged on a periodic lattice with a lattice constant comparable to the wavelength of light. Nowadays, photonic crystals find application in high Q, small mode volume cavities, in slow-light waveguides and numerous other applications that make use of the intriguing linear optical properties of photonic crystals. The nonlinear optics of photonic crystals, in particular second harmonic generation (SHG) is less intensively researched. Nevertheless, photonic crystals are interesting for nonlinear optics since they may combine high field intensities with optical properties that can be tuned by structure design.

In order to achieve highly efficient second harmonic generation in a small volume, a material with a large effective nonlinear susceptibility $\chi_{eff}^{(2)}$ must be used and the phase-matching condition must be met [29]. The phase-matching condition ensures that all waves generated inside the material interfere constructively. In most materials this condition is not fulfilled due to the material dispersion, but phase matching can be achieved using birefringent materials. The main obstacle in using III-V materials such as GaAs and GaP, that respectively have a more than 70 and 30 times larger $\chi_{eff}^{(2)}$ than that of a BBO crystal [31,32], is the fact that GaAs and GaP are not birefringent and phase-

matching is not easily satisfied. Phase matching can be satisfied in a device with periodically alternating layers of low and high index of refraction or by periodically poling the orientation of the $\chi^{(2)}$ material. An existing phase mismatch can be compensated by adding or subtracting a suitable reciprocal lattice vector **G** resulting in what is called quasi-phase-matching [33, 43–45]. Second harmonic generation can be further enhanced significantly by a strong spatial confinement of both the fundamental and the SH optical fields [46], that enhances the field intensities. Two-dimensional (2D) photonic crystal slabs, i.e., slabs of dielectric GaAs material perforated with a lattice of holes, are interesting in this respect.

Cowan et al. [47] show theoretically how to exploit the leaky modes of a freestanding 2D photonic crystal slab to achieve both quasi-phase-matching and strong spatial confinement. The authors predict an enhancement of SH signal in reflection of more than 6 orders of magnitude.

Mondia et al. [48] investigate experimentally SHG in reflection from a 2D square lattice of holes in GaAs supported on an Al_2O_3 cladding layer. The authors use very short (150 fs) pulses and vary the angle of incidence and the frequency of the fundamental beam. This enables them to make both the fundamental and the SH wave resonant with the leaky modes of the structure. In this quasi-phase-matched configuration they achieve a SH enhancement of more than 1200 times compared to the noise level in the experiment. Torres et al. [49] present a theoretical and experimental study of SHG in reflection from a 1D GaN photonic crystal. They report a SH enhancement of more than 5000 times, compared to an unpatterned GaN slab, when the quasi-phase-matching condition is satisfied.

We study in this chapter the influence of leaky modes at both the fundamental and SH frequency on SHG in reflection from a *freestanding* 2D photonic crystal slab, i.e., a slab that is surrounded by air on both sides. In principle, this would lead to a stronger confinement of the field and may therefore lead to more efficient SHG compared to earlier experiments. The photonic crystal consists of a regular 2D square array of holes drilled in ~ 150 nm thick slab of $Al_{0.35}Ga_{0.65}As$ material. Compared to earlier experiments in literature we use a narrow linewidth pulsed laser at 1.535 μm and tune the angle to probe the resonant coupling of both the fundamental and SH wave to the modes of the structure and how this affects the SH signal. We measure a SH enhancement of more than 4500 × compared to the signal from the photonic crystal away from resonance, and a SH enhancement of 35000 × relative to the second harmonic signal from the unpatterned $Al_{0.35}Ga_{0.65}As$ region on the wafer. These enhancements are significantly larger compared to enhancements

reported in References [48,49]. We measure our largest enhancement when the fundamental beam is slightly off-resonance. This shows the importance of the resonant coupling occurring at the SH frequency (quasi-phase-matching) and hints at the fact that the enhancement may be much larger in a structure that is doubly resonant.

3.2 Fabrication of photonic crystals

The photonic crystal samples, investigated in this chapter, consist of a free-standing slab perforated with a two-dimensional square lattice of holes. The starting point of the fabrication process, similar to that of Ref. [50], is the heterostructure shown in Fig. 3.1(a), grown along the <100> lattice direction of the GaAs crystal [51]. The purpose of the fabrication procedure is to create a large, freestanding slab made out of $Al_{0.35}Ga_{0.65}As$ perforated by a regular array of holes. A cross-section of this structure is shown in Fig. 3.1(b). The composition of the slab layer is chosen to render the structure optically trans-parent at both the fundamental (1535 nm) and second harmonic wavelength (767.5 nm).

The fabrication procedure starts with spin coating a ~ 500 nm thick layer of a positive-tone e-beam resist, ZEP 520A [52], on top of the heterostructure. The two-dimensional square lattice of holes is defined in the resist using e-beam lithography. To ensure a nonzero efficiency for second harmonic generation, the ΓX direction of the photonic lattice is rotated relative to the crystallo-graphic <100> direction of the underlying GaAs by an angle of $\sim 22.5°$. In this case, the incident electric field of the fundamental is never along a crystallographic axis of the GaAs wafer and the effective nonlinearity is nonzero. Collinear second harmonic generation along one of the crystallographic directions is forbidden due to the $4\bar{3}m$ symmetry of the GaAs lattice.

After e-beam exposure, the exposed resist is removed by developing for 80 sec. in n-amyl acetate and rinsing for 30 sec. in 9:1 methyl isobutyl ketone:isopropyl alcohol solution. The developed resist then serves as an etch mask for transferring the pattern to the silicon nitride (SiN_x) layer using anisotropic reactive ion etching (RIE) in a CHF_3/Ar plasma. In this process a RF power of 50 W, a pressure of ~ 6 μbar and CHF_3 and Ar flow rates of 25 sccm are used. The etch rate of the SiN_x layer is ~ 15 nm/min and the selectivity of the process is better then 10:1. After the pattern transfer, a low pressure RIE with an oxygen plasma is used to remove the residual e-beam resist.

Using the silicon nitride as a mask, the hole pattern is then etched deep
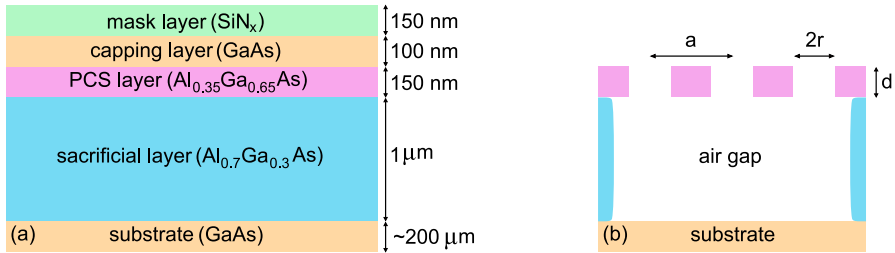
Figure 3.1. (a) Heterostructure used for fabrication of photonic crystal slabs. Photonic crystal slabs are made in the 150 nm thick $Al_{0.35}Ga_{0.65}As$ layer. The silicon nitride layer provides the mask for etching the hole pattern (defined by e-beam lithography) deep into the $GaAs/Al_xGa_{1-x}As$ layers. After removing the sacrificial layer a free-standing structure is achieved. (b) Schematic cross-section of a free-standing photonic crystal slab with lattice constant a, radius of the holes r and thickness d.

into the $GaAs/Al_xGa_{1-x}As$ layers in a chlorine-based RIE etch [53]. The flow rates of BCl_3, Cl_2, and N_2 are set to 15, 7.5, and 10 sccm, respectively. A pure chlorine plasma leads to isotropic etching of the GaAs. This can be compensated by adding a sufficient amount of nitrogen to the plasma to passivate the sidewalls during the etching process. This way, near vertical etch profiles can be realized, ensuring straight holes in photonic crystal layer [54]. The RF power and pressure are 100W and ~ 4.5 μbar respectively and the selectivity of the process is better than 10:1. Afterwards, the remaining silicon nitride mask is removed using the CHF_3/Ar RIE as described earlier.

The 100 nm thick GaAs capping layer, on top of the structure, that protects the AlGaAs layers from oxidizing, is removed in a 3:1 citric acid:H_2O_2 solution* etch for 2 minutes [55]. The GaAs layer is etched ~ 100 times faster then the underlying $Al_{0.35}Ga_{0.65}As$ layer. In order to obtain reproducible results, any oxide layer residing on top of the capping layer should be removed prior to the etching process by dipping the structure in 15:1 deionized H_2O:buffered oxide etch (BHF) solution for 15 seconds. Figure 3.2 shows a structure for which the removal of the GaAs is incomplete. The etching process is faster along the {100} crystallographic planes resulting in a square feature around every hole. From this image, the intentional $\sim 22.5°$ misalignment of the photonic and the crystal lattice of GaAs is clearly visible.

After removing the sacrificial $Al_{0.7}Ga_{0.3}As$ layer in a 1:4 HF (40%):H_2O

---

*The citric acid solution is made by mixing citric acid monohydrate with deionized water 1:1 by mass. The obtained solution is then mixed with a 31% H_2O_2 solution.

solution for 1 minute [50], critical point drying is used to remove the sample from the liquid, resulting in a freestanding photonic crystal slab. The samples for this chapter were fabricated using the facilities of the Kavli Nanolab Delft.

In this chapter, we investigate four freestanding photonic crystal slabs with the same lattice constant, but with a slightly different radius-to-pitch ratio r/a of the holes. These samples were created by writing the same pattern with e-beam using different exposures. Figure 3.3 shows an SEM image of sample D4 that was exposed with an electron dose of 250 μC/cm^2. From this image we find that the lattice constant $a = 890\pm2$ nm. An analysis of $\sim$ 1000 holes shows
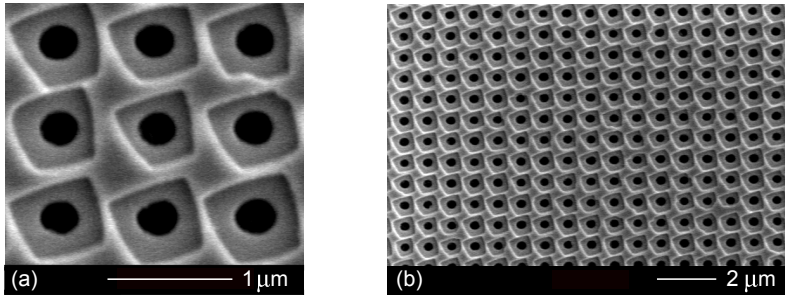

Figure 3.2. (a) and (b) SEM images of a photonic crystal sample with partially removed GaAs capping layer. Square feature around every hole arises from the fact that GaAs etches preferentially along the {100} crystallographic planes. The photonic lattice is rotated with respect to the crystal lattice of GaAs.
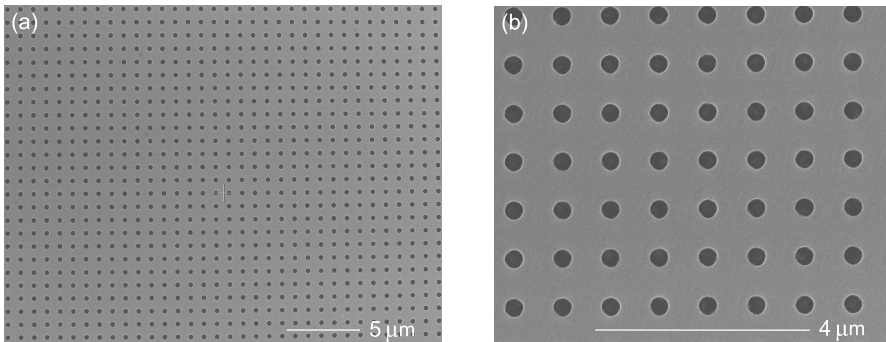

Figure 3.3. (a) and (b) Scanning electron micrographs showing the top view of freestanding photonic crystal slab D4. The entire structure covers an area of $\sim 300 \times 300$ μm^2. The radius of the holes is 160.9 nm, and the lattice constant is 890 nm.

that the radius of the holes is a normal distribution with an average radius of 160.9 nm and a standard deviation $\sigma = 1.6$ nm. The relevant parameters of photonic crystals D1–D4 are summarized in Table 3.1. As can be seen from the table, the hole size increases with electron dose. Varying the e-beam dose is a good way to fine tune the r/a ratio of a photonic crystal [56]. Samples D2, D3, and D4 have a similar distribution of hole sizes (equal σ) while D1 shows significantly more variation in hole size.

Table 3.1. Parameters of the photonic crystal slabs used in our experiments.

Sample label	dose [μC/cm^2]	a [nm]	r [nm]	Area [μm^2]
D1	220	890±2	144.1±3.2	$\sim 300 \times 300$
D2	230	-‖-	148.1±1.9	-‖-
D3	240	-‖-	154.6±2.0	-‖-
D4	250	-‖-	160.9±1.6	-‖-

3.3 Setup

The experimental setup used for both linear reflectivity and second harmonic generation is shown schematically in Fig. 3.4(a). All the measurements are done in a specular geometry where the angle of incidence θ_i is set by using a motorized stage.

3.3.1 Linear reflectivity

Two different white light sources are used to measure the linear reflectivity. A high power, fiber-coupled, Xenon lamp (Ocean Optics HPX-2000) is used in the infrared part of the spectrum ($\lambda \sim 900$–1700 nm) while a fiber-coupled Tungsten halogen lamp (Ocean Optics HL-2000-FHSA) is used at visible and near infrared wavelengths ($\lambda \sim 680$–900 nm). The advantage of the Tungsten over the Xenon lamp is that it has a flatter and more stable spectral output. The disadvantage of the Tungsten lamp is that it has less power in the infrared part of the spectrum. The white light coupled into a 50 μm multimode fiber (FIB.1) is collimated by lens L1 with a focal length of 50 mm. The collimated beam is then polarized by a Glan-Thompson polarizing beamsplitter cube (POL.) and focused on the sample by lens L2 with a focal length of 75 mm. Apertures AP.1 and AP.2 serve to modify the numerical apertures of both incident and collected beams. The reflected beam is collected and collimated
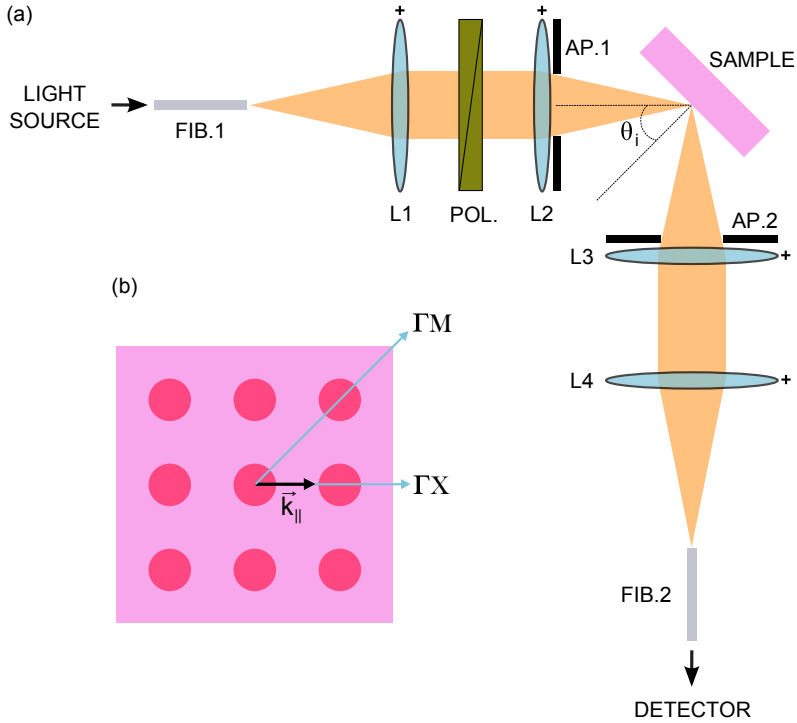
(a)

LIGHT
SOURCE

FIB.1

L1 POL. L2

AP.1

θ_i

SAMPLE

AP.2

L3

L4

FIB.2

DETECTOR

(b)

ΓM

ΓX

$\vec{k}_{||}$

Figure 3.4. (a) Setup used for both linear reflectivity and second harmonic generation. Light from an illumination source is coupled into a fiber (FIB.1) and focused on the photonic crystal sample at an angle of incidence θ_i. The reflected light is collected into a second fiber (FIB.2) and sent to a detector. The lenses L1–L4 serve to collimate and focus the light onto the sample. A polarizer (POL.) adjusts the polarization of the incident light. The apertures AP.1 and AP.2 can be used to reduce the numerical aperture of the incident and collected beams. (b) Schematic top view of a square lattice photonic crystal slab. Relevant symmetry directions are indicated as well as the parallel component of the wave vector $\mathbf{k}_{||}$.

by lens L3 (focal length of 75 mm), and focused by lens L4 (focal length of 50 mm) onto a 400 μm multimode fiber (FIB.2) and then sent to a fiber-coupled grating spectrometer.

More than one spectrometer is employed in order to cover both visible and infrared part of the spectrum ($\lambda \sim 680$–1700 nm). Ocean Optics USB2000 spectrometer (resolution ≈ 1.5 nm) is used for detection in the visible and near infrared part of the spectrum ($\lambda \sim 680$–900 nm) while Ocean Optics

NIR-512 spectrometer (resolution ≈ 3nm) is used for the infrared part of the spectrum ($\lambda \sim$ 900–1700 nm).

3.3.2 Second harmonic generation

For SHG we slightly modify the setup shown in Figure 3.4(a). A Q-switched diode-pumped solid state laser (Cobolt Tango), with Er:Yb-doped glass as gain medium, is now used as the source of illumination. This laser has a specified center wavelength of 1535 ± 1 nm and a narrow linewidth, < 0.04 nm. The laser has a 5 kHz repetition rate with a typical pulse duration of ≈ 3.8 ns (full width at half maximum). The average power of the laser is ~ 25 mW and high peak power pulses (~ 1.3 kW) are generated. Light from the laser is coupled into a 9.5 μm single-mode fiber instead of the 50 μm multimode fiber used for linear reflectivity measurements.

The second harmonic generated in reflection is detected with either Ocean Optics USB4000 spectrometer (resolution ≈ 1.3 nm) or an Apogee Alta U1 Peltier cooled CCD camera. The CCD camera is used to detect very low second harmonic signals since it has much higher sensitivity compared to the fiber-coupled spectrometers.

3.4 Linear optical characteristics

The optical modes of a two-dimensional photonic crystal slab can be classified as truly guided modes and leaky modes (or guided resonances) [57]. Truly guided modes are the modes guided in the slab by total internal reflection. For these modes, all diffraction orders from the photonic crystal lattice are confined to the guiding layer as well. As a result, these modes remain confined to the slab and decay exponentially outside the slab. Leaky modes are the modes guided in the slab by total internal reflection that can couple to the environment via diffraction. In this case, at least one diffraction order from the photonic crystal lattice can propagate in the surrounding medium. Therefore, leaky modes can escape the slab and couple to the external radiation.

An effective way to investigate the leaky modes and their dispersion relation is to measure specular reflection spectra as a function of angle of incidence [58, 59]. Each guided resonance will appear as a resonant feature in the reflection spectrum on top of a slowly oscillating background [60]. Figure 3.5 shows a plot of the measured reflection for sample D4 as a function of frequency on the vertical axis and the in-plane wave vector $k_{||}$ on the horizontal axis. Data are shown for s-polarized (Fig. 3.5(a)) and p-polarized (Fig. 3.5(b)) light. In the experiment the angle of incidence θ_i is varied from 30° to 70° in
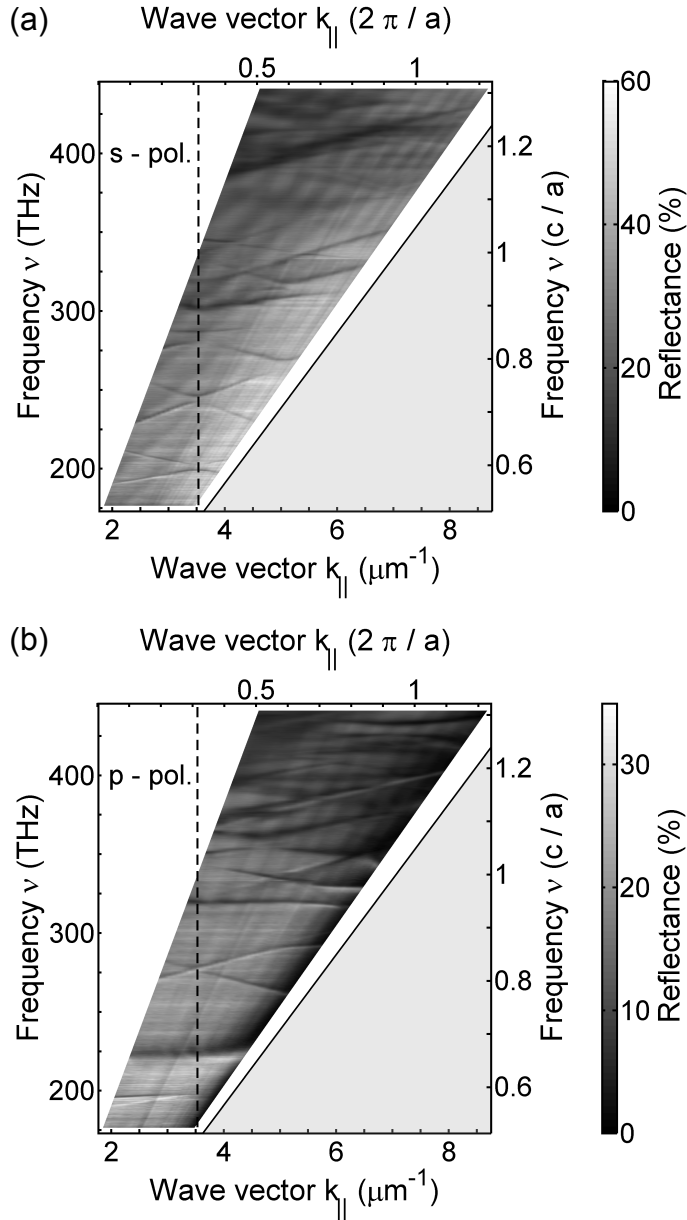
Figure 3.5. Gray scale plot of the measured reflection as a function of frequency (vertical axis) and wave vector $k_{||}$ (horizontal axis) for sample D4. Measurements are shown for s- (a) and p-polarized (b) incident light, and reveal the presence of several leaky modes. The gray shaded area below the light line (solid line) is where the truly guided modes exist.

steps of 1°. In order to facilitate a comparison with a dispersion relation $\nu(k_{||})$, the angles of incidence are converted to the in-plane wave vectors using the expression $k_{||} = (2\pi\nu/c)\sin\theta_i$, where θ_i are the angles of incidence, as shown in Figure 3.4(a). The sample is oriented in such a way that the in-plane wave vector, $\mathbf{k}_{||}$, is along the ΓX symmetry direction of the photonic crystal lattice. The incident light beam is focused to a spot of ~ 75 μm with a numerical aperture ~ 0.025. Several sharp resonant features can be observed in the figure indicating the dispersion of leaky modes. The gray shaded area below the light line ($\nu = ck_{||}/(2\pi)$) is the region of the truly guided modes.

In order to understand the position of the leaky modes, we calculated the band structure of the leaky modes using a freely available finite difference time domain (FDTD) package*. In the calculation, the slab has a radius of the holes $r/a = 0.18$, a thickness $d/a = 0.13$, and a relative permittivity $\epsilon = 10$. These parameters correspond to those of sample D4. For simplicity, we assume that the photonic crystal material is lossless and dispersionless and use a literature value [62] of the permittivity of $Al_{0.35}Ga_{0.65}As$ at a wavelength of 1500 nm. It is well-known that below the electronic band gap, the permittivity increases with frequency. Therefore, we expect that the calculated modes are slightly blue-shifted for larger frequencies compared to a calculation that takes into account dispersion. This is a relatively small effect in the frequency range where we compare the calculated band structure with measured data.

Figure 3.6 shows the calculated band structure of leaky modes plotted on top of the experimental reflectivity data for sample D4. We restrict ourselves to frequencies ν below 300 THz for clarity. Calculations are shown for both H-even (TE-like) and E-odd (TM-like) modes.

In the calculation, the 2D square lattice is positioned in the xy-plane and a point dipole source is placed in the middle of the photonic crystal slab at $z = 0$. The modes of a photonic crystal slab can be classified by their E-field, which is either *even* or *odd* with respect to the mirror-symmetry plane at $z = 0$. Even modes have the H-field in the z-direction, while odd modes have the E-field in the z-direction. In the case of an unpatterned waveguide slab, these modes correspond to the fundamental transverse electric (TE) and transverse magnetic (TM) modes. Note however, that this definition of TE and TM is relative to a plane of continuous translational symmetry, perpendicular to the slab; e.g., the $x = 0$ plane. This continuous translational symmetry is broken in a 2D photonic crystal slab and the optical modes cannot be labeled as TE and TM modes [63]. We will refer to these modes as a TE- and TM-like mode

---

*We use finite difference time domain package MEEP (MIT Electromagnetic Equation Propagation) [61], that can be found at http://ab-initio.mit.edu/wiki/index.php/.
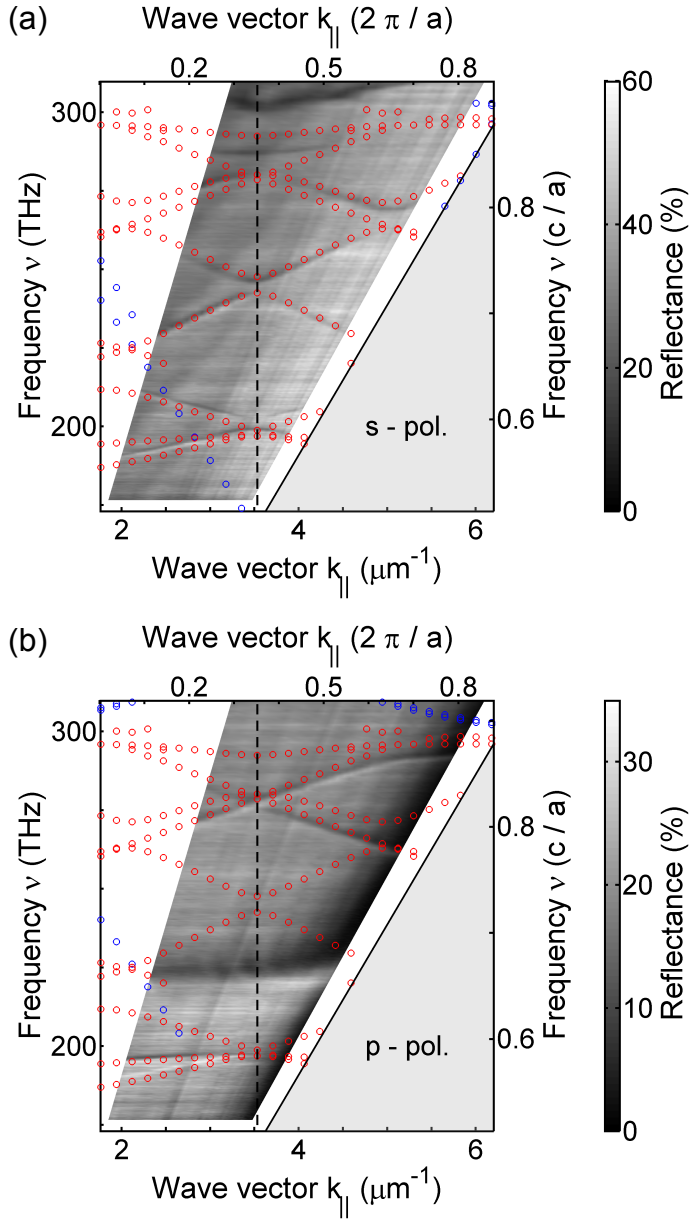
Figure 3.6. Calculated dispersion of leaky modes plotted on top of the experimental reflectivity data of Fig. 3.5 for s- (a) and p-polarized (b) light. The red and blue circles correspond to H-even (TE-like) and E-odd (TM-like) leaky modes, respectively.

to emphasize the resemblance of these modes to those of an unpatterned slab.

As can be seen, the calculated and the experimental data are in good agreement. From the figure we conclude that there is no coupling to TM-like leaky modes in this frequency range while a number of TE-like leaky modes are visible in the experimental data for both s- and p-polarized incoming light.

External radiation couples to the guided resonances of the photonic crystal via diffraction by adding a reciprocal lattice vector $\mathbf{G}$ to the in-plane wave vector $\mathbf{k}_{||}$. We define the wave vector of the incident light in the xz-plane, with the x-axis parallel to the ΓX direction of the photonic lattice. Each leaky mode can be labeled by the reciprocal lattice vector (G_x, G_y) involved in the coupling of the incoming light to the leaky mode.

In order to understand the coupling of the incident light to a leaky mode one needs to understand the symmetry of these modes in the plane of incidence. In our case, the plane of incidence is the $x = 0$ plane of mirror symmetry of the photonic crystal. The E-field of the leaky modes is either odd or even relative to this plane. Note that this definition of odd or even is an additional symmetry in addition to the mirror symmetry of the $z = 0$ plane discussed before. The E-field of the incoming s- or p-polarized light is either odd or even relative to the $x = 0$ plane. This determines the coupling of light to the slab modes.

Let us first consider the coupling to $(\pm 1, 0)$ and $(0, \pm 1)$ modes. At non-normal incidence all degeneracy of these modes is lifted. The (-1, 0) and (+1, 0) modes show strong dispersion and propagate in the direction of the incoming wave vector. These TE-like modes are odd with respect to the $x = 0$ plane and couple to s-polarized light. The $(0, \pm 1)$ modes propagate in and out of plane direction, and as a consequence have a weaker dispersion. The lower energy $(0, \pm 1)$ mode is a superposition of a $(0, +1)$ and $(0, -1)$ mode with odd symmetry relative to the $x = 0$ plane and couples to s-polarization. The high energy $(0, \pm 1)$ mode is even and couples to p-polarization [64]. This is indeed what is observed in Fig. 3.6. In the experimental data for s-polarization (Fig. 3.6(a)), going from low to high frequencies, we see a lower energy $(0, \pm 1)$ mode, a $(-1, \pm 1)$ mode, a crossing of $(1, 0)$ and $(-2, 0)$ modes, and a crossing of $(1, \pm 1)$ and $(-2, \pm 1)$ modes. The (-1, 0) mode is too low in frequency to be observed in the experiment. In p-polarization (Fig. 3.6(b)), we see a higher energy $(0, \pm 1)$ mode, a $(-1, \pm 1)$ mode with low Q (not resolved with MEEP calculation*), and a crossing of $(1, \pm 1)$ and $(-2, \pm 1)$ modes.

Sample D4 was designed in such a way to enable the coupling of a s-

---

*To eliminate the non-resonant contribution MEEP analyzes the field after a number of optical cycles. This excludes the contribution from modes with a low Q factor.

polarized fundamental beam at frequency $\nu_F = 195.44$ THz to one of the first leaky modes. From Figure 3.6(a), it is evident that the fundamental can resonantly couple to the structure by exciting the lower energy $(0, \pm1)$ mode. In order to determine for which value of the in-plane wave vector $k_{||}$ this is achieved we have to extract the dispersion of this leaky mode from the experimental reflectivity data.

Figure 3.7 shows reflection spectra of sample D4 for s-polarized incident light and various values of $k_{||}$. Each reflection spectrum contains sharp resonant features superimposed on top of a smooth background. The asymmetry of the (Fano) resonances is a result of an interference between a direct (non-resonant) and indirect (resonant) channel, as was first described by Fano [65, 66]. Light in the non-resonant channel is Fresnel reflected from the slab, while light in the resonant channel couples to a leaky mode of the structure and after some time "leaks" back into the environment. Fan et al. [60]
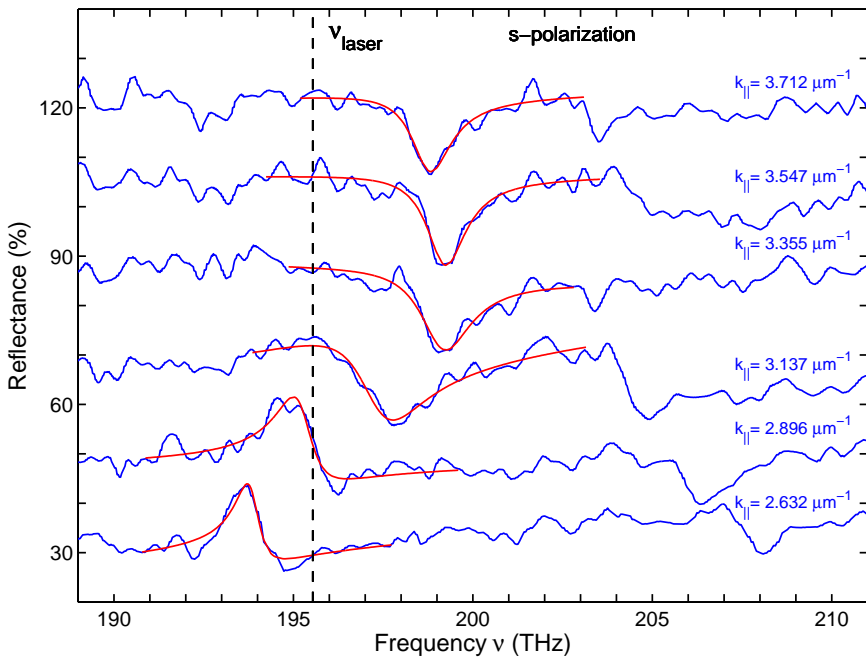

Figure 3.7. Experimental reflection spectra of sample D4 (blue curves) for s-polarized incident light and different values of $k_{||}$. Measured resonant features corresponding to the lower energy $(0, \pm1)$ leaky mode are well fitted with asymmetric Fano lineshapes (red curves). Black dashed line indicates the fundamental frequency.

have developed a general temporal coupled-mode theory of the Fano resonance for a single-mode optical resonator coupled with multiple input/output ports. A photonic crystal slab can be treated as a single-mode optical resonator with two ports, one at each side of the structure. Light, can be transported from one port to the other using both a non-resonant and a resonant channel. The resonant channel is characterized by a frequency ν_0 and a time τ. We define the escape rate of a resonance as $\Gamma = 1/(2\pi\tau)$ and the quality factor of a resonance as $Q = \nu_0/(2\Gamma)$. For a symmetric two port system, e.g., a freestanding photonic crystal slab in air, the reflectance R as a function of frequency ν is given by

$$R = \left| r_D + \Gamma \frac{-r_D \mp it_D}{i(\nu - \nu_0) + \Gamma} \right|^2, \tag{3.1}$$

where r_D and t_D are the Fresnel reflection and transmission coefficients of the slab. The subscript "D" is used to denote the direct channel. The $\mp$ sign is due to exciting either *even* (-) or *odd* (+) leaky mode with respect to the plane of mirror-symmetry going through the middle of the slab ($z = 0$).

For a lossless system, the asymmetric Fano lineshape given by equation (3.1) reaches both 0% and 100%. In realistic systems, losses are present. These losses are either due to the absorption of the slab material or scattering from imperfections of the structure. Driessen et al. [67] have extended the coupled-mode theory of the Fano resonance by adding an extra port to include losses in the system. It is assumed that energy in the photonic crystal resonator is transferred irreversibly to the loss port and is characterized by a loss rate γ. The resonant Fano features in the experimental data, for a freestanding photonic crystal slab in air, can be described using the following expression for the reflectance R:

$$R = \left| r_D + \Gamma \frac{-r_D \mp it_D}{i(\nu - \nu_0) + \Gamma + \gamma} \right|^2. \tag{3.2}$$

In order to fit the measured Fano resonances corresponding to the lower energy $(0, \pm 1)$ leaky mode (Fig. 3.7), the expression (3.2) is rewritten in the following form:

$$R = \left| c_1 + c_2\nu - \frac{c_3 + ic_4}{i(\nu - \nu_0) + \gamma + \Gamma} \right|^2, \tag{3.3}$$

where c_1, c_2, c_3, c_4, ν_0 and $\gamma + \Gamma$ are fit parameters. Here, we assume that the direct channel contribution to the total reflection, in the vicinity of a resonance, can be approximated with a linear function of the frequency ν. As can be seen from Fig. 3.7, the obtained fits show a good agreement with the experimental data. The importance of this approach is that we can extract the dispersion

(ν_0 as a function of $k_{||}$) and the quality factor ($Q = \nu_0/(2(\Gamma + \gamma))$) as a function of $k_{||}$) of a leaky mode directly from the experimental data. Figure 3.8 shows the dispersion of the lower energy $(0, \pm 1)$ leaky mode of sample D4 (blue dots). The frequency of the fundamental is indicated by the red dashed line in the figure. The green dash-dot line defines a constant angle of incidence $\theta_i = 46°$. From this figure it is clear that the s-polarized fundamental beam couples resonantly to a leaky mode at an angle of incidence $\theta_i = 46°$, corresponding to $k_{||} = 0.417 \times 2\pi/a$. A typical quality factor $Q = \nu_0/(2(\Gamma + \gamma))$ of this leaky mode, as determined by the Fano model, is ~ 175.
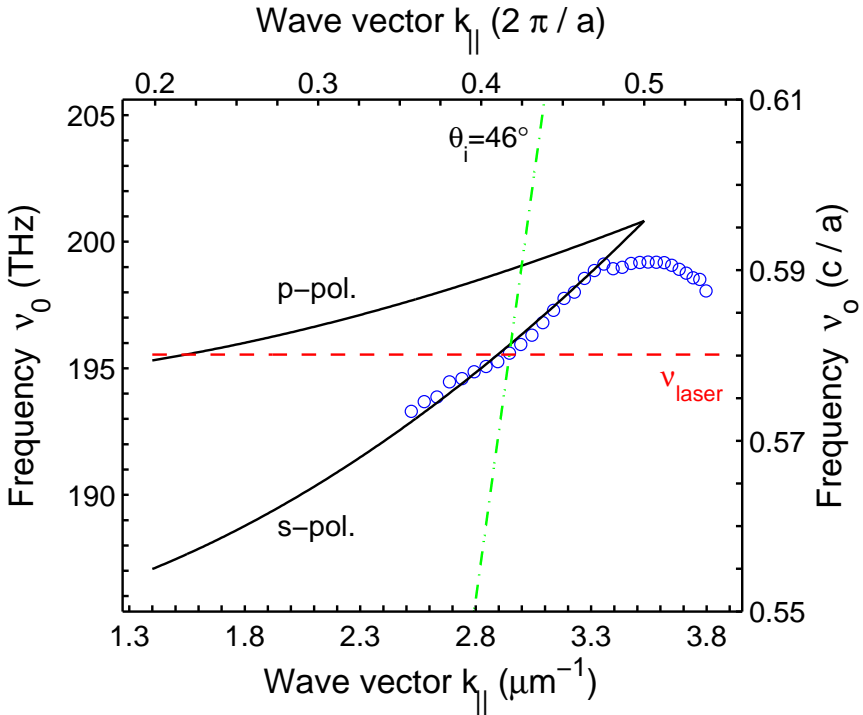

Figure 3.8. Measured dispersion of the lower energy $(0, \pm 1)$ leaky mode of sample D4 (blue dots). The red dashed line indicates the position of the fundamental frequency, and the green dash-dot line corresponds to a constant angle of incidence $\theta_i = 46°$. Resonant coupling of the s-polarized fundamental beam to the $(0, \pm 1)$ leaky mode occurs at an angle of incidence $\theta_i = 46°$. A simple analytical model, based on a nearly free photon picture (see text), is used to calculate the dispersion of both the lower and the higher energy $(0, \pm 1)$ leaky mode (black curves).

A simple analytical model, that describes the dispersion (ν_0 as a function of $k_{\parallel}$) of the $(0, \pm 1)$ leaky modes, can be derived. In a nearly free photon picture, the light line of a uniform dielectric medium with an effective refractive index n_{eff} is folded back to the first Brillouin zone by adding an appropriate reciprocal lattice vector. For the hypothetical case of a slab with infinitely small holes, the $(0, \pm 1)$ modes are degenerate. However, in a real photonic crystal slab, these modes split due to a standing wave pattern generated by the two counter-propagating $(0, \pm 1)$ modes. The lower energy $(0, \pm 1)$ mode has the maximum of the electric field in a high refractive index region, while the higher energy $(0, \pm 1)$ mode has the maximum of the electric field in a low refractive index region. The dispersion of the $(0, \pm 1)$ modes can be successfully approximated by only considering the interaction between the two $(0, \pm 1)$ modes. The frequencies $\nu_{0\pm}$ of the modes are given by

$$\nu_{0\pm}(k_x) = \nu_c(k_x) \pm \Delta\nu(k_x)/2, \tag{3.4}$$

where ν_c is the center frequency, $\Delta\nu$ is the splitting between the modes, and k_x is the component of the incoming wave vector parallel to the interface in the ΓX direction. The center frequency $\nu_c(k_x)$ is given by

$$\nu_c = \frac{c}{2\pi n_{eff}} \cdot \left(\left(\frac{2\pi}{a} \right)^2 + \frac{1}{2} k_x^2 \right)^{1/2}, \tag{3.5}$$

and the splitting $\Delta\nu(k_x)$ between the two modes is given by:

$$\Delta\nu = \Delta\nu\left(k_x = 0\right) \cdot \left(\frac{a}{\pi} \right)^2 \cdot \left(\left(\frac{\pi}{a} \right)^2 - k_x^2 \right). \tag{3.6}$$

Here $\Delta\nu(k_x = 0)$ is the splitting at normal incidence that we obtain from the FDTD calculation. We find values of $n_{eff} = 2.52$ and $\Delta\nu(k_x = 0) = 0.029 \times c/a$.

3.5   Nonlinear optical properties

Figure 3.9 shows the measured power of the signal at a frequency of 390.88 THz (twice the fundamental frequency) as a function of the fundamental power (blue dots), generated in sample D4 and measured in reflection. A typical spectrum of the SH signal, measured with a fiber-coupled spectrometer, is shown in the inset. In order to achieve a dynamic range of ≈ 5 orders of magnitude, the detection scheme is changed by replacing the spectrometer with a silicon CCD camera. To make sure that we detect only the light at
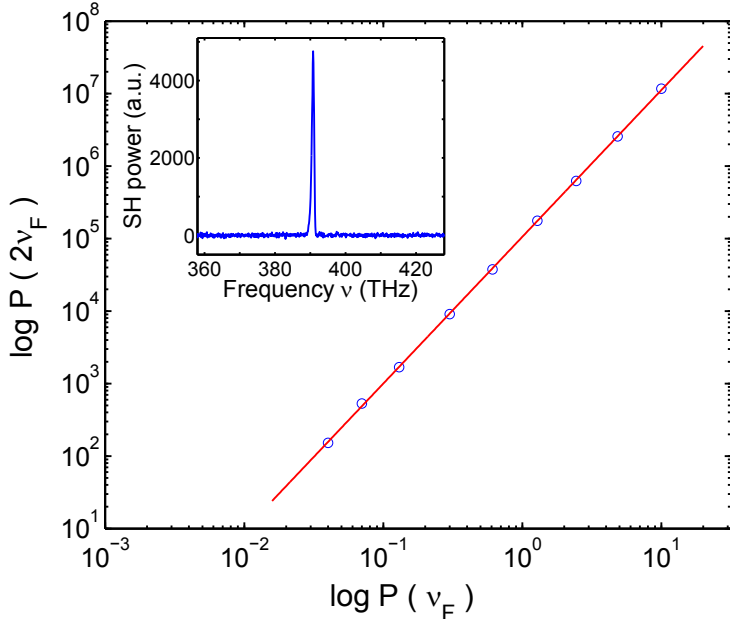
Figure 3.9. Measured power of the signal at a frequency of 390.88 THz as a function of the fundamental power (blue dots), generated in sample D4, and measured in reflection. The linear fit (red line) has a slope of 2.025 and confirms the quadratic power dependence. The inset shows a typical spectrum of the SH signal.

390.88 THz a bandpass filter with a center frequency of 391.17 THz and a full width at half maximum of 5.41 THz is placed in front of the CCD camera. The incident fundamental beam is clipped by an aperture and focused to a spot of $\sim 35\ \mu$m with a numerical aperture of ~ 0.05. The power dependence measurement is done at a constant angle of incidence and polarization of the incident beam. As can be seen in the figure, the generated power at twice the fundamental frequency is proportional to the square of the fundamental power.

Figure 3.10 shows the second harmonic power (blue dots) generated by the s-polarized fundamental beam inside sample D4, as a function of the in-plane wave vector $k_{||}$. The in-plane wave vector $k_{||}$ is parallel to the ΓX symmetry direction of the photonic crystal lattice. The fundamental beam is clipped by an aperture and focused to a spot of $\sim 75\ \mu$m with a numerical aperture ~ 0.025, and the second harmonic signal is detected using a fiber-coupled grating spectrometer. We varied the angle of incidence θ_i from $39°$ to $52°$
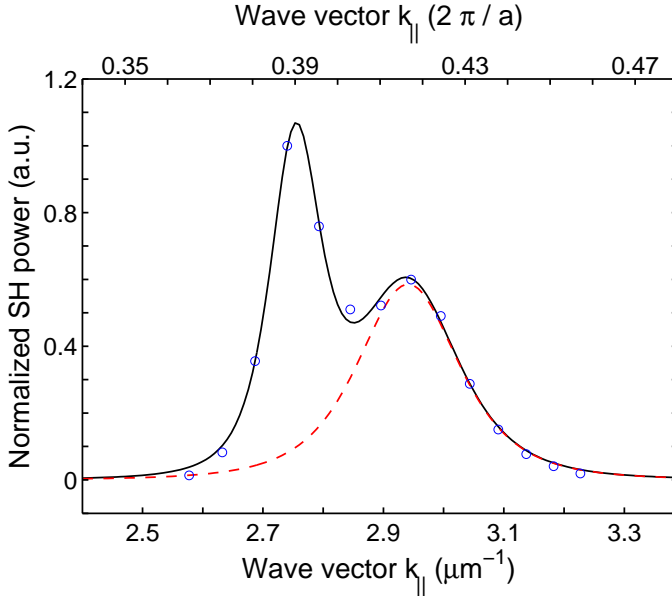
Figure 3.10. Second harmonic power (blue dots) generated by the s-polarized fundamental beam inside sample D4, and measured in reflection as a function of the in-plane wave vector $k_{||}$. Two distinct peaks in the SH power imply that two different resonant effects occur in the SHG. The measured SH power can be fitted with two Lorentzian-squared functions (black line). The red dashed line indicates the contribution to the SH due to a resonant coupling of the fundamental to the lower energy $(0, \pm 1)$ leaky mode. The remaining contribution is due to a resonant coupling of the generated SH to a leaky mode of the structure.

in steps of $1°$ and converted this to the in-plane wave vectors $k_{||}$ using the expression $k_{||} = (2\pi\nu/c) \sin\theta_i$.

The measured second harmonic power for sample D4 shows two distinct peaks, implying that there are two different resonant effects that give rise to SH. The lower peak, occurring at $k_{||} = k_{||F} = 0.417 \times 2\pi/a$, is due to the resonant coupling of the fundamental to the lower energy $(0, \pm 1)$ leaky mode, as can be seen in Fig. 3.8. On resonance, we expect that the largest part of the fundamental power couples to the photonic crystal slab yielding the largest SH power. The power at the fundamental frequency ν_F inside the slab is given by

$$P_{in\ slab}(\nu_F, k_{||}) \propto \frac{\Gamma(k_{||})^2}{(\nu_F - \nu_0(k_{||}))^2 + (\Gamma(k_{||}) + \gamma(k_{||}))^2}, \qquad (3.7)$$

where ν_0, Γ and γ are the center frequency, escape and loss rates of the lower energy $(0, \pm1)$ leaky mode respectively. Assuming that the parameters Γ and γ are slowly varying functions of $k_{||}$ for the range of in-plane wave vectors used in the SHG experiment, expression (3.7) becomes:

$$P_{in\ slab}(\nu_F, k_{||}) \propto \frac{1}{(\nu_F - \nu_0(k_{||}))^2 + (\Gamma + \gamma)^2}. \qquad (3.8)$$

Since the center frequency ν_0 can be approximated well with a linear function of $k_{||}$ for the range of in-plane wave vectors used in the SHG experiment (Fig. 3.8), we rewrite expression (3.8) as:

$$P_{in\ slab}(\nu_F, k_{||}) \propto \frac{1}{(k_{||F} - k_{||})^2 + \left(\frac{\Delta_F}{2}\right)^2}. \qquad (3.9)$$

Thus, the fundamental power inside the photonic crystal slab as a function of $k_{||}$, can be described with a Lorentzian function peaked at $k_{||F}$ with a full width at half maximum (FWHM) Δ_F. The position of the peak, $k_{||F}$, is determined by the dispersion of the leaky mode, and the width of the Lorentzian, Δ_F, is determined by the quality factor of the mode. For the second harmonic power generated in the photonic crystal we write:

$$P_{in\ slab}(2\nu_F, k_{||}) \propto \left(\frac{1}{(k_{||F} - k_{||})^2 + \left(\frac{\Delta_F}{2}\right)^2}\right)^2. \qquad (3.10)$$

The measured SH power can be fitted with two Lorentzian-squared functions of the form (3.10), as shown by the black line in Fig. 3.10. The peaks are positioned at $k_{||SH} = 0.390 \times 2\pi/a$ and $k_{||F} = 0.417 \times 2\pi/a$, and have a width $\Delta_{SH} = 0.011 \times 2\pi/a$ and $\Delta_F = 0.022 \times 2\pi/a$. The dashed red line in Figure 3.10 shows the contribution to the SH due to the resonant coupling of the fundamental to the lower energy $(0, \pm1)$ leaky mode at $k_{||} = 0.417 \times 2\pi/a$.

The remaining contribution to the SH cannot be explained by considering only the resonance at the fundamental frequency. The fundamental beam is off-resonance at $k_{||} = 0.390 \times 2\pi/a$ (Fig. 3.8), where we measure the highest SH signal. We suggest that there is a contribution to the SH signal due to the resonant coupling of the generated wave at the second harmonic frequency to one of the leaky modes of the photonic crystal slab. Unfortunately, we are not able to identify a specific leaky mode in either the reflectivity measurements or in the MEEP calculation. At higher frequencies, the band structure becomes very complex due to the large number of bands involved and strong

interaction between them. In fact, a measurement of second harmonic using a tunable laser might be a better way to characterize the leaky modes at higher frequencies.

Figure 3.11 shows a comparison of the nonlinear optical response of samples with slightly different radius-to-pitch ratio r/a of the holes. The SH signal is measured in reflection as a function of the in-plane wave vector $k_{||}$ for samples D1 (pink), D2 (green), and D3 (blue dots). The curves are offset vertically by a constant value for clarity. The experimental data for sample D4 (red dots), as discussed earlier, are shown in the figure as well.

We observe that the second harmonic signal shifts to larger values of $k_{||}$ as the ratio r/a decreases. This effect can be understood by considering a nearly free photon picture. In this picture, a decrease in the ratio r/a results in an increase of the effective refractive index of the slab (n_{slab}) and shifts the dispersion of the leaky mode ($\nu \propto k_{||}/n_{slab}$) towards lower frequencies. As a consequence, the fundamental beam becomes resonant with the photonic crystal at a larger value of the in-plane wave vector $k_{||}$. The black arrows in the figure indicate the values of $k_{||}$, estimated from experimental linear reflectivity data, for which the fundamental beam is exactly on resonance.

As can be seen from the figure, the signals from samples D1 and D2 are very comparable. This is due to the fact that these samples have the same pitch and almost equal hole size. The main difference between the samples is that sample D1 has a larger variation in the hole size compared to other samples (Table 3.1).

For all samples, the SH is generated over a relatively large range of $k_{||}$ and cannot be explained by considering only the coupling of the fundamental beam to the structure. It is clear from the dispersion of the lower energy $(0, \pm 1)$ leaky mode that the fundamental beam is "far away" from being exactly on resonance with either sample D1 or D2 in the region around $k_{||} = 0.5 \times 2\pi/a$. We believe, that resonant effects at second harmonic frequency provide an answer. Note that for these values of $k_{||}$ the leaky mode at the SH frequency is close to the edge of the first Brillouin zone, as indicated by the black vertical dash-dotted line in Fig. 3.11. Since the group velocity vanishes at the edge of the Brillouin zone, coupling to such a mode could lead to a very broad feature in the measured SH.

As a final note, we emphasize the presence of a peak in the SH signal occurring in the second Brillouin zone. To visualize this peak, we multiply the SH power generated in sample D4 for larger values of $k_{||}$, by a factor of 10. A weak peak occurs at $k_{||} \approx 0.57 \times 2\pi/a$ due to a higher order diffraction of the periodic lattice at the fundamental frequency. The magnitude of this peak is

much lower since the higher order diffraction event is less efficient.

The calculated enhancement of the SH signal for a similar geometry was found to be more than 6 orders of magnitude [47]. In order to estimate the SH enhancement for sample D4, we measured both the resonant and the non-resonant contribution to the SH signal generated in the sample, and calculated the ratio. The non-resonant contribution can be measured by tuning the $k_{||}$ in such a way that the waves at both the fundamental and the second harmonic frequency cannot resonantly couple to the structure. We are limited by the
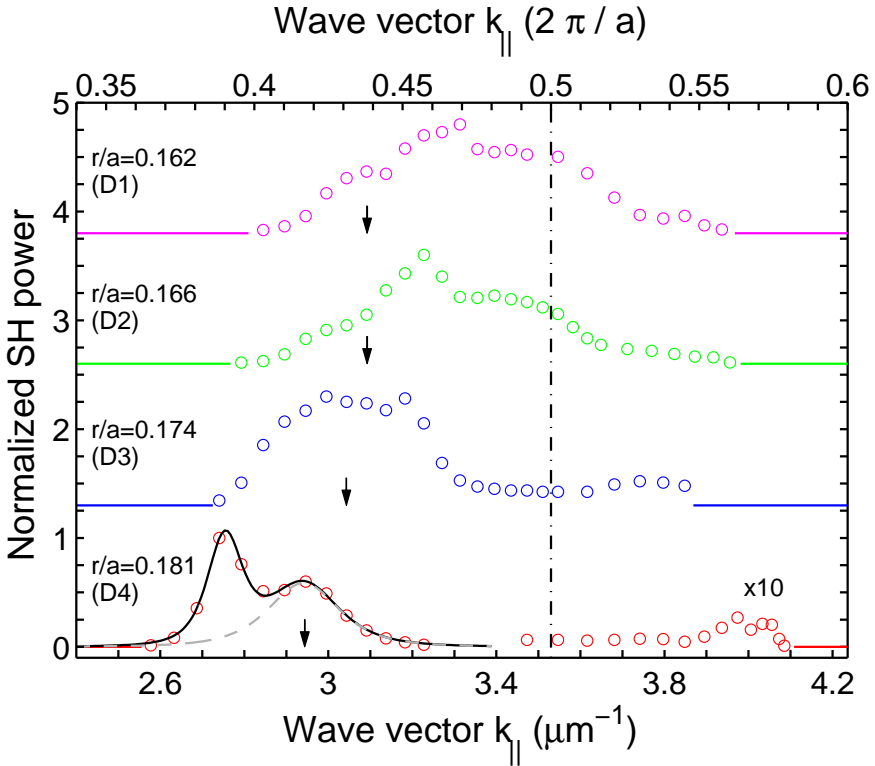

Figure 3.11. Second harmonic power measured in reflection as a function of the in-plane wave vector $k_{||}$ for samples D1 (pink), D2 (green), D3 (blue), and D4 (red dots). The curves are offset by a constant value for clarity. The black arrows indicate the values of $k_{||}$ for which the fundamental beam is exactly on resonance with the given structure. The vertical dash-dotted black line indicates the position of the edge of the first Brillouin zone. As the ratio r/a decreases, the SH signal shifts to the larger $k_{||}$.

noise floor of the spectrometer in measuring this contribution, and estimate a lower limit of the SH enhancement for sample D4 of 4500, which is almost 4 times larger than the maximal enhancement reported in Reference [48]. The maximal SH signal generated in reflection from sample D4 occurs at $k_{||}$ for which the fundamental is slightly off-resonance, as can be seen in Figure 3.10. This implies that even larger enhancements can be achieved for a structure that enables the resonant coupling at both the fundamental and SH frequency at the same time. Based on the fit with two Lorentzian-squared functions in Fig. 3.10, we estimate that the signal may be further enhanced by a factor of 10. We also compared the resonant SH generated in reflection from the sample to the SH generated in reflection from the unpatterned $Al_{0.35}Ga_{0.65}As$ region on the wafer. A detection scheme with a very sensitive silicon CCD camera, described earlier, is used to detect low SH signal generated from the unpatterned region. The highest measured second harmonic signal from the photonic crystal slab is $9225 \pm 3 \times 10^3$ cts/s. The measured second harmonic signal from the unpatterned region is $0.26 \pm 0.03 \times 10^3$ cts/s. Therefore, the experimental SH enhancement is $35 \pm 4 \times 10^3$ times, which is 7 times larger than the enhancement reported in Reference [49] for 1D GaN structures.

3.6   Conclusion

Leaky modes at both the fundamental and the SH frequency play a prominent role in increasing the nonlinear optical response of a photonic crystal slab. By tuning the in-plane wave vector $k_{||}$ of the incident fundamental beam the structure can be resonantly excited, leading to large enhancements of second harmonic. We measure an enhancement > 4500 when compared to the photonic crystal slab off-resonance, and a factor 35000 compared to an unpatterned substrate.

The observation of two distinct peaks in the SH signal generated in sample D4 can be explained with the resonant coupling at both the fundamental and the SH frequency. In fact, the largest SH enhancement for sample D4 occurs when the fundamental beam is slightly off-resonance, and we estimate that the SH can be enhanced by another factor 10. To investigate the enhancement in more detail, a better understanding of the leaky modes at the SH frequency is needed. An interesting new route to investigate the influence of the modes at the SH frequency on the SHG would be to design and make a photonic crystal slab that has one of the first leaky modes at the SH frequency. In this way, the coupling of the fundamental to the structure can be neglected and all the features in the SH signal can be attributed to resonant effects at SH

frequency.

CHAPTER 4

Method to transfer photonic crystals to a transparent gel substrate

4.1 Introduction

Over the last two decades, the continuous expansion of the field of photonic crystals went hand in hand with developments in semiconductor nanofabrication techniques. Since the introduction of photonic crystals as structures that can form a complete band gap to inhibit spontaneous emission [5], or localize light [6], many novel properties of these fascinating materials have been found and experimentally realized. Today, photonic crystals are recognized as structures that offer remarkable control of light propagation and enhanced light-matter interaction. As such, they find applications in lasers, single photon emitters, waveguides, filters, optical nonlinear devices, sensors, and slow light media [9–11]. So far, combining various devices into a single chip has proven to be a very difficult task, since it requires different materials and fabrication techniques.

In this chapter we propose a novel technique to transfer a semiconductor based photonic crystal device to any substrate. The main idea is to stick the structure to a transparent gel film. This gel can then be glued to the desired substrate. If needed, the substrate can have additional patterning in order to add functionality to the system. In contrast to wafer bonding techniques, a dedicated machine is not needed and the interfaces do not have to be polished to an optical quality. This may significantly reduce the time and resources needed to fabricate the desired structure, which is extremely important in the early stage of prototype development where trial and error are often used as

an approach to solve the fabrication issues.

The proposed technique can be used for optical frequency converters based on photonic crystal slabs in III-V semiconductor materials that possess high second-order nonlinearity such as GaN, GaP, or $Al_xGa_{1-x}As$. Current III-V technology allows epitaxial growth of nearly lattice matched AlGaAs layers on GaAs. For a freestanding membrane with a large surface area, the lattice mismatch between the membrane layer and the substrate causes buckling of the membrane. The buckling leads to lower optical quality of the structure. This issue can be overcome by transferring the freestanding membrane to a transparent gel substrate to release the strain.

We have successfully transferred large freestanding $Al_{0.35}Ga_{0.65}As$ photonic crystal membranes ($\sim 300 \times 300~\mu m^2$) to a transparent gel substrate with a low refractive index of $n_{gel} = 1.4$. In contrast to the freestanding structure, the membrane on gel is almost flat and the transparent substrate enables transmission measurements. The introduction of the low index substrate results in a red shift of the frequencies of the leaky modes. A simplified coupled mode theory based on a truncated plane wave method [68] in two-dimensions is used to describe an avoided crossing between three modes in our system. Due to the interaction, one of the modes becomes subradiant and reaches Q values of 300, limited by the finite size of our membrane, which demonstrates the excellent optical quality of our structures.

Compared to a similar system patterned in silicon nitride [69], our structures are mechanically more robust and they have a larger index contrast. Therefore, ultrahigh-Q nanocavities in $Al_{0.35}Ga_{0.65}As$ that are transferred to the gel might provide a more promising platform for biochemical sensing in liquid phase [70] than those in silicon nitride membranes. For comparison, a silicon nitride device immersed in water has an index contrast of 1.71 at a wavelength of 780 nm [69], while an index contrast of ≥ 2 is needed to create a band gap for the guided modes [71–73]. The index contrast for the $Al_{0.35}Ga_{0.65}As$ membrane in water is 2.56, and for the $Al_{0.35}Ga_{0.65}As$ membrane on the gel substrate is 2.44, at a wavelength of 780 nm [62]. Both of them exceed what is possible with silicon nitride and the contrast is large enough to create a complete band gap. This enables defect cavities with a high quality factor and a small modal volume for sensing applications.

Another possible application of our technique would be to provide high extraction efficiency for light-emitting diodes (LEDs). In this application a photonic crystal layer with a large index contrast is placed on top of an LED [74] using our transfer technique. Without a photonic crystal layer, the light that is not emitted in the extraction cone is guided in the cladding material. If

not collected from the edges of the structure, the guided modes are lost. By adding a photonic crystal layer with properly chosen parameters, it becomes possible to diffract large part of guided light into the extraction cone. The advantage of our method is that this layer can be made independently in a separate fabrication stage using a completely different technology. By using the large index contrast of the photonic crystal, a much more strongly diffracting layer is created when compared to existing structures with a small periodic surface corrugations [74].

Our technique could be used to position a gallium phosphide (GaP) membrane with a cavity on a flat diamond substrate with nitrogen-vacancy centers (N-V centers) as an alternative to using a nanodiamond with a single N-V center [75]. These N-V centers in bulk diamond can be isotropically pure and can be positioned using ion implantation [76]. Moreover, such N-V centers have low decoherence [77, 78] which may be important for future applications in quantum information.

4.2   Sample preparation

We fabricated two-dimensional photonic crystal slabs with a square lattice of holes with a hole radius of ~ 150 nm and a lattice constant $a = 820$ nm using a combination of e-beam lithography and reactive ion etching techniques in a commercially grown AlGaAs layer structure [51]. The samples were fabricated using the facilities of the Kavli Nanolab Delft. An overview of the fabrication process is shown in Figure 4.1. The layers in this study are deposited using a MOCVD (metalorganic chemical vapor deposition) process on a $< 100 >$ GaAs substrate and consist of a 1 μm thick Al rich $Al_{0.7}Ga_{0.3}As$ layer, a 150 nm thick Ga rich $Al_{0.35}Ga_{0.65}As$ layer, and a 100 nm thick GaAs capping layer. To create the hole pattern, a 150 nm silicon nitride layer is deposited on top of the structure and serves as a mask during the final reactive ion etching step. The lattice of holes is created by e-beam lithography in a ~ 500 nm thick layer of positive tone e-beam resist, ZEP 520A [52], as shown in Figure 4.1(a). A low pressure reactive ion etching step in a CHF_3/Ar plasma is used to transfer the hole pattern into the nitride mask. After removal of the e-beam resist in a low pressure O_2 plasma, the hole pattern is etched deep into the AlGaAs heterostructure in a $BCl_2/Cl_2/N_2$ reactive ion etch process at 100 W RF power, a pressure of ~ 4.5 μbar and flow rates of 15, 7.5, and 10 sccm respectively. The nitrogen flow in this process was optimized to create near vertical side walls of the holes. After etching the holes, the nitride mask is removed using the CHF_3/Ar etching procedure described above.
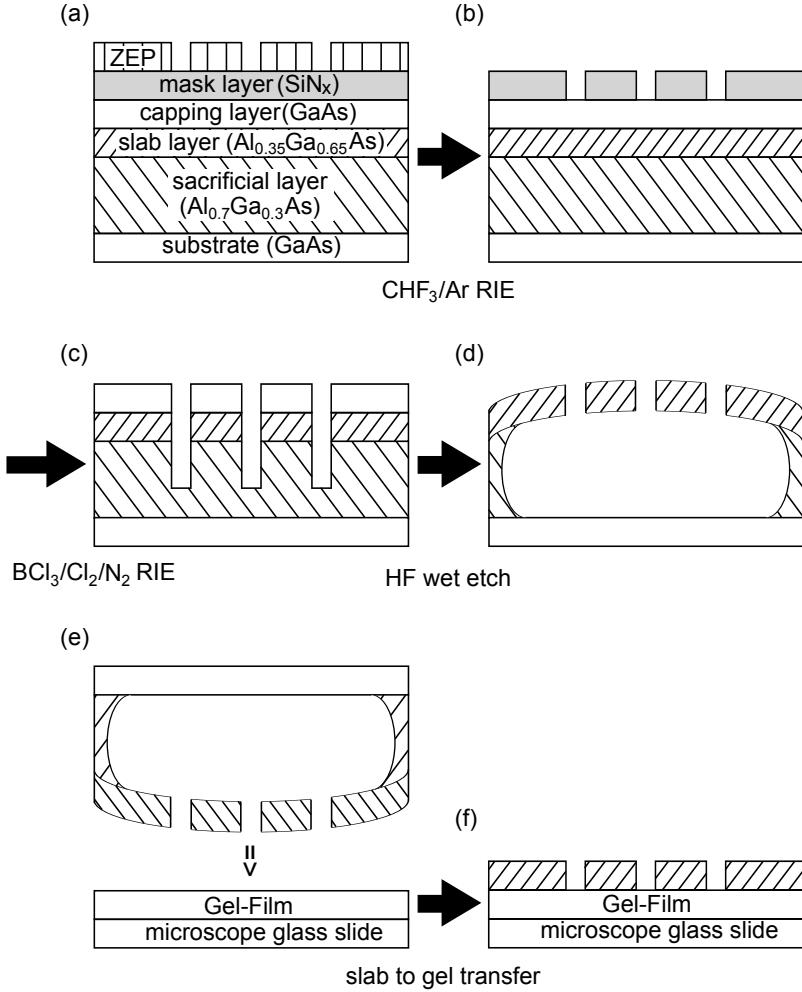
Figure 4.1. Overview of the fabrication process of a photonic crystal slab: (a)-(c) A regular two-dimensional square lattice of holes is created in the AlGaAs/GaAs heterostructure by using e-beam lithography and reactive ion etching. (d) Wet etching techniques are employed to remove both the capping and the sacrificial layer, creating a freestanding photonic crystal slab in air. Due to a small lattice mismatch between the GaAs substrate and the $Al_{0.35}Ga_{0.65}As$ layer, the slab buckles. (e) The photonic crystal slab is then transferred to a gel substrate fixed onto a microscope glass slide. (f) The resulting structure is an almost flat membrane on a transparent substrate (gel) with a low refractive index $n_{gel} = 1.4$.

To create a freestanding membrane we first remove any residual oxide layer by dipping the sample in 15:1 deionized H_2O:buffered hydrofluoric acid (BHF) solution for 15 sec. The sample is then placed in a 3:1 citric acid:H_2O_2 solution for 120 sec to selectively remove the GaAs capping layer. Finally, the freestanding membrane is created by etching the sacrificial $Al_{0.7}Ga_{0.3}As$ layer in a concentrated 1:4 HF (40%):H_2O solution for 60 sec followed by a rinsing step in pure water and critical point drying. The resulting membrane covers an area of $\sim 300 \times 300$ μm^2 and is not perfectly flat due to a small lattice mismatch between the $Al_{0.35}Ga_{0.65}As$ ($l = 0.565603$ nm) membrane layer and the GaAs ($l = 0.565325$ nm) substrate [79]. This lattice mismatch of about 0.05% causes a compressive strain in the membrane. After etching the sacrificial layer, the freestanding photonic crystal slab buckles releasing the strain. The buckled membrane is symbolically depicted in a form of a bent slab in Figure 4.1(d).

In the end, the membrane is transferred to a transparent gel layer [80] with a refractive index of 1.4 on a standard microscope slide. The sample is gently placed on the gel using tweezers, and the GaAs substrate is carefully peeled off. As a result, an almost flat photonic crystal slab is created, as shown in Figure 4.1(f).

Figures 4.2(a) and (b) show the optical images of a photonic crystal slab before and after the transfer, respectively. As can be seen, a few cracks occur along the sample surface depending on how gently the slab is placed on the gel. Typically, there is a damage free area on the sample that is larger than $\sim 200 \times 200$ μm^2. In addition to the structures with the lattice constant $a = 820$ nm, the hole radius $r \sim 150$ nm, and the area $A \sim 300 \times 300$ μm^2, we have transferred samples with $a = 960$ nm, $r \sim 270$ nm, and a surface area $A \sim 425 \times 425$ μm^2, and samples with $a = 350$ nm, $r \sim 100$ nm, and $A \sim 425 \times 425$ μm^2. Out of about 25 transferred membranes, only about 5 had significant damage or folds from the transfer process. Considering that in those ~ 5 cases the transfer was not done very carefully, we conclude that the $\sim 80\%$ yield can be increased by taking more care during the transfer process. Equally important, membranes that have collapsed onto the substrate during the fabrication process, can be picked up with the gel layer and used in experiments. This demonstrates the robustness and versatility of our technique, and suggests that samples could be made without the use of critical point drying.

Figures 4.2(c) and (d) show the interference microscope images of the slab at a wavelength of 549 nm, before (c) and after (d) the transfer, demonstrating that the structure on the gel is flatter. The equidistant fringes next to the sample in Figure 4.2(c) result from a small angle between the glass slide and
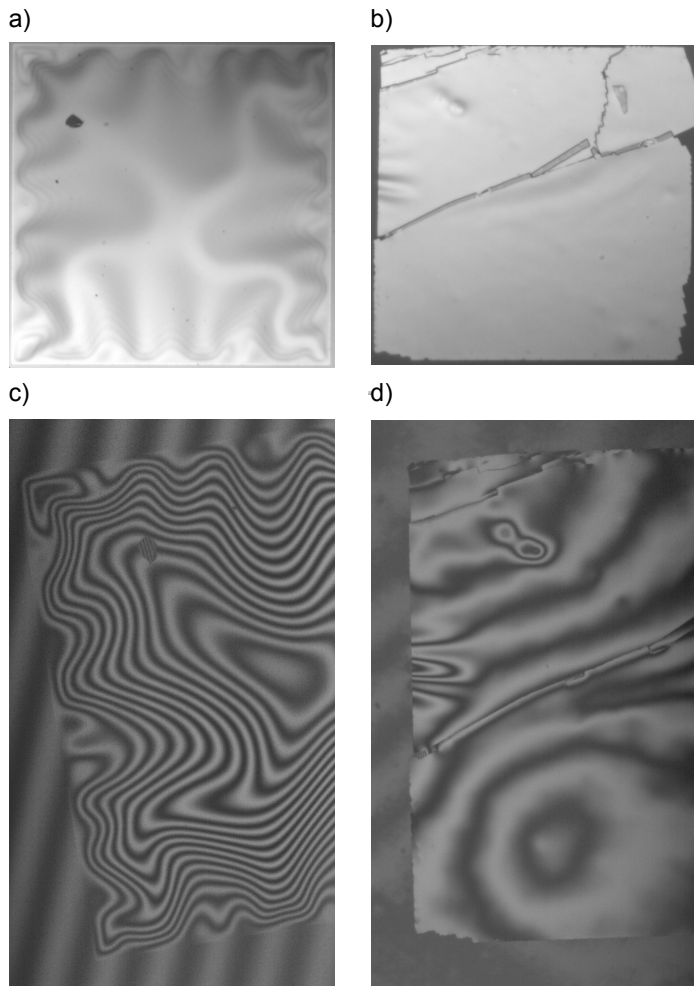
a)

b)

c)

d)

Figure 4.2. Optical microscope images of a freestanding photonic crystal slab (a) and the same photonic crystal slab after being transferred to the gel substrate (b). The sample size is $\sim 300 \times 300 \ \mu\text{m}^2$. Interference microscope images of the photonic crystal slab before (c) and after (d) placement on the gel showing that the structure on the gel is flatter. The height difference between a neighboring dark and white fringe is 274.5 nm.

the holder of the microscope. To estimate an upper limit for height differences along a membrane before and after the transfer, we count the fringes along the sample diagonal from the edge to the center of the structure. For a typical sample, we estimate the maximum height difference to be $\sim 10~\mu$m for a freestanding membrane and $\sim 1~\mu$m for a membrane on a gel. This shows that the membranes not only survive the transfer, but also become significantly flatter.

4.3 Experiment

We perform reflection and transmission measurements for wavelengths between 650 and 1700 nm using white light from a lamp coupled to a 50 μm multimode fiber. The output of this fiber is imaged onto the sample with a 1.5 times magnification to create a 75 μm spot on the sample. Apertures in the beam limit the numerical aperture of the incident beam to NA ~ 0.025. The reflected/transmitted light is collected into a 400 μm fiber and then sent to a fiber-coupled grating spectrometer. A silicon CCD array spectrometer (Ocean Optics USB2000) with a spectral resolution of ≈ 1.5 nm is used for detection in the visible and near-infrared part of the spectrum ($\lambda \sim 650$–900 nm). For the infrared part of the spectrum ($\lambda \sim 900$–1700 nm), we use an InGaAs array spectrometer (Ocean Optics NIR512) with a ≈ 3 nm spectral resolution. A Glan-Thompson polarizing beamsplitter cube is placed in a parallel part of the beam and is used to measure the reflectivity and transmissivity for *s*- and *p*-polarized light as a function of wavelength and angle of incidence.

The experimental setup for measuring the linear reflection spectra is identical to the setup shown in Figure 3.4(a) of Chapter 3. The linear transmission spectra are measured by aligning lenses L3 and L4 to collect the transmitted light rather then the reflected light.

4.4 Results and Discussion

4.4.1 Leaky modes of photonic crystal slabs before and after the transfer to the gel substrate

Figure 4.3 shows typical experimental reflection spectra of a photonic crystal slab before (blue circles) and after (red circles) the transfer to the gel. The measurements are done with *p*-polarized light incident at an angle of 35° along the ΓX symmetry direction of the square lattice. The reflection spectra consist of sharp resonant features superimposed on a slowly oscillating background.
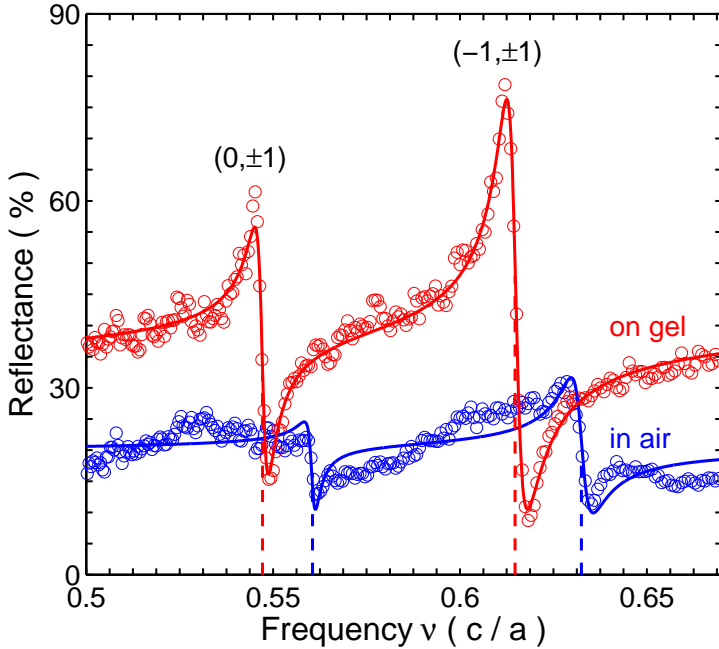
Figure 4.3. Measured reflection spectra of the slab suspended in air (blue circles) and transferred on the gel (red circles). The solid lines are obtained by fitting a Fano model (described in the text) to the experimental data. The dashed lines indicate the center frequencies of the p-polarized $(0,\pm1)$ and $(-1,\pm1)$ modes, as determined from the fit.

The two resonances in the spectra are the p-polarized $(0,\pm1)$ and $(-1,\pm1)$ leaky modes. A red shift of the resonances is observed after the transfer to the gel. Each leaky mode is labeled by the dimensionless reciprocal lattice vector (G_x, G_y) that is involved in the coupling of the incoming light to the leaky mode. This notation assumes that the plane of the periodicity is parallel to the xy-plane of the Cartesian coordinate system, with the ΓX symmetry direction of the square lattice parallel to the x-axis. Furthermore, we consider an experimental geometry in which the component of the incoming wave vector along the z-axis is perpendicular to the sample, and is denoted as $\mathbf{k}_\perp$. The component of the incoming wave vector in the xy-plane is labeled as $\mathbf{k}_{||}$.

It is clear from the measured spectra that the resonant features for the membrane on the gel substrate are more prominent than those for the freestanding membrane. The main reason for this is the removal of the highly-reflective GaAs substrate. In the case of the freestanding structure, the GaAs

substrate and the membrane act as two mirrors and form a Fabry-Perot cavity with air in between. The observed waviness of the membrane introduces variations in the distance between the substrate and membrane, which are much larger than $\lambda/4$. This creates strong variations in the reflected amplitude of the non-resonant contribution. Illuminating with a large spot is equivalent to averaging over all the substrate to membrane distances, and as a consequence the resonances in the reflection spectra for the freestanding slab have lower visibility compared to the slab transferred to the gel.

To quantify the red shift of the resonances due to the transfer to the gel we fit a Fano model to the measured reflectivity spectra (solid lines in Fig. 4.3). Within this model, the reflectivity as a function of the frequency, $R(\nu)$, is given by [60, 67]

$$R(\nu) = \left| r_D + \sum_j \frac{r_{Rj}}{i(\nu - \nu_j) + \gamma_j + \Gamma_j} \right|^2, \tag{4.1}$$

where r_D represents the non-resonant (direct) contribution, and the sum represents the resonant contribution. Leaky mode j has an amplitude r_{Rj}, a center frequency ν_j, and an escape rate Γ_j. The loss rate γ_j in the model describes losses due to the absorption, higher order diffraction, and the scattering from imperfections of the structure [67]. Accordingly, the quality factor (Q_j) of the leaky mode is defined as $Q_j = \nu_j/(2(\Gamma_j + \gamma_j))$, and can be interpreted as the number of optical periods before the intensity of the mode decays by $e^{-2\pi}$ [68]. To fit experimental data, we assume that the amplitude of the direct contribution, in a small frequency region around the center frequency, can be approximated with a linear function of the frequency ν: $r_D = c_1 + c_2\nu$, and we allow the amplitude r_{Rj} to be a complex number.

From the fits to the measured data in Fig. 4.3 we find frequencies ν_j of 0.561 and $0.633 \times c/a$ for the freestanding structure, and 0.547 and $0.615 \times c/a$ for the structure transferred to the gel. This corresponds to a red shift of 2.5 and 2.8% for the $(0, \pm1)$ and $(-1, \pm1)$ mode. Qualitatively this red shift can be understood from a nearly free photon picture [69, 81, 82]. The leaky modes are due to the folded mode of the slab waveguide with an effective refractive index. When the slab is placed on a substrate with a higher refractive index, i.e., gel instead of air, this effective refractive index increases and a red shift is observed.

Although this waveguide model explains the physical origin of the frequency shift, it cannot be used directly for a quantitative description of the experimental data. The waveguide model does not contain a simple way to calculate the effect of the holes on the effective refractive index and does not take

into account the interaction between the modes. This issue can be resolved by comparing our experimental data with finite-difference time-domain (FDTD) calculations. We use a freely available software package called MEEP [61] to calculate the frequencies of the resonances for an infinite slab with parameters identical to the experimental structure. The calculations are performed for a structure with a lattice constant $a = 820$ nm, a radius of holes $r = 160$ nm, and a thickness of the slab $d = 122$ nm. For the refractive index of the slab material we use a value of 3.1975, which is the tabulated value for the refractive index of the $Al_{0.35}Ga_{0.65}As$ at a wavelength of 1.5 μm [62]. The refractive index of the gel is taken to be 1.4. Figure 4.4 shows the measured and the calculated dispersion relations for both the *s*- and *p*-polarized $(0,\pm1)$ modes, for a freestanding membrane and a membrane on the gel. The experimental
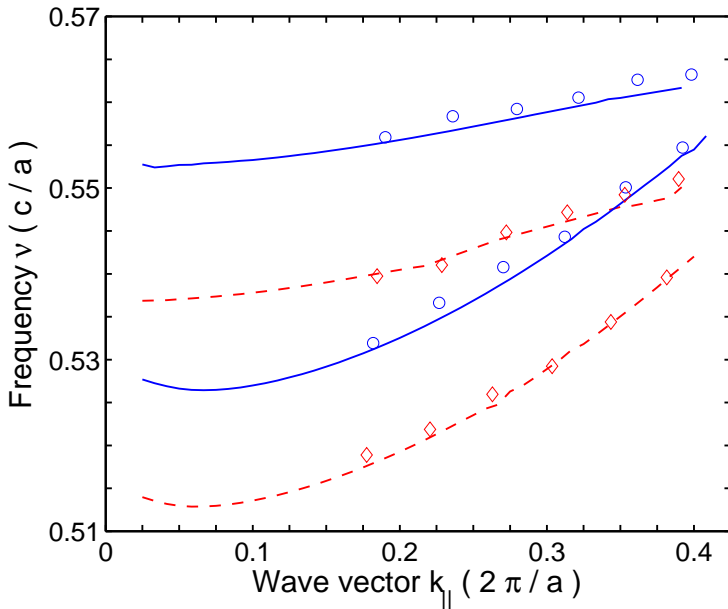

Figure 4.4. Measured (blue circles) and calculated (solid blue lines) dispersion relations of the two $(0,\pm1)$ modes, for a freestanding membrane. The *s*-polarized mode is lower in frequency than the *p*-polarized mode. Measured (red diamonds) and calculated (dashed red lines) dispersion relations of the two $(0,\pm1)$ modes, for the membrane transferred to the gel substrate. The calculations are performed for a structure with a lattice constant $a = 820$ nm, a radius of holes $r = 160$ nm, and a thickness of the slab $d = 122$ nm. The refractive indices of the slab material and the gel are taken to be 3.1975 and 1.4, respectively.

dispersion is obtained by fitting a Fano model of Equation 4.1 to the measured reflection spectra done at oblique angles of incidence with the wave vector $k_{||}$ along the ΓX symmetry direction of the square lattice. The *s*-polarized $(0, \pm 1)$ mode has a lower frequency than the *p*-polarized $(0, \pm 1)$ mode. As can be seen, the experimental data before (blue circles) and after (red diamonds) the transfer to the gel substrate agree very well with the calculated data for a slab in air (solid blue lines) and a slab with gel instead of air on one of the sides (dashed red lines), and shows a red shift of $\approx 2.5\%$ for the entire band. This uniform shift is consistent with the simple waveguide picture, where the presence of the gel increases the effective refractive index of the slab by $\approx 2.5\%$.

4.4.2 Interaction between the leaky modes of photonic crystal slabs transferred to a gel substrate

Transferring photonic crystal membranes to an optically transparent gel substrate creates flat structures that are ideally suited for transmission measurements. Figure 4.5 shows the measured transmission as a function of frequency (vertical axis) and wave vector $k_{||}$ (horizontal axis). Experimental data is shown for both *s*- (a) and *p*-polarized (b) light along the ΓX and the ΓM symmetry direction of the square lattice. The transmission spectra reveal many leaky modes also for higher order photonic bands. This demonstrates the excellent optical quality of the transferred structure. In this chapter we will limit the discussion to the lower frequency modes. For *s*-polarized light with $k_{||}$ along the ΓX symmetry direction, going from low to high frequencies, we observe the (-1,0), the (0,± 1), the (1,0), and the $(-1, \pm 1)$ leaky modes of the fundamental TE waveguide mode. For frequencies around $\sim 0.7 \times c/a$, we identify the (0,± 1) leaky mode of the fundamental TM mode close to the Γ-point. The TM mode interacts with the TE mode [82]. This TE-TM mixing together with higher order waveguide modes complicates the labeling of the modes for frequencies above $0.7 \times c/a$.

We will analyze the interaction between the (1,0) and (-1,± 1) leaky modes of the fundamental TE waveguide mode in detail. For a wave vector $k_{||}$ along the ΓX symmetry direction, the (1,0) mode couples to *s*-polarized radiation. Of the two (-1,± 1) modes, the low frequency mode couples to *s*-polarization, while the higher frequency mode couples to *p*-polarized radiation.

Figure 4.6 shows the measured transmission spectra for angles of incidence from 10° to 40° in steps of 1° (solid gray lines). The curves are vertically offset for clarity. We show the experimental data for the in-plane wave vector $k_{||}$ along the ΓX symmetry direction of the square lattice, for *s*- (a) and *p*-polarized (b) light. The data in Figure 4.6(a) shows a clear avoided crossing
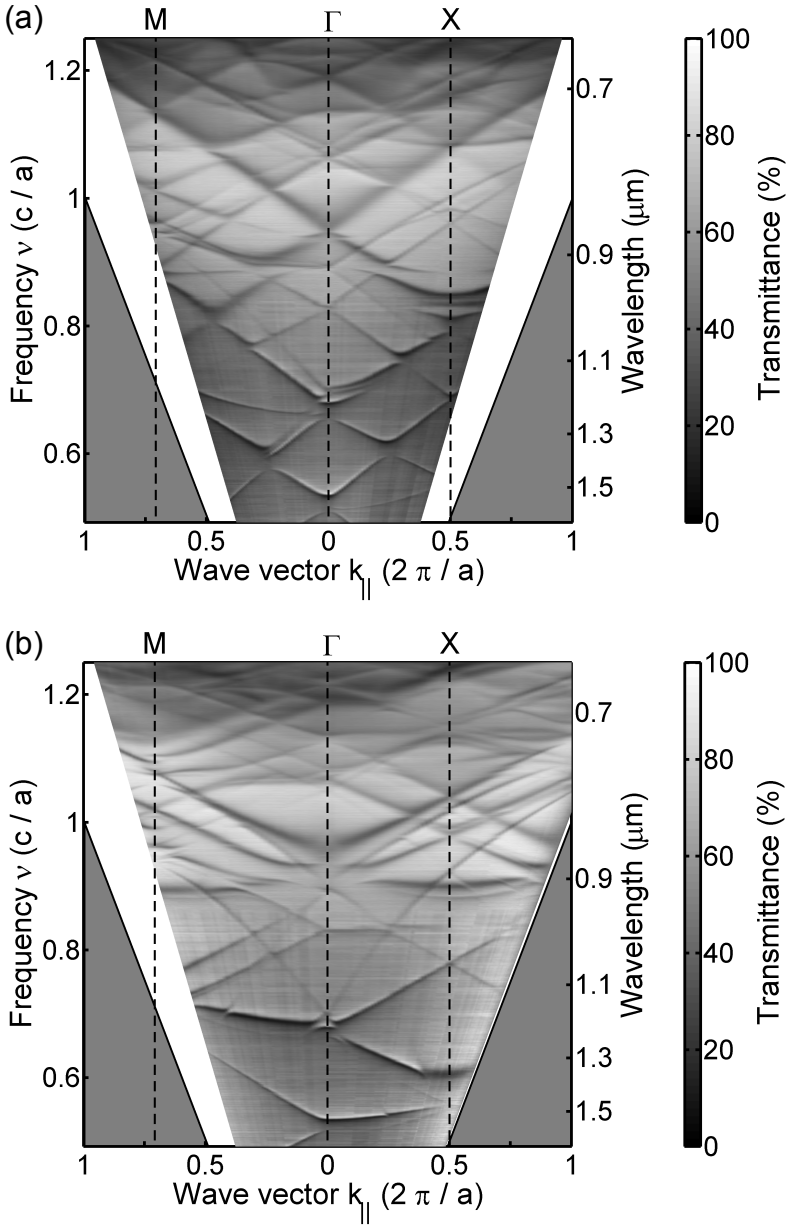
Figure 4.5. Gray scale plot of the measured transmission as a function of frequency (vertical axis) and wave vector $k_{||}$ (horizontal axis). Measurements are shown for *s*- (a) and *p*-polarized (b) incident light, and for the ΓX and the ΓM symmetry direction of the square lattice. The graphs reveal the presence of many leaky modes. The gray shaded area below the light line (solid line) is inaccessible in our experiment.
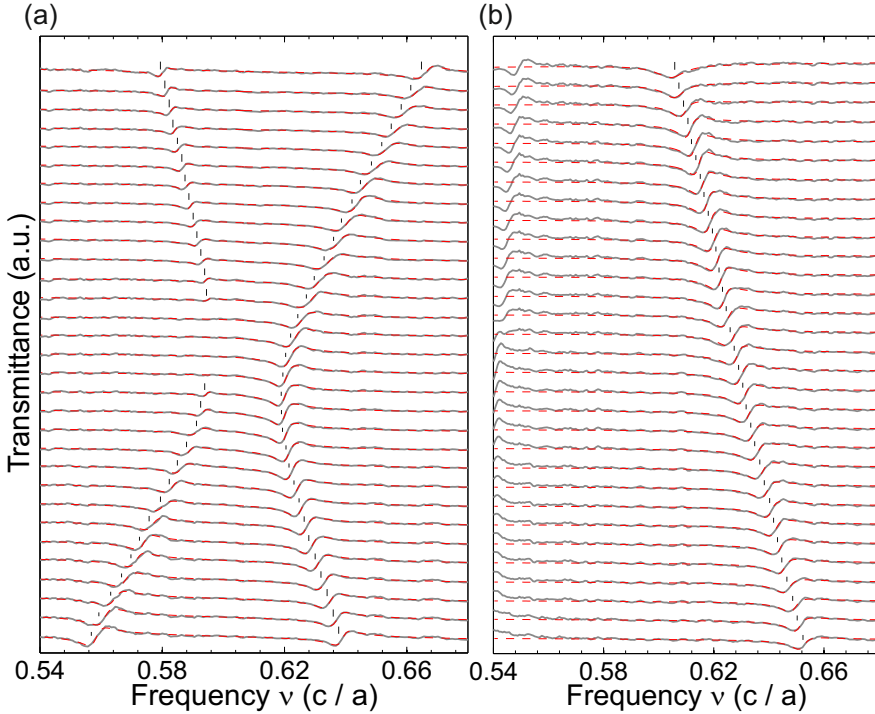
(a)   (b)

Figure 4.6. Measured transmission spectra (solid gray lines) for angles of incidence from 10° to 40° in steps of 1°, vertically offset for clarity. The experimental data are shown for wave vector $k_{||}$ along the ΓX symmetry direction and for s- (a) and p-polarization (b). The resonant features in transmission that correspond to (1,0) and (-1,±1) modes, are fitted with Fano lineshapes (dashed red lines). Indicating the position of the resonant frequencies, the black lines serve as guides to the eye, and demonstrate the avoided crossing between the s-polarized (1,0) and (-1,±1) mode.

between the s-polarized (1,0) and (-1,±1) modes.

The dashed red lines are fits to the data using the Fano model. As can be seen, this model describes very well the measured transmission spectra. By fitting the Fano lineshapes to the sharp features in the spectra, we obtain the dispersion relations and the quality factors of the leaky modes. The black lines indicate the fitted center frequencies, and serve to guide the eye. At the avoided crossing, the quality factor of the lower energy (1,0) mode increases while its amplitude decreases. As a result, this mode becomes subradiant and disappears from the spectra.

To gain insight and to get quantitative data for the avoided crossing of the modes, we introduce a simplified coupled mode theory that retains the essential symmetries of a complete band structure calculation. The interaction between the three modes can be described by a coupled mode theory featuring a 3×3 matrix of the following form:

$$H = \begin{pmatrix} \nu_1 & \kappa_1 & -\kappa_1 \\ \kappa_1 & \nu_2 + \kappa_2 & \kappa_2 \\ -\kappa_1 & \kappa_2 & \nu_2 + \kappa_2 \end{pmatrix}. \tag{4.2}$$

Here ν_1 and ν_2 are the frequencies of the unperturbed modes, that is the guided modes of a dielectric slab with an appropriate effective refractive index, without holes. The symmetry and the interaction between the three modes represented by this matrix is consistent with the nearly free photon picture introduced by Sakoda et al. [82]. The dispersion of these modes, $\nu(k_\parallel)$, can be obtained by folding the dispersion of the fundamental TE waveguide mode of the slab back to the first Brillouin zone by adding an appropriate reciprocal lattice vector. In this picture, ν_1 corresponds to the non-degenerate $(1,0)$ mode, while ν_2 corresponds to the twofold degenerate $(-1, \pm 1)$ modes. The coupling constant κ_1 characterizes the interaction between the s-polarized $(1,0)$ and $(-1, \pm 1)$ mode, while the coupling constant κ_2 characterizes the interaction between the two $(-1, \pm 1)$ modes.

The resonant frequencies of the leaky modes are given by the eigenvalues of the matrix H, and can be written as:

$$\nu_0 = \nu_2 + 2\kappa_2 \tag{4.3}$$

$$\nu_\pm = \frac{\nu_1 + \nu_2}{2} \pm \sqrt{\left(\frac{\nu_1 - \nu_2}{2}\right)^2 + 2\kappa_1^2}, \tag{4.4}$$

where ν_0 is the resonant frequency of the p-polarized $(-1, \pm 1)$ mode, ν_+ is the resonant frequency of the s-polarized $(-1, \pm 1)$ mode, and ν_- is the resonant frequency of the s-polarized $(1, 0)$ mode. The coupling between the s-polarized $(1,0)$ and $(-1, \pm 1)$ leaky mode, introduces the frequency splitting between the two modes equal to $2\sqrt{2}\kappa_1$ at $k_\parallel = G/4$ $(G = 2\pi/a)$.

Figure 4.7 shows the dispersion relations for the three modes obtained from the Fano fits of Fig. 4.6 (circles). The dashed lines represent the dispersion of the modes ν_1, ν_2 in the coupled mode theory. The resulting fit of the coupled mode theory to the experimental data is represented by the solid line and shows excellent agreement. The fitted values of the coupling constants are $\kappa_1 = 0.012 \times c/a$ and $\kappa_2 = 0.022 \times c/a$. This corresponds to a splitting

relative to the center frequency of the two uncoupled modes ($\nu_c = 0.608 \times c/a$) of $2\sqrt{2}\kappa_1/\nu_c = 5.6\%$ and $2\kappa_2/\nu_c = 7.2\%$. To reduce the number of fitting parameters, we assumed that both coupling constants are independent of the in-plane wave vector $k_{||}$.

In the coupled mode theory the uncoupled s-polarized $(1,0)$ and $(-1,\pm1)$ leaky modes follow dispersions of $\nu_1(k_{||})$ and $\nu_2(k_{||})$:

$$\nu_1(k_{||}) = \frac{1}{2\pi}\left((v_p - v_g)\frac{5G}{4} + v_g\left(k_{||} + G\right) \right), \tag{4.5}$$

$$\nu_2(k_{||}) = \frac{1}{2\pi}\left((v_p - v_g)\frac{5G}{4} + v_g\sqrt{\left(k_{||} - G\right)^2 + G^2} \right), \tag{4.6}$$

where the phase velocity and group velocity are defined as

$$v_p = 2\pi\left.\frac{\nu_w}{\beta_w}\right|_{\beta_w = \beta_{w0}}, \tag{4.7}$$

$$v_g = 2\pi\left.\frac{\partial\nu_w}{\partial\beta_w}\right|_{\beta_w = \beta_{w0}}. \tag{4.8}$$

Here the dispersion relation of the waveguide mode $\nu_w(\beta_w)$ is expanded in Taylor series around the point of the avoided crossing ($\beta_{w0} = 5/4 \times 2\pi/a$, ν_{w0}), and then folded back to the first Brillouin zone. From the fit we obtain the values for the phase velocity $v_p = 0.486 \times c$ and for the group velocity $v_g = 0.327 \times c$, where c is the speed of light in vacuum. Furthermore, from the phase velocity, we determine the value of the effective refractive index of the waveguide mode $n_{w0} = 2.06$. This value is consistent with the nearly free photon picture where the effective refractive index of the guided mode n_w is limited by the refractive index of the surrounding medium $n_{gel} = 1.4$ on one side and the effective refractive index of the slab waveguide $n_{slab} \sim 3$ on the other side.

We will now discuss the quality factors of the coupled modes and the coupling to the external radiation. Only one of the $(-1,\pm1)$ modes couples to p-polarized light, while the two other modes couple to s-polarized light. The reciprocal lattice vector $(0,2)$ couples the two degenerate $(-1,\pm1)$ waves with electric fields $\mathbf{E_1}$ and $\mathbf{E_2}$ ($|\mathbf{E_1}| = |\mathbf{E_2}|$), and creates two non-degenerate modes $\mathbf{E_1} \pm \mathbf{E_2}$. The resulting mode denoted by the "+" sign has an electric field distribution which is even with respect to the mirror plane through the holes, and therefore couples to p-polarized radiation. The mode denoted by the "-" sign has an odd field distribution with respect to the same mirror plane and couples to s-polarized light. The standing wave component of the
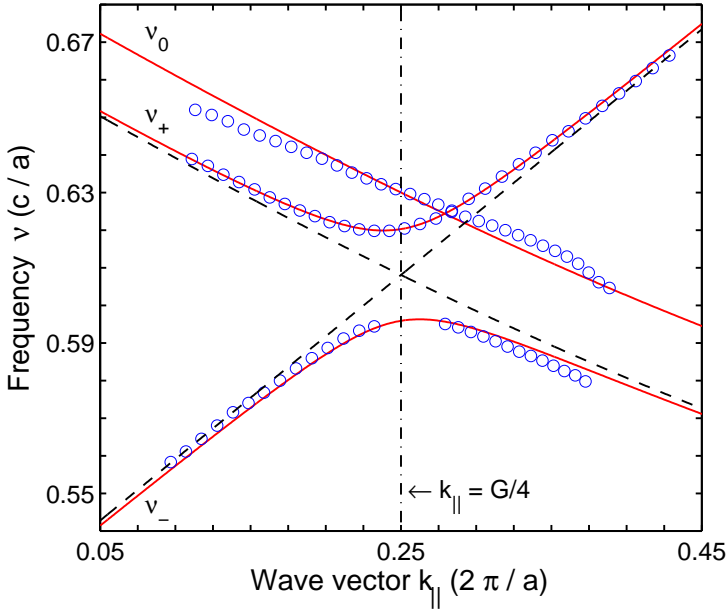
Figure 4.7. Dispersion relations for the *s*-polarized $(1,0)$ mode and both the *s*- and *p*-polarized $(-1,\pm1)$ modes derived from the fits of Fig. 4.6 (circles). The solid lines are obtained from a coupled mode theory with only 3 modes (see text). Note that the labels ν_0, ν_+, and ν_- correspond to the *p*-polarized $(-1,\pm1)$ mode, the *s*-polarized $(-1,\pm1)$ mode, and the *s*-polarized $(1,0)$ mode, respectively. The dashed lines indicate the unperturbed modes and cross at $k_{||} = G/4$.

pattern concentrates the electric field in the holes for the *p*-polarized $(-1,\pm1)$ mode, and in the dielectric medium for the *s*-polarized mode. As a result, the *p*-polarized mode is higher in frequency than the *s*-polarized mode [68].

The reciprocal lattice vector $(2,1)$ couples the $(1,0)$ wave with the two $(-1,\pm1)$ waves. The two modes show an avoided crossing where one of the modes becomes long-lived (subradiant) and disappears from the spectra, while the other one becomes short-lived (superradiant) and remains visible in the spectra [83–85]. This is a feature of the external coupling that can occur in open systems where the modes are coupled via a continuum [86, 87]. The radiation of one mode into the surroundings is suppressed by destructive interference, and as a result the quality factor of this mode is considerably increased. Meanwhile, the radiation of the other mode into the continuum is increased via constructive interference and the corresponding quality factor is decreased.

Figure 4.8 shows the quality factor (Q) for the *s*-polarized (1,0) mode as a function of the wave vector $k_{||}$ oriented along the ΓX symmetry direction (blue circles), as obtained by fitting a Fano model to the experimental transmission spectra. The error bars represent 95% confidence intervals determined from the fit. The dashed red line is a prediction of the quality factor and is given by

$$\frac{1}{Q} = \frac{1}{Q_{ideal}} + \frac{1}{Q_{loss}}.$$

(4.9)

Here Q_{ideal} is the calculated quality factor of the *s*-polarized (1,0) leaky mode for an ideal two-dimensional photonic crystal slab with parameters identical to the experimental structure. In experimental structures this quality factor is never reached due to absorption, imperfections and/or finite size effects. The effect of these loss mechanisms is characterized with the quality factor Q_{loss}.
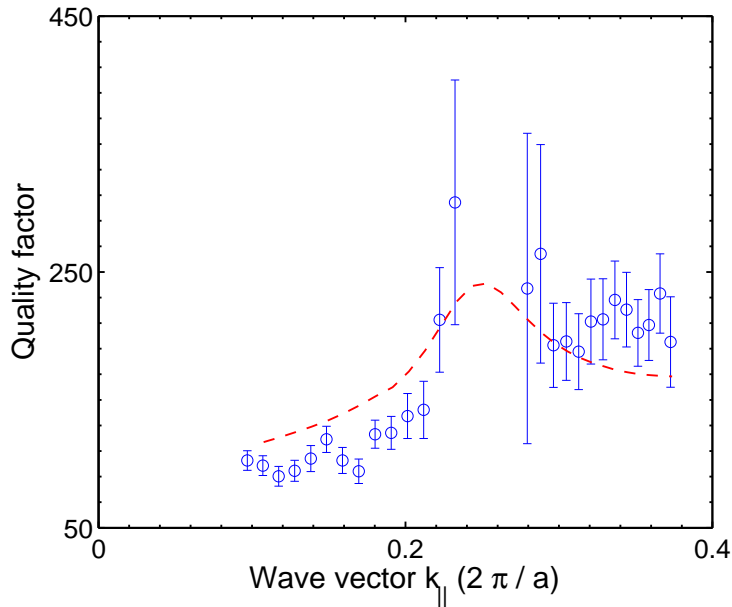

Figure 4.8. Experimental quality (Q) factor (blue circles) of the (1,0) mode as a function of the wave vector $k_{||}$, obtained by fitting the Fano model to the measured transmission spectra. Error bars represent 95% confidence intervals determined from the fit. The calculated quality factor for an ideal two-dimensional photonic crystal slab is used to obtain the dashed red line which serves as a guide to the eye (see text). Quality factors as high as 300 are measured, a value limited by the finite size of the structure.

We did not attempt to accurately describe the losses in the experimental structure, and used a constant value of 250 for Q_{loss}, independent of $k_{||}$. Since the field distribution in the slab depends on the mode and $k_{||}$, it is more realistic to consider Q_{loss} as a function of $k_{||}$. In fact, the data points for $k_{||} < G/4$ ((1,0) mode) are described better with $Q_{loss} = 175$, while the data points for $k_{||} > G/4$ are described better with $Q_{loss} = 325$.

As can be seen in the figure, the quality factor increases as the wave vector $k_{||}$ approaches midway between the Γ and the X point, where the avoided crossing occurs. At the avoided crossing, the (1,0) mode disappears and the corresponding quality factor diverges. The highest measured quality factor in our case is 300. For this case, the light travels a distance of $Q\lambda_0/n_{eff} \approx 200$ μm before diffracting into the surrounding media. Here $\lambda_0 = 1.38$ μm and $n_{eff} = 2.06$ are the resonant wavelength and the effective refractive index of the leaky mode, respectively. Since our sample covers an area of $\sim 300 \times 300$ μm^2, this suggests that the quality factor is limited by the finite size of the sample, and not by the optical quality of the structure.

4.5 Conclusions

We have demonstrated a novel method to transfer large freestanding photonic crystal slabs $\sim 300 \times 300$ μm^2 to a transparent substrate (gel) with a low refractive index of $n_{gel} = 1.4$. This eliminates the buckling of the membranes due to a lattice mismatch between the $Al_{0.35}Ga_{0.65}As$ membrane and the GaAs substrate. As a result, almost perfectly flat membranes which allow for both the reflection and transmission measurements, are created. After the transfer to the gel, the measured resonant frequencies of the leaky modes are red shifted with respect to those of a freestanding slab. This can be explained by the change in the effective refractive index of the leaky modes via a change in dielectric environment. More importantly, the resonant features in the experimental reflection spectra for photonic crystal slabs on the gel substrate are more prominent than those for freestanding photonic crystal slabs. We believe that this is due to the removal of the Fabry-Perot cavity that is formed by the highly-reflective GaAs substrate and the wavy membrane. Therefore, the structures on the gel are more attractive for studying the resonant effects in photonic crystal slabs.

We show that the interaction between the *s*-polarized (1,0) and (-1,$\pm$1) mode leads to an avoided crossing for the in-plane wave vector $k_{||}$ midway between the Γ and the X point of the square lattice. This avoided crossing can be described by a coupled mode theory featuring a 3×3 matrix instead of

a complete photonic band structure calculation. At the avoided crossing the lower energy *s*-polarized (1,0) mode disappears from the transmission spectra becoming a subradiant mode with a high quality factor. For this mode, we measure Q factors as high as 300 and show that these values are probably limited by the finite size of our structures (diffraction) demonstrating the excellent optical quality of the transferred membranes.

The high quality factor of leaky modes, makes our structures especially attractive for experimental study of nonlinear resonant effects, such as second harmonic generation [47–49]. Coupling to a resonance with a high Q factor accumulates considerable field intensity in the nonlinear material of a photonic crystal. If both the fundamental and the second harmonic waves couple resonantly to the structure phase-matching conditions are fulfilled [47,48], and large enhancement in the second harmonic response can be achieved.

The presented transfer technique may prove to be a robust and relatively simple way to integrate a wide variety of devices based on different materials. The transfer technique can be applied to increase extraction efficiency of light-emitting diodes by using diffraction from a photonic crystal layer [74]. Positioning a gallium phosphide membrane with a cavity on a flat diamond substrate with nitrogen-vacancy centers to achieve long coherence times [75,77,78] could probably also be done with our method. Finally, it should be possible to create a versatile lab-on-chip system by picking up a high Q photonic crystal nanocavity with the gel layer, and placing it on top of a network of microfluidic channels for biochemical sensing applications. Both the photonic crystal cavity and the microfluidic channels can be fabricated independently using desired materials and technologies. This kind of freedom, intrinsic to our method, could prove to be a very useful tool for integration of photonic crystal devices in a single chip.

70

Chapter 5

Interpretation of Fano lineshape reversal in the reflectivity spectra of photonic crystal slabs

5.1 Introduction

Asymmetric Fano lineshapes [66, 88] are a characteristic feature of (quantum) interference between two interfering paths and have been identified in many physical systems. These systems include, but are not limited to, neutron scattering [89], conductance of quantum dots [90, 91], optical transmission through metal hole arrays [85, 92], scattering spectra of microwave cavities [93] and photonic crystal structures [58, 59, 94]. Recently, it has been suggested that the details of the Fano lineshape, in particular a complex valued q parameter, contains information on the decoherence and dephasing of the underlying quantum system [93, 95]. Similarly, reversal of the Fano lineshape asymmetry has been linked to the ability to tune the interaction, and thus also the coherence, between the two channels [90, 96].

Photonic crystal slabs, i.e., dielectric slabs perforated with a regular lattice of holes, show distinct Fano resonances in their reflection and transmission spectra. These photonic crystal slabs support optical modes for a combination of frequency ω and in-plane wave vector $k_{||}$, which are above the light line defined by $\omega = ck_{||}$, with c the speed of light in vacuum. These modes are either propagating (Fabry-Perot) modes of the slab, or leaky modes that couple incident light from the surrounding media to a guided mode of the slab via

diffraction, picking up an additional crystal momentum equal to a reciprocal lattice vector. The interference of this resonant mode with the propagating Fabry-Perot mode leads to Fano resonances [57]. Typically, these resonant features in reflection spectra are used to find the dispersion relation of the leaky modes [58, 59, 94].

In most experimental studies the asymmetry parameter of the dispersive lineshape is considered to be constant and is regarded as a fit parameter. This asymmetry parameter, often denoted as q, can be interpreted as the amplitude of the resonant contribution relative to the background. The sign of q controls the asymmetry of the lineshape [66, 97]. In this picture, the asymmetry can only be reversed when the direct reflectivity reaches zero for which the lineshape becomes Lorentzian. The interference leading to the Fano lineshape in the reflectivity spectra of photonic crystal slabs can be tuned either via tuning the parameters of the structure, or via tuning the angle of incidence. Calculations at normal incidence for symmetric photonic crystal structures [98] confirm that this situation can be realized by tuning the ratio d/a of slab thickness over lattice constant. This shifts the resonance frequency of a leaky mode over a zero in the direct reflection of the slab and reverses the asymmetry. Experimentally this reversal has recently been demonstrated in reflection spectra of p-polarized light from a photonic crystal waveguide via angle tuning [67, 99]. When the angle of incidence is tuned through Brewster's angle, the amplitude of the direct reflection reaches zero and the asymmetry is reversed. The symmetry of the system ensures that the reflectivity reaches a true zero and the amplitude reflection coefficient for the electric field changes sign, corresponding to a π phase shift. It is this phase shift that is responsible for the reversal of the asymmetry.

In this chapter we show that experimental reflectivity spectra for an asymmetric slab structure also show Fano lineshapes that reverse their asymmetry. This is surprising as these asymmetric structures generally do not give a true zero in the amplitude reflection coefficient; the interference leading to zeros in the reflectivity (Fabry-Perot modes) is not complete and the asymmetric structure does not have a Brewster's angle where the reflectivity for p-polarized light goes through zero. In order to describe the reversal of the asymmetry a complex q parameter is needed in a system that obeys both time reversal symmetry and energy conservation. We stress that the origin of the complex q in our work is not due to dephasing or decoherence as reported in literature [93, 95], but due to the asymmetry of the system. While dephasing and decoherence always result in a complex q parameter, the inverse statement is not true.

5.2   Experiment

Photonic crystal slabs with a square lattice of holes with a hole radius of ~ 150 nm and a lattice constant $a = 820$ nm were fabricated in a commercially grown AlGaAs layer structure [51] using a combination of e-beam lithography and reactive ion etching techniques. The samples were fabricated using the facilities of the Kavli Nanolab Delft. The layers of the AlGaAs layer structure are deposited on a $\langle 100 \rangle$ GaAs substrate and consist of a 1 μm thick Al rich $Al_{0.7}Ga_{0.3}As$ layer, a 150 nm thick Ga rich $Al_{0.35}Ga_{0.65}As$ layer, and a 100 nm thick GaAs capping layer. To create the hole pattern, a 150 nm silicon nitride layer is deposited on top of the structure and serves as a mask during the final reactive ion etching step. The lattice of holes is created by e-beam lithography in a ~ 500 nm thick layer of positive tone e-beam resist, ZEP 520A [52], and transferred into the nitride mask layer using a low pressure reactive ion etching step in a CHF_3/Ar plasma. After removal of the e-beam resist in a low pressure O_2 plasma, the hole pattern is etched deep into the AlGaAs heterostructure in a $BCl_2/Cl_2/N_2$ reactive ion etch process at 100 W RF power, a pressure of ~ 4.5 μbar, and flow rates of 15, 7.5, and 10 sccm respectively. The nitrogen flow in this process was optimized to create near vertical side walls of the holes. After etching the holes, the nitride mask is removed using the CHF_3/Ar etching procedure described above.

To create a freestanding membrane the residual oxide layer is first removed by dipping the sample in 15:1 deionized H_2O:buffered hydrofluoric acid (BHF) solution for 15 sec. The sample is then placed in a 3:1 citric acid:H_2O_2 solution for 120 sec to selectively remove the GaAs capping layer. The freestanding membrane is created by etching the sacrificial $Al_{0.7}Ga_{0.3}As$ layer in a concentrated 1:4 HF (40%):H_2O solution for 60 sec followed by a rinsing step in pure water and critical point drying. The resulting freestanding membrane covers an area of $\sim 300 \times 300$ μm^2 and is used to measure specular reflectivity spectra at oblique angles of incidence. Afterwards, the membrane is transferred to a transparent gel layer [80], with a refractive index of 1.4 on a standard microscope slide to create a membrane without the highly reflective GaAs substrate and the reflectivity measurement is repeated.

The specular reflectivity measurements are done for wavelengths between 900 and 1700 nm using white light from a lamp coupled to a 50 μm multimode fiber. The output of this fiber is imaged onto the sample with a 1.5 times magnification to create a 75 μm spot on the sample. The reflected light is collected into a 400 μm fiber and then sent to a fiber-coupled grating spectrometer with an InGaAs array (Ocean Optics NIR512) with a ≈ 3 nm spectral resolution. Apertures in the beam limit the numerical aperture of the

input beam to NA ~ 0.025. A Glan-Thompson polarizing beamsplitter cube is placed in a parallel part of the beam and is used to measure both the *s*- and *p*-polarized reflectivity as a function of wavelength and angle of incidence.

5.3 Results

The experimentally measured reflection spectra for the symmetric slab structure are shown in Fig. 5.1. The figure shows the measurements (symbols) and calculations based on a complete scattering matrix method (solid gray lines), for angles of incidence of 60° (left), 70° (middle), and 80° (right). The frequency ω and the wave vector $k_{||}$ are plotted in dimensionless units $\omega a/(2\pi c)$ and $k_{||}a/(2\pi)$, respectively. The incident beam is *p*-polarized with the parallel wave vector $\mathbf{k}_{||}$ oriented along the ΓX symmetry direction of the photonic lattice. The numerical calculations assume an ideal two-dimensional photonic crystal slab with air on both sides. The calculations use the tabulated
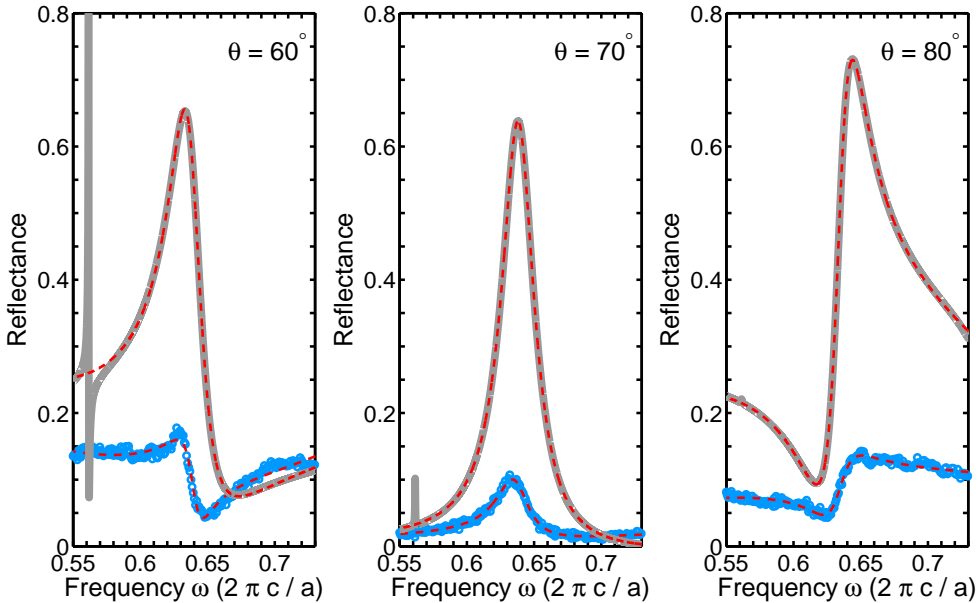

Figure 5.1. Measured (blue symbols) and calculated (solid gray lines) reflection spectra for different angles of incidence for a symmetric (freestanding) slab, showing the asymmetry reversal of the *p*-polarized (-1,±1) mode at Brewster's angle. The dashed red lines are fits to the data using the Fano model described in the text.

value for the refractive index of the $Al_{0.35}Ga_{0.65}As$ at a wavelength of 1.5 μm; $n_2 = 3.1975$ [62]. The thickness of the slab and the value of r/a are identical to those of the experimental structure. The calculations are performed for a structure with a lattice constant $a = 820$ nm, a radius of holes $r = 160$ nm, and a thickness of the slab $d = 122$ nm.

As can be seen in the figure, the calculations give good qualitative agreement with the data. Both the measured and the calculated reflectivity spectra are well described by the Fano lineshape. The dashed red lines in Fig. 5.1 show a fit using a Fano model, with the reflectivity $R(\omega)$ given by

$$R(\omega) = \left| r_D \exp(-i\Delta\xi) + \frac{r_R\Gamma_0}{i(\omega - \omega_0) + \Gamma_0} \right|^2. \tag{5.1}$$

The first term represents the direct contribution with an amplitude r_D, while the second term represents the resonant contribution with an amplitude r_R. The resonance is characterized by a frequency ω_0, and a linewidth Γ_0. The phase $\Delta\xi$ represents the phase difference between the resonant and the non-resonant contribution at the resonance frequency and controls the asymmetry of the resonance. We assume that the amplitude of the slowly varying non-resonant contribution as a function of frequency ω, $r_D(\omega)$, can be approximated well with

$$r_D(\omega) = \left| r_0 + r_1\omega + r_2\omega^2 \right|, \tag{5.2}$$

where r_0, r_1 and r_2 are fit parameters.

The asymmetry of the Fano lineshape in Fig. 5.1 of the p-polarized (-1,$\pm$1) mode is reversed by tuning the angle of incidence, creating a nearly symmetric lineshape at an angle of incidence of 70°. Based on the asymmetry of the lineshape in reflectivity measurements for every 5° (not shown) we estimate that the asymmetry reversal occurs at an angle of incidence of 71 ± 1°. This corresponds to a Brewster's angle θ_B for a uniform dielectric slab in air with an effective refractive index of $\tan(\theta_B)$ equal to $n_{\text{eff}} = 2.9 \pm 0.2$. We expect this value to be comparable to the effective refractive index estimated from the direct (non-resonant) reflectivity of the slab at the resonance frequency. This contribution is modeled by the Fresnel reflection coefficients of the dielectric slab with an effective refractive index that represents the average effect of the holes. Since this background is close to zero for all frequencies for angles of incidence close to Brewster's angle we analyze calculated spectra over a broad frequency range for angles of incidence of 60° and 80°. From these fits, we obtain values of the effective refractive index of 3.02 and 2.89, consistent with the effective refractive index found from analyzing the asymmetry of the resonant contribution.

Table 5.1 summarizes the resonance frequency, the linewidth and the phase difference, as obtained from the Fano model for both the measured and calculated reflection spectra in Fig. 5.1. The table shows the excellent agreement between the measured and calculated spectra for the resonance frequency (ω_0) and the corresponding linewidth (Γ_0). The phase difference $\Delta\xi$ changes sign as the resonant Fano lineshape changes the asymmetry. The relatively large error bars for $\Delta\xi$ are representative for the variation in the fitted value of $\Delta\xi$ for different choices of the background (direct) contribution; e.g., by setting both r_1 and r_2 equal to zero in Eq. 5.2. Close to Brewster's angle for the symmetric slab, the background (direct) contribution reaches zero amplitude and the phase difference $\Delta\xi$ becomes undefined. The comparison between the experimental and calculated spectra presented above confirms the picture that the asymmetry reversal occurs around the true zero in the direct reflectivity at Brewster's angle.

After reflection measurements, the symmetric, freestanding, photonic crystal membrane was transferred to a transparent gel substrate by sticking the membrane to the gel and peeling of the GaAs substrate, as described in Chapter 4 of this thesis. The gel is optically transparent and has a refractive index $n_{gel} = 1.4$. Figure 5.2 shows measured (symbols) and calculated (solid gray lines) reflection spectra for an asymmetric slab for angles of incidence of 75° (left), 78° (middle), and 83° (right).

The experimental data in the figure clearly show that the asymmetry reversal of the Fano lineshape of the p-polarized (-1,±1) mode also occurs in the asymmetric case when there is no Brewster's angle. In this case, the asymmetry reversal is observed at a significantly larger angle of incidence of $78 \pm 1°$, compared to the symmetric structure. The parameters of the fitted Fano lineshapes are summarized in Table 5.1.

5.4 Discussion

A detailed inspection of the calculated spectra for the asymmetric structure (not shown) reveals that the amplitude of the direct reflectivity is low, but does not reach zero. This implies that a simple change of the sign of the amplitude reflection coefficient in the direct channel cannot be responsible for the reversal of the Fano lineshape. In order to convincingly show that a true zero in the direct reflectivity is not a necessary condition for the asymmetry reversal of a Fano lineshape we performed additional calculations on a structure with a much larger lattice constant. The parameters of this structure are tuned to give a minimum in the direct reflectivity that is very different from zero.

Table 5.1. Fitted values of the Fano resonances: the center frequency, the linewidth, and the phase difference between the resonant and the direct contribution in the reflectivity. Results are given for both measured and calculated spectra, for various angles of incidence for a symmetric slab (top) and an asymmetric slab on a substrate (bottom).

	angle ($°$)	ω_0 ($2\pi c/a$)	Γ_0 ($2\pi c/a$)	$\Delta\xi$ (rad)
Symmetric				
	60	0.640 ± 0.005	0.009 ± 0.001	-2.19 ± 0.10
Experiment	70	0.636 ± 0.005	0.015 ± 0.002	-0.58 ± 0.15
	80	0.635 ± 0.005	0.015 ± 0.002	1.90 ± 0.08
	60	0.639 ± 0.001	0.014 ± 0.001	-1.28 ± 0.02
Calculation	70	0.638 ± 0.001	0.014 ± 0.001	—
	80	0.635 ± 0.001	0.012 ± 0.001	1.68 ± 0.07
Asymmetric				
	75	0.611 ± 0.005	0.009 ± 0.001	-0.60 ± 0.06
Experiment	78	0.611 ± 0.005	0.009 ± 0.001	-0.13 ± 0.15
	83	0.610 ± 0.005	0.008 ± 0.001	0.51 ± 0.24
	75	0.620 ± 0.001	0.014 ± 0.001	-0.72 ± 0.24
Calculation	78	0.620 ± 0.001	0.014 ± 0.001	-0.06 ± 0.37
	83	0.618 ± 0.001	0.015 ± 0.001	1.26 ± 0.05

The calculations are performed for both a symmetric (air-slab-air) and an asymmetric (air-slab-gel) structure and are summarized in section 5.4.3.

The remainder of this chapter is structured as follows: we will first introduce a general scattering matrix formalism for asymmetric structures and apply this to the specific case of a photonic crystal slab on a substrate with only two inputs and two outputs. This results in analytical expressions for the reflected amplitude and the asymmetry parameter q of the Fano resonance. We then apply this truncated scattering matrix method to interpret our experimental data and compare the results to those obtained using a complete scattering matrix.
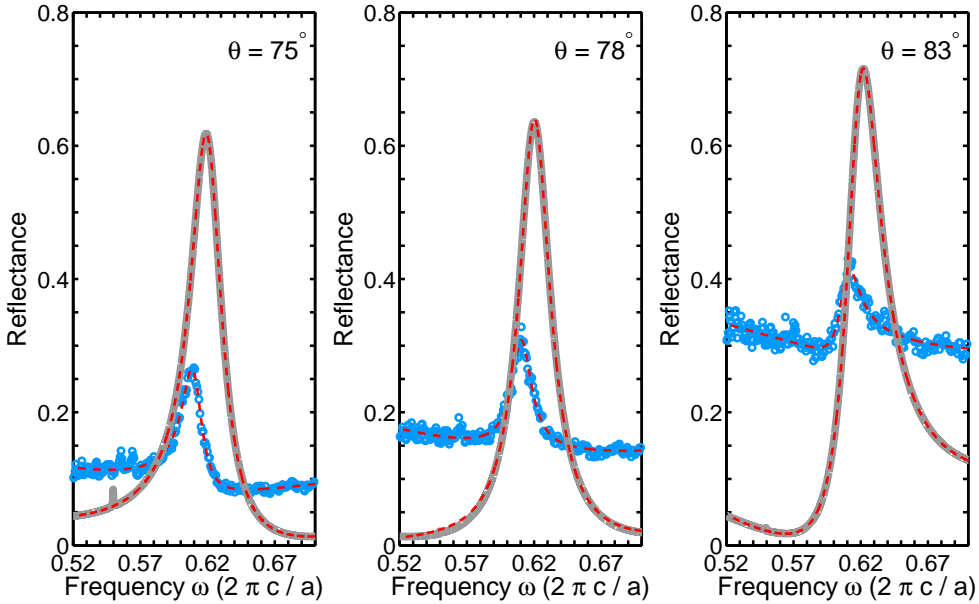
Figure 5.2. Measured (blue symbols) and calculated (solid gray lines) reflection spectra for different angles of incidence for an asymmetric (on gel) slab, showing the asymmetry flip of the *p*-polarized (-1,±1) mode. The dashed red lines are fits to the data using the Fano model described in the text.

5.4.1   Scattering matrix formalism

We introduce a scattering matrix formalism to describe the resonant coupling of incident radiation to a planar photonic crystal slab. Compared to earlier work [60], which deals with symmetric structures, our formalism deals with both symmetric and asymmetric photonic crystal waveguide structures. We will apply this formalism to the particular case of a planar photonic crystal slab on a substrate to gain physical insight in the origin of the asymmetry reversal of the dispersive (Fano) lineshape. We will give results for oblique angles of incidence for both symmetric (air-slab-air) and asymmetric (air-slab-gel) structures, and discuss the conditions for asymmetry reversal of the dispersive (Fano) lineshape in detail.

We consider an optical system with m inputs and m outputs that can be described by temporal coupled-mode theory featuring a $m \times m$ scattering matrix [60]. For the specific case of a photonic crystal slab the inputs and outputs of the system are defined by a plane wave incident on the slab that

is either transmitted, reflected or diffracted. The plane waves can couple to a guided mode in the photonic crystal membrane, thereby transforming the guided modes into leaky modes. This occurs whenever a photonic band in the band structure of a photonic crystal slab is above the light line. The resulting transmission and reflection spectra of a photonic crystal membrane contains several peaks, each with a dispersive (Fano) lineshape characteristic for the resonant coupling [58, 59, 94].

The input of the optical system is described by a column vector $\mathbf{b}_+$ that contains the amplitudes of the modes at the input. A similar vector $\mathbf{b}_-$ contains the amplitudes of the modes at the output. For a planar multilayer structure the amplitudes b_i in a medium with refractive index n_i are related to the E-field in the i-th layer by [100]

$$b_{\pm,i} = \sqrt{\frac{1}{2} \frac{k_{iz}}{k_0}} E_{\pm,i}, \tag{5.3}$$

where $k_0 = 2\pi/\lambda$ is the wave number and k_{iz} is the component of the wave vector perpendicular to the interface: $k_{iz} = n_i \cos\theta_i k_0$. To avoid confusion with the $\mathbf{E}$-field, we will refer to these amplitudes as $\mathbf{b}$-field amplitudes. This $\mathbf{b}$-field amplitude is normalized in such a way that the square of the amplitude relates directly to the power flux, defined by the Poynting vector, in the z-direction normal to the interface. The scattering matrix S relates the amplitudes of input and output modes via

$$\mathbf{b}_- = S\mathbf{b}_+.$$

For a lossless system that does not break time-reversal symmetry the scattering matrix S needs to be unitary and symmetric [60]:

$$SS^\dagger = I, \quad S_{ij} = S_{ji}.$$

To describe the coupling to leaky modes we will characterize each mode at a specific in-plane wave vector $k_\parallel$ by a center frequency ω_p and a linewidth Γ_p. The linewidth Γ_p is related to the coupling strength between the incoming light and the leaky mode. The total scattering matrix of a layered structure with N independent resonances can be written as

$$S = C + \sum_{p=1}^{N} \frac{\mathbf{d_p} \otimes \mathbf{d_p}}{i(\omega - \omega_p) + \Gamma_p}. \tag{5.4}$$

Here $\mathbf{d_p}$ is a vector containing the coupling constants of each mode to the resonator, ω_p are the resonance frequencies, Γ_p denotes the resonance linewidth,

and C is a unitary and symmetric scattering matrix. Linear optical structures impose both time-reversal symmetry and energy conservation constraints on the system and require that the matrix elements of C, Γ_p, and the coupling constants $\mathbf{d_p}$ are not independent [60].

5.4.2   Example: 2-port asymmetric slab

For a system with 2 inputs and 2 outputs the relation between C, Γ, and $\mathbf{d}$ can be made explicit and insight can be gained by studying this case in more detail. Therefore, we will restrict ourselves to the simplest asymmetric photonic crystal structures where no higher order diffraction occurs. In that case the system has only two inputs and two outputs and the scattering matrix reduces to a 2×2 matrix. The inputs and outputs of this system correspond to the reflected and transmitted modes. Compared to the earlier work reported in Ref. [60] we do retain the essential asymmetry induced by the substrate. The photonic crystal slab has an effective refractive index equal to n_2 and is sandwiched between a substrate with a refractive index n_3 and a superstrate with a refractive index n_1.

   The expressions for the asymmetric structure are identical to those of the symmetric structure if we refer to the amplitude reflection and transmission coefficients r' and t' of the $\mathbf{b}$-field as defined by Eq. 5.3. The complete scattering matrix is given by

$$
S = \begin{pmatrix} r' & t' \\ t' & r' \end{pmatrix} + \\
\frac{\Gamma_0}{i(\omega - \omega_0) + \Gamma_0} \begin{pmatrix} -(r' \pm t') & \mp(r' \pm t') \\ \mp(r' \pm t') & -(r' \pm t') \end{pmatrix},
\tag{5.5}
$$

where the $\pm$ sign corresponds to a situation where the E-field on both sides of the slab oscillates in phase or out of phase. For a symmetric slab this defines the modes as either *even* or *odd* relative to the symmetry plane in the middle of the slab [63]. The coefficients r' and t' are related to the more commonly used Fresnel coefficients r and t of the slab via $r' = r$ and $t' = t\sqrt{k_{3z}/k_{1z}}$ for both *s*- and *p*-polarized light [100].

   The reflected intensity of the slab given by $R(\omega) = |S_{11}(\omega)|^2$ can be written in a form that is identical to the original result of Fano [66]:

$$
R(\epsilon) = |S_{11}(\epsilon)|^2 = |r'|^2 \frac{|q + \epsilon|^2}{1 + \epsilon^2}.
\tag{5.6}
$$

Here ϵ is the normalized detuning in units of the linewidth $\epsilon = (\omega - \omega_0)/\Gamma_0$,

and the asymmetry parameter q is given by

$$q = \pm i \, \frac{t'}{r'}. \tag{5.7}$$

A similar expression can be derived for the transmission with an asymmetry parameter $\tilde{q} = -q^{-1}$. For a symmetric slab q reduces to a real-valued parameter since the Fresnel transmission coefficient has a π phase difference with the reflection coefficient. This is no longer true for the more general case of an asymmetric slab for which the phase difference between t' and r' varies as a function of angle of incidence and the resulting q parameter is complex.

For the calculation shows the calculated phase difference between the direct and the resonant contribution in the reflection of p-polarized light for the fundamental TE mode supported by a waveguide layer with an effective refractive index n_{eff} equal to 3.16 representative of the AlGaAs material used in the experiment.

For this calculation we used the matrix element S_{11} in Eq. 5.5 at the resonance frequency and we used complex Fresnel coefficients r and t defined as

$$r = \frac{r_{12} + r_{23} \exp[i2k_{2z}d]}{1 - r_{21}r_{23} \exp[i2k_{2z}d]} \exp[-i2k_{1z}d]$$

$$t = \frac{t_{23}t_{12} \exp[i(2k_{2z} - k_{1z} - k_{3z})d/2]}{1 - r_{21}r_{23} \exp[i2k_{2z}d]}.$$

Here the coefficients r_{ij} and t_{ij} refer to the Fresnel coefficients of a single interface between layer i and j. The figure shows the phase difference as a function of angle of incidence and dimensionless quantity $n_{\text{eff}}d/\lambda$. Figure 5.3 (a) shows the phase difference for a symmetric structure with air on both sides, while Fig. 5.3 (b) shows the phase difference for the same slab with the air on one side replaced by a transparent gel with refractive index $n_3 = 1.4$. This figure clearly shows large, abrupt jumps in the phase difference for both symmetric and asymmetric slab structures. The phase jumps in the symmetric case are easily understood as points where the direct reflectivity reaches zero. This occurs at Brewster's angle (vertical dashed line in (a)) and whenever the reflectivity becomes zero due to interference in the film (horizontal solid lines). This Fabry-Perot condition is satisfied whenever the optical path length of the film defined as $n_{\text{eff}}d\cos\theta$ is equal to $m\lambda/2$, with m integer. This situation changes for the asymmetric structure (b). The Fabry-Perot condition produces a minimum in the reflectivity, but the reflectivity does not reach zero. As can be seen in the figure, for angles smaller than $\arctan(n_3/n_1)$ the phase jumps at the minimum in the reflectivity. To understand the phase jump for larger
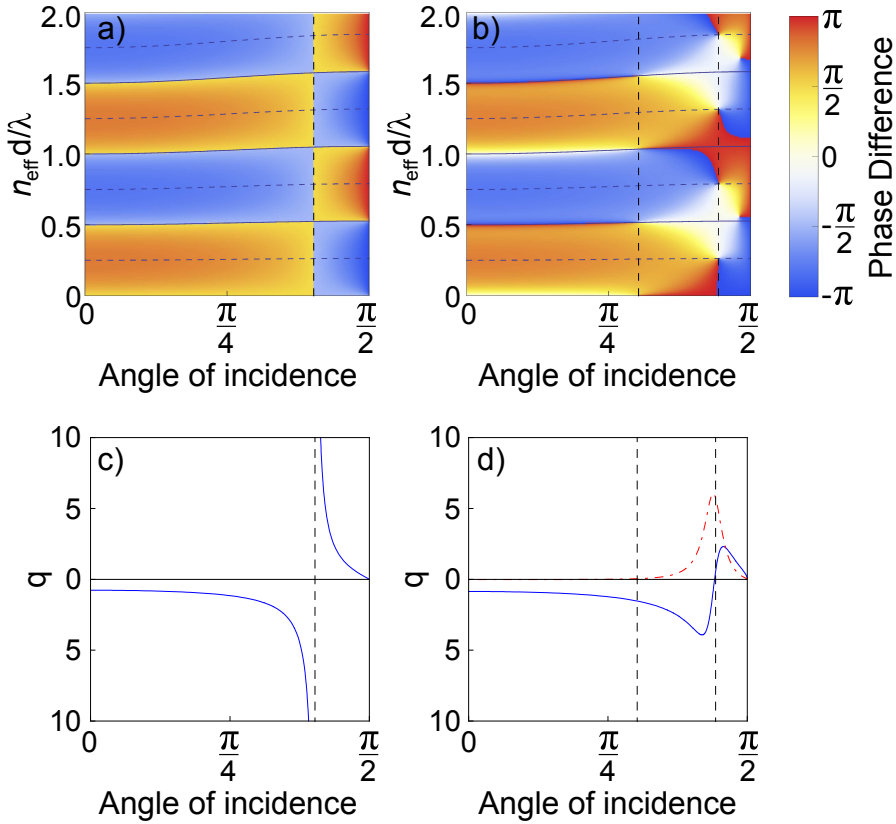
Figure 5.3. Calculated phase difference between the direct and the resonant contribution for a slab with an effective refractive index of 3.16, representative for AlGaAs used in the experiment. The plot shows the phase difference as a function of angle of incidence and dimensionless quantity $n_{\text{eff}}d/\lambda$ for a symmetric membrane structure (a) and an asymmetric structure on a gel substrate with $n_3 = 1.4$ (b). The solid and dashed lines are explained in the text. The corresponding asymmetry parameter q of the Fano resonance as a function of angle of incidence is shown for the symmetric (c) and asymmetric structure (d) for a value of $n_{eff}d/\lambda = 0.3$. The solid line refers to the real part of q, while the dash-dot line shows the imaginary part of q for the asymmetric structure.

angles of incidence we write the reflectivity of the asymmetric slab as [101]:

$$R = |r|^2 = \frac{r_{12}{}^2 + r_{23}{}^2 + 2r_{12}r_{23}\cos 2\beta}{1 + r_{12}{}^2 r_{23}{}^2 + 2r_{12}r_{23}\cos 2\beta},$$

with $\beta = k_{2z}d$.

From this expression it is clear that the minima and maxima in the reflectivity are found by the condition

$$\cos 2\beta = \pm 1.$$

These conditions are indicated by the solid and dashed horizontal lines in the figure. The reflectivity of the asymmetric slab can only become zero for a specific combination of frequency and angle of incidence. The frequency at which the reflectivity becomes zero is given by the above condition, while the angle is defined by the additional condition that

$$r_{12} = \pm r_{23}.$$

This leads to two angles, indicated by the dashed vertical lines in Fig. 5.3 (b). The smallest of the two angles is independent of the refractive index of the layer n_2 and is equal to Brewster's angle $\arctan(n_3/n_1)$ between the superstrate and substrate [101]. The second angle depends on the refractive index of the slab, superstrate, and substrate material. For a slab with $d/a < 0.5$ this angle is always larger than Brewster's angle between the superstrate and the slab material. From the figure, it can be seen that the phase difference jumps for angles close to this larger angle for dimensionless quantities $n_{\text{eff}}d/\lambda$ that are not close to $m/2$, with m being integer. The value of the refractive index of the substrate plays an important role in determining the two angles and also controls the apparent repulsion between the phase jumps due to the Fabry-Perot effect and due to angle tuning.

The angle from the simple truncated scattering matrix model is consistent with the experimental results presented in Section 5.3. For a structure with an effective refractive index of 2.9 ± 0.2 on a substrate with a refractive index of 1.4, the minimum in the direct reflectivity (see the vertical dashed line in Fig. 5.3) occurs at an angle of $78.1 \pm 1.5°$. This number compares well with the experimental value of $78 \pm 1°$. Figures 5.3 (c) and (d) show the calculated asymmetry parameter q as a function of angle for a value of $n_{eff}d/\lambda = 0.3$. This value corresponds to the experimentally measured frequency of the Fano resonance of the symmetric structure at Brewster's angle. The real part of q is represented by the solid blue line, while the complex part of q is shown by

the red dash-dot line. For the symmetric structure the q is real-valued, while the q parameter for the asymmetric structure in Fig. 5.3 (d) is clearly complex with a non-trivial phase that depends on the angle of incidence.

5.4.3 Asymmetry reversal with nonzero background

In this section we present numerical data calculated by a complete scattering matrix method that show that the asymmetry of a Fano resonance can be reversed if the direct reflectivity does not reach zero. The parameters of the photonic crystal structure in the calculation are tuned to give a minimum in direct reflectivity that is very different from zero to more clearly illustrate the point. We consider a two-dimensional photonic crystal slab with a lattice constant $a = 2$ μm and use the same radius of holes $r = 160$ nm and slab thickness $d = 122$ nm as in the experimental structure. The refractive index of the slab material is taken to be $n_{slab} = 3.157$, equal to the infrared refractive index of $Al_{0.35}Ga_{0.65}As$ at a wavelength of 2.5 μm [62].

Figures 5.4 and 5.5 summarize the calculated reflection spectra and corresponding phase difference $\Delta\xi$ for the symmetric structure. These data should be compared to the data in Figures 5.6 and 5.7 obtained for the asymmetric structure.

The calculated reflection spectra in Figure 5.4 show the Fano lineshape reversal for the symmetric structure. Spectra are shown for angles of incidence from $68°$ to $76°$ in steps of $2°$ (solid lines) and are offset vertically by 0.8 for clarity. The horizontal dash-dot lines indicate the zero reflectance for each angle of incidence. The dashed lines show the fitted Fano lineshapes to data. As can be seen, the asymmetry of the Fano lineshape is reversed by tuning the angle of incidence. At Brewster's angle ($\theta = 72°$), the direct reflectivity reaches zero, and the Fano lineshape reduces to the symmetric Lorentzian lineshape of the resonant contribution.

The solid line in Fig. 5.5 shows the phase difference $\Delta\xi$ between the resonant and the non-resonant contribution, for the p-polarized (-1,$\pm$1) mode over a large range of angles. This phase difference is obtained at the resonance frequency, by fitting the Fano model of Eq. 5.1 to the calculated reflection spectra. The phase difference $\Delta\xi$ influences the interference between the direct and resonant reflectivity and controls the asymmetry of the Fano lineshape. Whenever this phase difference is an integer multiple of π radians, the asymmetry reversal of the Fano lineshape occurs. As can be seen in Figure 5.5, the phase difference goes through zero for an angle of incidence of $72°$. This angle is exactly equal to Brewster's angle for the symmetric structure and the direct reflectivity is zero (see Fig. 5.4).
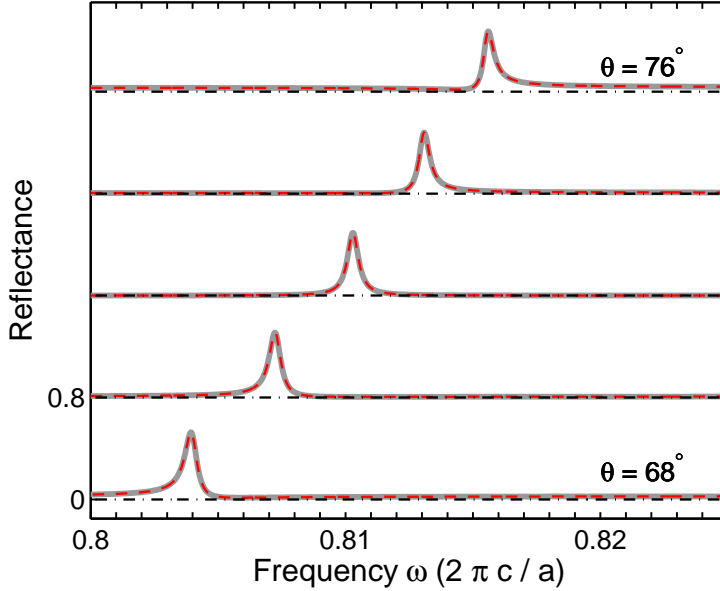
Figure 5.4. Calculated reflection spectra for a symmetric structure (solid lines), for angles of incidence from 68° to 76° in steps of 2°, vertically offset by 0.8 for clarity, showing the asymmetry reversal of the p-polarized (-1,±1) mode. The calculations are performed for a structure with a lattice constant $a = 2$ μm, a radius of holes $r = 160$ nm, and a slab thickness $d = 122$ nm. Note that the zero in the amplitude reflection coefficient is indicated by the dash-dot lines, for each reflectivity spectrum. The dashed lines show the fit of the Fano model to the calculated data.

Figure 5.5 shows a small, abrupt change, in the phase difference, for an angle of incidence of $\approx 12°$, as indicated by the vertical arrow. The origin of this phase change is an extra diffraction order of the leaky mode into the surrounding air. These diffraction orders occur whenever the length of the wave vector in air is larger or equal than the parallel component of the wave vector of the waveguide mode modulo a reciprocal lattice vector $\mathbf{G}$. In dimensionless units this diffraction condition is given by

$$|\mathbf{k_s}| = n_s\omega_0 > |\mathbf{k}_{||} + \mathbf{G}|, \tag{5.8}$$

where $\mathbf{k_s}$ is the wave vector in the substrate/superstrate and $\mathbf{k}_{||}$ is the parallel component of the incident wave vector, ω_0 is the dimensionless frequency of the resonance and n_s is the refractive index of the substrate/superstrate. The inset of Fig. 5.5 shows the dispersion $\omega_0(\theta)$ of the p-polarized (-1,±1) leaky
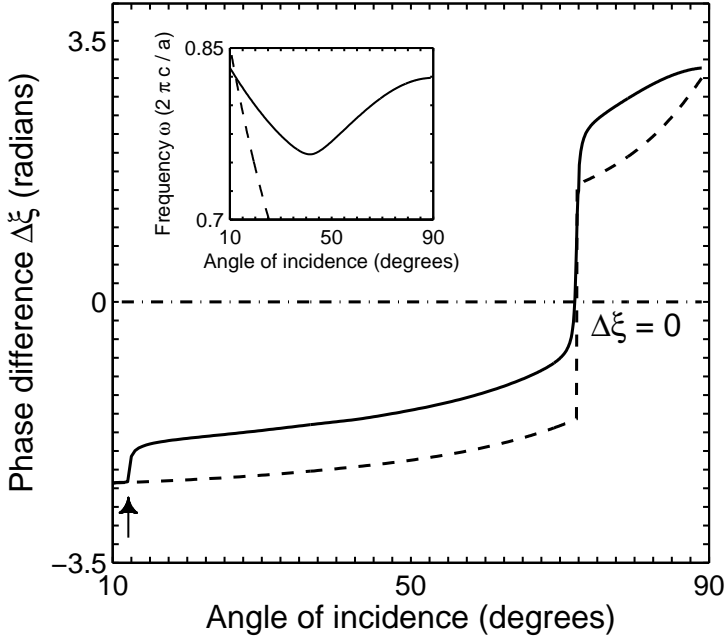
Figure 5.5. Calculated phase difference between the resonant and the non-resonant contribution, as a function of the angle of incidence, for a symmetric structure (solid line). The phase difference is obtained for the *p*-polarized (-1,±1) mode at the resonance frequency, by fitting a Fano model to the calculated reflection spectra. The asymmetry reversal of the Fano lineshape ($\Delta\xi = 0$) occurs at Brewster's angle. The dashed line represents the phase difference calculated using a coupled-mode theory with only two modes, as described in the text. The inset shows the calculated dispersion relation of the leaky mode (solid line), and the folded light line in air (dashed line).

mode (solid line) obtained from the calculated spectra together with the folded light line in air (dashed line)*. The crossing of these lines corresponds to the condition for diffraction in air, which occurs for angles larger than $12°$.

How does the phase difference between the resonant and the non-resonant contribution compare to the phase difference calculated with the relatively simple coupled-mode theory of only two modes as presented in Section 5.4.2? To answer this question, we ignore the effect of higher diffraction orders and

---

*To convert in-plane wave vectors $k_{||}$ to angles of incidence θ for a mode with a dispersion $\omega(k_{||})$ in a medium with a refractive index n, we use the expression $\theta = \arcsin(k_{||}/(n\omega))$, with ω and $k_{||}$ expressed in dimensionless units $\omega a/(2\pi c)$ and $k_{||}a/(2\pi)$, respectively.

use the truncated 2×2 matrix to describe the system. The direct reflectivity of our slab can be well described by the reflectivity of a uniform slab with a frequency dependent effective refractive index n_2, which takes into account the extra dispersion due to the presence of the holes [57]. We fitted the Fano model to the calculated p-polarized reflection spectrum for an angle of incidence of 10°. For this angle there are no diffraction orders in air for the relevant (-1,±1) mode. The calculated reflection spectrum consists of sharp resonant features going from zero to unity superimposed on a slowly oscillatory background. The direct reflectivity is well described by an effective refractive index

$$n_2 = 3.118 - 0.014\omega + 0.029\omega^2, \tag{5.9}$$

with ω expressed in dimensionless units $\omega a/(2\pi c)$. Since the p-polarized (-1,±1) mode shows a flat dispersion (see inset of Fig. 5.5), the resonance frequency does not change significantly with $k_{||}$. Therefore, we assume that Equation 5.9 can be used for other angles of incidence as well. The dashed line in Fig. 5.5 shows the calculated phase difference using Eq. 5.5 and the known dispersion of the resonant mode. As can be seen, the agreement between the solid and the dashed line is excellent for angles below 12°. For angles larger than 12° there is a small deviation as the truncated two-port system fails to describe the diffraction orders in air. Apparently, the influence of the diffraction orders on the phase difference at Brewster's angle is small, and the truncated scattering matrix accurately captures the physical process related to the reversal of the Fano lineshape.

To emphasize that in the asymmetric case the direct reflectivity does not reach zero while the asymmetry of the Fano lineshape is reversed, Figure 5.6 shows the calculated reflection spectra (solid lines), for angles of incidence from 72° to 80° in steps of 2°. The spectra are offset vertically by 0.2 for clarity, with the horizontal dash-dot lines indicating zero reflectance. It is clear from the figure that the asymmetry reversal occurs between 76° and 78°, but that the direct reflectivity does not reach zero for the entire angle range from 72° to 80°.

The corresponding phase difference $\Delta\xi$ between the direct and the resonant contribution is shown by the solid line in Fig. 5.7. The parameters of the structure are identical to those of the symmetric structure of Fig. 5.5, with the only difference that the air on one side has been replaced by a dielectric with a refractive index of 1.4. As can be seen, the phase difference goes through zero for an angle of incidence of 77.2°, which is larger than Brewster's angle for the symmetric structure. Similar to the symmetric structure we observe abrupt changes in the phase difference due to higher order diffraction in the
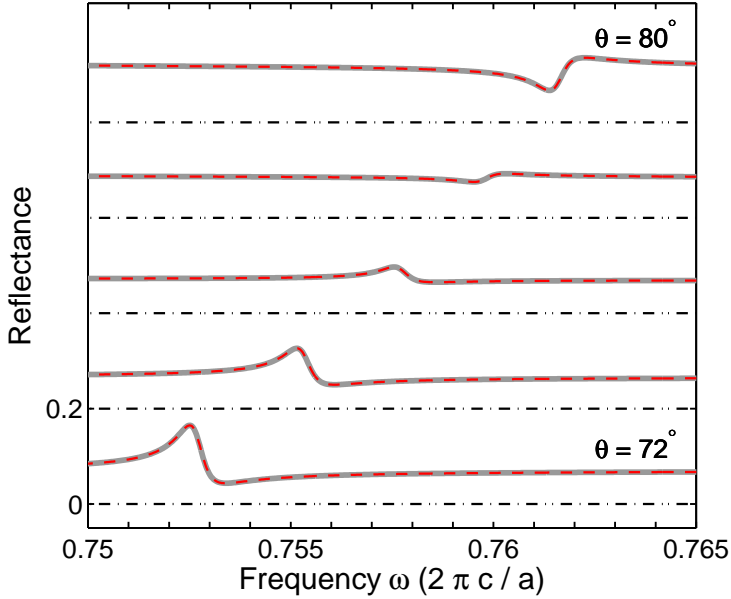
Figure 5.6. Calculated reflection spectra for an asymmetric structure (solid lines), for angles of incidence from 72° to 80° in steps of 2°, vertically offset by 0.2 for clarity, showing the asymmetry reversal of the *p*-polarized (-1,±1) mode. Note that the zero in the amplitude reflection coefficient is indicated by the dash-dot lines, for each reflectivity spectrum. Dashed lines show the fit of the Fano model to the calculated data.

air and in the substrate, as indicated by the vertical arrows. The inset shows the dispersion relation of the leaky mode (solid line) together with folded light lines in air (dashed line) and in the substrate (dash-dot lines). From the crossings of these lines with the dispersion of the leaky mode we conclude that there are four higher diffraction orders. The diffraction order into the substrate that uses the (-1,0) reciprocal lattice vector is present for all angles of incidence.

The dashed line in Figure 5.7 shows the calculated phase difference using coupled-mode theory of Section 5.4.2 truncated to only two modes. In the calculation we use the same effective refractive index for the slab as a function of frequency (Eq. 5.9) as obtained for the symmetric slab, since the increase in the effective refractive index caused by the gel substrate is small. As can be seen, the truncated coupled-mode theory reproduces the main features in the phase difference. We note a slight difference in the angle where the Fano
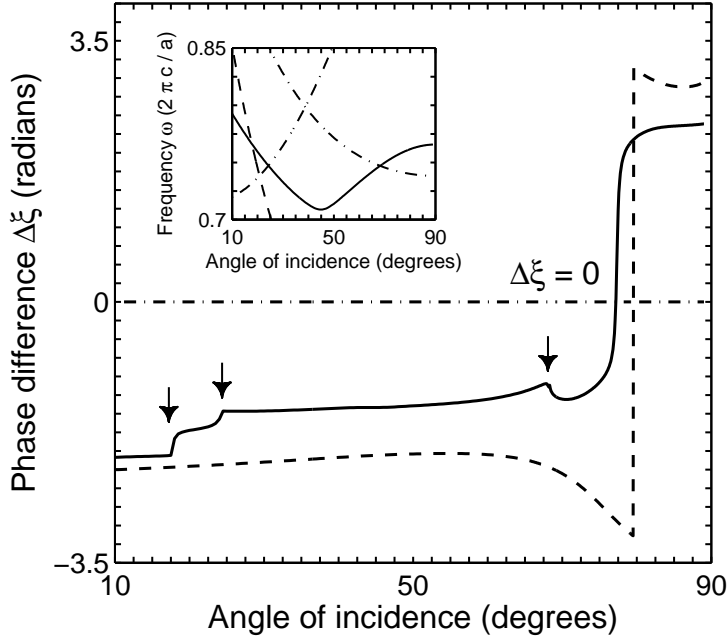
Figure 5.7. Calculated phase difference between the resonant and the non-resonant contribution, as a function of the angle of incidence, for an asymmetric structure (solid line). The phase difference is obtained for the *p*-polarized (-1,±1) mode at the resonance frequency, by fitting a Fano model to the calculated reflection spectra. The asymmetry reversal of the Fano lineshape ($\Delta\xi = 0$) occurs beyond Brewster's angle for the symmetric structure. The dashed line represents the phase difference calculated using a coupled-mode theory with only two modes, as described in the text. The inset shows the calculated dispersion relation of the leaky mode (solid line), and the folded light lines in both air (dashed line) and gel (dash-dot lines).

lineshape reversal occurs between the truncated model and the full calculation. This difference can be attributed to the presence of higher order diffraction. For a lossless system, the amplitude of the resonance should be equal to 1, when there is no higher order diffraction. Due to the higher order diffraction, the amplitude of the resonance in Fig. 5.6 is significantly reduced. Nevertheless, we believe that the truncated model accurately describes the physical process underlying the reversal of the Fano lineshape.

5.5   Conclusions

The measured reflectivity spectra for p-polarized light for a photonic crystal slab on a gel substrate, show several Fano lineshapes on top of a slowly varying background. The asymmetry of the Fano lineshape can be reversed by tuning the angle of incidence. For symmetric slabs, with air on both sides, the angle at which the asymmetry reverses is equal to Brewster's angle, and the direct contribution reaches zero. For asymmetric slabs this is no longer true: the reversal is observed for an angle of incidence beyond Brewster's angle, and the direct reflectivity no longer reaches zero. A truncated two-port coupled-mode theory can be applied to both the symmetric and the asymmetric structures, which reveals the underlying mechanism of the asymmetry reversal. For asymmetric photonic crystal slabs with $d/a < 0.5$, the reversal of the asymmetry occurs for angles larger then Brewster's angle. We show that the resonances in reflection spectra of a lossless photonic crystal waveguide should be described by a complex q parameter in the Fano model. Only for a symmetric structure the q parameter, which gives the ratio between the resonant and the direct contribution, can be taken as real. The reversal of the asymmetry occurs whenever the phase difference between the resonant and the non-resonant contribution is an integer multiple of π, which does not necessarily coincide with a minimum in the direct reflectivity.

CHAPTER 6

Second harmonic generation in transmission from photonic crystals on a gel substrate

6.1 Introduction

Increasing the efficiency of frequency conversion processes has always been an important goal of nonlinear optics. As long as phase-matching conditions are satisfied, a higher nonlinear conversion efficiency can be achieved by either focusing the light or by using a material with a larger nonlinear susceptibility [29]. The phase-matching condition ensures that all the waves generated in the material are in phase, and therefore add up constructively. For most nonlinear media this condition is not automatically satisfied due to material dispersion. Common ways to phase-match the nonlinear interaction are to use temperature tuning or angle tuning of a birefringent nonlinear crystal, e.g., BBO, KTP, or LiNbO₃. Unfortunately, this method cannot be applied to optically isotropic materials with a much larger nonlinear susceptibility. This is the case with some III-V semiconductor materials. For example, gallium arsenide (GaAs) has a more than 70 times larger effective second-order nonlinear susceptibility $\chi^{(2)}_{eff}$ than that of BBO but is not birefringent.

Bloembergen et al. [33] were the first to propose a structure with periodically alternating layers of low and high refractive index as a way to satisfy the phase-matching condition. For this structure, an existing phase mismatch can be compensated by adding or subtracting an appropriate reciprocal lattice vector $\mathbf{G}$ of the photonic lattice. This is called quasi-phase-matching. The nonlinear conversion efficiency can be further enhanced significantly by a strong spatial confinement of the optical fields which enhances the field inten-

sities. This has been demonstrated by Scalora et al. [46] for the case of second harmonic generation (SHG) from one-dimensional periodic GaAs/AlAs structures where the enhancement of the second harmonic (SH) signal is achieved by confining both the fundamental and second harmonic optical fields.

Cowan et al. [47] showed theoretically how to use leaky modes of a free-standing two-dimensional photonic crystal slab to achieve both quasi-phase-matching and strong spatial confinement. Leaky modes couple incident light from the surrounding media to a guided mode of the slab via diffraction from the photonic lattice. Using a Green's function formalism, the authors calculated an enhancement of SH signal in reflection of more than 6 orders of magnitude compared to the SH signal off-resonance. An experimental investigation by Mondia et al. [48] resulted in an enhancement of the second harmonic signal generated in reflection from a two-dimensional GaAs photonic crystal slab on an Al_2O_3 cladding layer. The SH signal was generated by focusing a tunable laser with short pulses (150 fs) to a 35 μm spot on the sample. By tuning the laser frequency and the angle of incidence authors investigated the enhancement of the SH signal. When both the fundamental and the second harmonic wave are resonant with the leaky modes of the structure, an enhancement of more than 1200 times compared to the noise floor was measured.

Torres et al. [49] present a theoretical and experimental study of the second harmonic signal generated in reflection from a one-dimensional GaN photonic crystal. They report an enhancement of more than 5000 times compared to an unpatterned GaN slab when both the fundamental and the second harmonic wave are resonant with the leaky modes of the structure. When only the fundamental beam is resonant with the structure, the enhancement is significantly reduced to a factor of 350.

In this chapter we study the influence of leaky modes on the second harmonic generation from a two-dimensional $Al_{0.35}Ga_{0.65}As$ photonic crystal slab on a transparent gel substrate. Compared to earlier experiments in literature [48, 49] a narrow linewidth pulsed laser at 1.535 μm is collimated rather than focused on the sample and the SH signal is measured in transmission instead in reflection. The resonant coupling of both the fundamental and SH wave to the leaky modes of the structure is probed by tuning the angle of incidence. In contrast to the work presented in References [48, 49] where the condition of double resonance was achieved at oblique angles of incidence, our structure is doubly resonant at normal incidence. At normal incidence, the second harmonic signal is enhanced by a factor 10000 relative to the non-resonant signal. The double resonance condition at normal incidence combined with the high enhancement of the SH signal in transmission holds promise for collinear

down-conversion [102, 103].

Compared to earlier experiments [48, 49], our experiments clearly show the effect of the resonant coupling of the second harmonic waves to leaky modes of the structure. By increasing the angle of incidence the fundamental beam is tuned away from resonance, resulting in a decrease of the second harmonic signal. However, at angles of incidence of $\pm\, 9.1°$ two local maxima are clearly observed in the experimental second harmonic signal.

We use a coupled mode theory [60, 100] to explain the main features of the measured second harmonic signal as a function of the angle of incidence. Within this theory, each of the leaky modes of the photonic crystal is treated as a resonance, and the SH signal in transmission depends on how efficiently the fields at the fundamental and the second harmonic frequency couple in or out of these resonances, and on the phase mismatch. Unlike numerical methods such as finite difference time domain calculations or a Green's function approach, our approach offers direct insight into the underlying physical mechanism. More importantly, our simple model uses parameters that are easily obtained by independent measurements of the linear as well as the nonlinear optical properties of the system instead of assuming parameters of an ideal two-dimensional photonic crystal slab. This makes the model immediately applicable to realistic experimental structures that have a finite size and very likely a number of fabrication imperfections. We show that the measured second harmonic signal cannot be explained by considering the resonant coupling at only the fundamental frequency, and that resonant effects at the second harmonic frequency have to be included.

6.2   Sample preparation

Photonic crystal slabs with a square lattice of holes with a hole radius of ~ 150 nm and a lattice constant $a = 820$ nm were fabricated in a commercially grown AlGaAs layer structure [51] using a combination of e-beam lithography and reactive ion etching techniques. The samples were fabricated using the facilities of the Kavli Nanolab Delft. The layers of the AlGaAs layer structure are deposited on a <100> GaAs substrate and consist of a 1 μm thick Al rich $Al_{0.7}Ga_{0.3}As$ layer, a 150 nm thick Ga rich $Al_{0.35}Ga_{0.65}As$ layer, and a 100 nm thick GaAs capping layer. The composition of the slab layer is chosen to render the structure optically transparent at both the fundamental (1535 ± 1 nm) and second harmonic wavelength (767.5 ± 0.5 nm). To create the hole pattern, a 150 nm silicon nitride layer is deposited on top of the structure and serves as a mask during the final reactive ion etching step. The lattice of holes is created

by e-beam lithography in a $\sim$ 500 nm thick layer of positive tone e-beam resist, ZEP 520A [52], and transferred into the nitride mask layer using a low pressure reactive ion etching step in a CHF_3/Ar plasma. After removal of the e-beam resist in a low pressure O_2 plasma, the hole pattern is etched deep into the AlGaAs heterostructure in a $BCl_2/Cl_2/N_2$ reactive ion etch process at 100 W RF power, a pressure of $\sim$ 4.5 μbar, and flow rates of 15, 7.5, and 10 sccm respectively. The nitrogen flow in this process was optimized to create near vertical side walls of the holes. After etching the holes, the nitride mask is removed using the CHF_3/Ar etching procedure described above.

To ensure a nonzero efficiency for second harmonic generation, the ΓX direction of the photonic lattice is deliberately rotated relative to the crystallographic <100> direction of the AlGaAs of the slab layer by an angle of $\sim$ 22.5°. Therefore, the incident electric field of the fundamental is never along a crystallographic axis of the AlGaAs and the effective nonlinearity is nonzero. Collinear second harmonic generation along one of the crystallographic directions is forbidden due to the 4$\bar{3}$m symmetry of the GaAs lattice [29].

To create a freestanding membrane the residual oxide layer is first removed by dipping the sample in 15:1 deionized H_2O:buffered hydrofluoric acid (BHF) solution for 15 sec. The sample is then placed in a 3:1 citric acid:H_2O_2 solution for 120 sec to selectively remove the GaAs capping layer. The freestanding membrane is created by etching the sacrificial $Al_{0.7}Ga_{0.3}As$ layer in a concentrated 1:4 HF (40%):H_2O solution for 60 sec followed by a rinsing step in pure water and critical point drying. The resulting freestanding membrane covers an area of $\sim$ 300$\times$300 μm^2. Finally, the membrane is transferred to a transparent gel layer [80] with a refractive index of 1.4 on a standard microscope slide, as described in Chapter 4 of this thesis. As a result, an almost perfectly flat membrane which allows for reflection as well as transmission measurements is created.

6.3 Experiment

Figure 6.1 shows the setup used for both second harmonic generation and linear transmission measurements. Alternating between the two experiments is done by flipping both mirrors (flip mirrors) either "down" for second harmonic generation or "up" for linear transmissivity measurements. The second harmonic is generated by a Q-switched Cobolt Tango laser which has a specified center wavelength of 1535 $\pm$ 1 nm, and a narrow linewidth < 0.04 nm. The laser produces pulses with a typical duration of $\approx$ 3.8 ns (full width at half maximum) at a repetition rate of 5 kHz. The generated signal at second har-
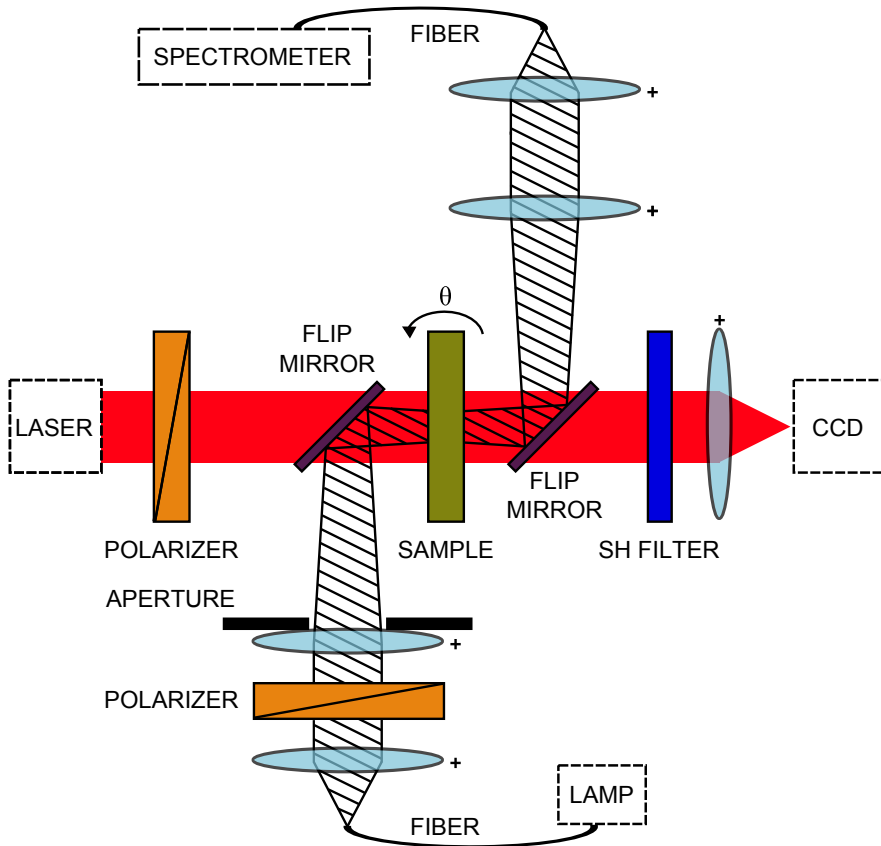
Figure 6.1. Setup used for second harmonic generation and linear transmission measurements. A fiber-coupled lamp and a spectrometer are used for linear transmission measurements, while a pulsed laser operating at 1.535 μm and a CCD camera equipped with a bandpass filter (SH filter) are used for second harmonic measurements. The polarization of the incident beam is set by a Glan-Thompson polarizing beamsplitter cube, and the angle of incidence θ is controlled by placing the sample on a motorized rotation stage. For linear transmission measurements an aperture in the beam limits the angular spread of the incoming light beam. Flip mirrors are used to alternate between the two measurements.

monic wavelength is measured in transmission by an Apogee Alta U1 Peltier cooled CCD camera. Rather then being strongly focused, the fundamental beam is collimated by a lens (not shown), and has a waist of ~ 0.5 mm, and a corresponding half-angular width of ~ 1 mrad. A 25 nm wide bandpass filter (Andover 766FS10-25) centered at a wavelength of 766.5 nm (sh filter) is placed in front of the silicon CCD camera to filter out the fundamental beam. The polarization of the incident fundamental beam is set to either s or p using a Glan-Thompson polarizing beamsplitter cube. Furthermore, a half-wave plate is placed before the polarizer (not shown) to adjust the power at the fundamental wavelength that is incident on the sample. Typically, an average power of ~ 10 mW is used in the experiments.

Linear transmission measurements are performed for wavelengths between 650 and 1700 nm using white light from a halogen lamp coupled to a 50 μm multimode fiber. The output of this fiber is imaged onto the sample with a 2 times magnification to create a 100 μm spot on the sample. The transmitted light is collected into a 400 μm fiber and then sent to a fiber-coupled grating spectrometer. Visible light is detected with a silicon CCD array spectrometer (Ocean Optics USB2000) with a spectral resolution of ≈ 1.5 nm, while the spectrum in the near infrared is detected with an InGaAs array spectrometer (Ocean Optics NIR512) with a ≈ 3 nm spectral resolution. The measurements are done with a very low numerical aperture of the incident beam of NA ≈ 0.01, set by inserting an aperture in the beam path. A Glan-Thompson polarizing beamsplitter cube in a parallel part of the beam is used to measure the transmission of both s- and p-polarized light as a function of wavelength and angle of incidence.

6.4 Results and discussion

The linear transmission and reflection spectra of two-dimensional photonic crystal slabs are well-known, and show a number of asymmetric, dispersive lineshapes [58, 59] due to the coupling of the incident light to one of the leaky modes of the photonic crystal slab via diffraction from the photonic lattice. The coupling of a continuum of modes to a single resonant channel leads to interference between the direct (non-resonant) and indirect (resonant) channel, as was first described by Fano [66]. For a photonic crystal slab, the direct channel corresponds to the Fresnel reflection of the slab, while the resonant channel is created by diffraction of incoming light from the regular photonic lattice into a guided mode of the structure [60].
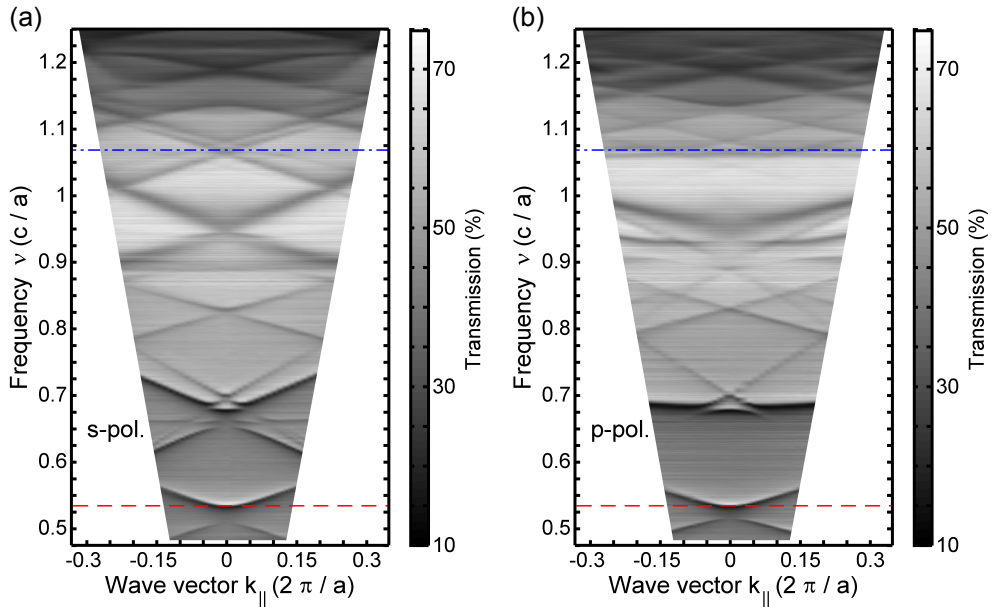
Figure 6.2 shows a gray scale plot of the measured transmission as a func-

tion of frequency (vertical axis) and the in-plane wave vector $k_{||}$ (horizontal axis), for both *s*- (a) and *p*-polarized (b) incident light. The crystal is oriented so that the parallel component of the wave vector $k_{||}$ is along the crystallographic ΓM direction of the photonic lattice. The dark lines that are clearly visible in the figure correspond to the minima of the Fano lineshapes of the leaky modes. The dashed red and the dash-dot blue horizontal lines in the figure indicate the frequencies of the fundamental and the second harmonic.

The experimental transmission spectra $T(\nu) = |t(\nu)|^2$ in the wavelength range between 1400 and 1700 nm (i.e., frequencies ν between 0.48 and 0.58 c/a) are well described by two independent Fano resonances:

$$t(\nu) = t_D(\nu) + \frac{A_1\Gamma_1}{(\nu - \nu_1) + i(\Gamma_1 + \gamma_1)} + \frac{A_2\Gamma_2}{(\nu - \nu_2) + i(\Gamma_2 + \gamma_2)}, \qquad (6.1)$$

where $t_D(\nu)$ is the frequency dependent transmission through the slab given by the Fresnel coefficients of the layered medium. We assume that this direct

Figure 6.2. Gray scale plot of the measured transmission as a function of frequency (vertical axis) and wave vector $k_{||}$ (horizontal axis). Measurements are shown for *s*- (a) and *p*-polarized (b) incident light with $k_{||}$ along the ΓM symmetry direction of the square lattice. The dashed red and the dash-dot blue lines indicate the frequencies of the fundamental and the second harmonic light.

contribution can be approximated well by a linear function over this relatively small frequency range. The parameters $A_{1,2}$ and $\nu_{1,2}$ denote the amplitudes and resonance frequencies of the two modes, while $\Gamma_{1,2}+\gamma_{1,2}$ give the linewidths of the resonances. The radiative coupling to the mode is characterized by $\Gamma_{1,2}$. The loss, quantified by $\gamma_{1,2}$ includes both higher order diffraction as well as scattering loss due to imperfections of the structure. Accordingly, the quality factors of the modes are given by $Q_{1,2} = \nu_{1,2}/(2(\Gamma_{1,2} + \gamma_{1,2}))$ [68]. Figure 6.3 shows the frequencies $\nu_{1,2}$ as a function of the in-plane wave vector $k_{||}$ for both *s*- (blue circles) and *p*-polarized light (red diamonds). The frequencies display a clear avoided crossing caused by Bragg type scattering from the periodic array of holes. At normal incidence the leaky modes of the structure are
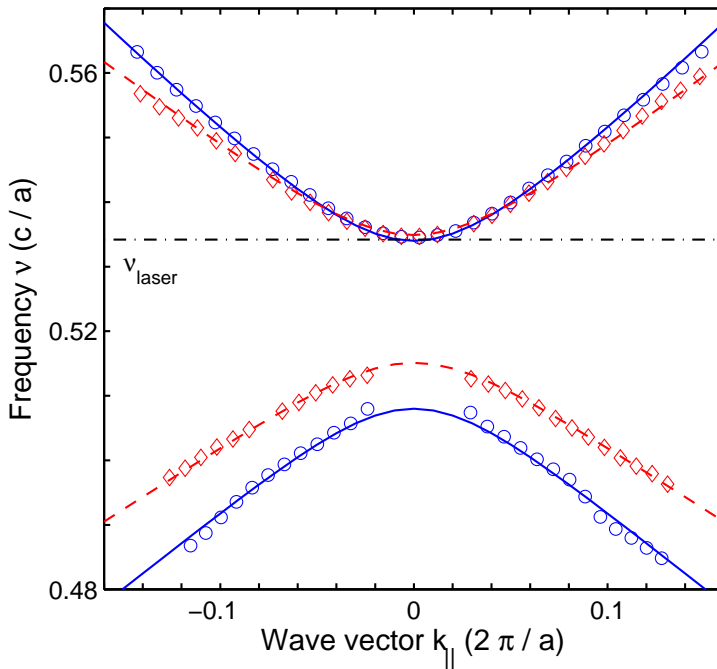
Figure 6.3. Dispersion relations of the lowest four leaky modes for the in-plane wave vector $k_{||}$ oriented along the ΓM direction of the square lattice. Each mode couples to the structure via an addition of one of the four (1,0) reciprocal lattice vectors. The measurements show two modes for both *s*- (blue circles) and *p*-polarized light (red diamonds). The solid blue and dashed red lines are fits to the experimental data points using a coupled mode theory, as described in the text. The laser (fundamental) frequency is indicated by the black dash-dot line.

resonant with the pulsed laser operating at 1535 nm (frequency 0.5342 c/a).

The avoided crossing between the leaky modes is well described by the coupled mode theory using a 2×2 Hamiltonian matrix [85, 86, 104]

$$H = \begin{pmatrix} E_1 & V \\ W & E_2 \end{pmatrix},$$

where E_1 and E_2 are energy eigenvalues of the uncoupled modes. For a closed system the energy eigenvalues are real, and the matrix H is Hermitian, and the off-diagonal elements are related by $V = W^*$. The eigenvalues of the coupled system lead to an avoided crossing with energies

$$E_{\pm} = \frac{E_1 + E_2}{2} \pm \sqrt{\frac{E_1 - E_2}{2} + VW}.$$

For an open or dissipative system, such as the leaky modes of the photonic crystal slab considered here, the same Hamiltonian can be used to describe the dynamics of the system. Complex-valued energies $E_{1,2} = h\nu_{1,2} + i(\Gamma_{1,2} + \gamma_{1,2})$ contain both the resonance frequency and the linewidth of the leaky photonic modes. Keeping the restriction $V = W^*$ corresponds to so-called internal coupling since the only difference to the Hermitian coupling is that both modes are individually coupled to the continuum. The fully non-Hermitian case with $V \neq W^*$ corresponds to external coupling, where the modes are coupled via the continuum. An important feature of this external coupling is that it creates a mode with a considerably increased lifetime (subradiant mode), and as a consequence a second mode with a shorter lifetime (superradiant mode). As can be seen from Figure 6.3, modes below the laser frequency (ν_{laser}) become subradiant at normal incidence and disappear from the measured transmission spectra.

For our geometry the leaky modes are excited via diffraction using one of the four $(1, 0)$ reciprocal lattice vectors. For a parallel component of the wave vector in the ΓM $(1, 1)$ direction, the dispersion of the modes of the uncoupled system are obtained by folding the dispersion relation of the fundamental TE waveguide mode. The resulting dispersion relations of the uncoupled modes $\nu_{1,2}$ can be expressed in dimensionless units as:

$$\nu_{1,2} = \nu_0 \sqrt{\left(1 \pm \frac{\alpha k_{||}}{\sqrt{2}}\right)^2 + \left(\frac{\alpha k_{||}}{\sqrt{2}}\right)^2}, \tag{6.2}$$

where ν_0 is the center frequency at normal incidence, and α is a dimensionless parameter that we introduced to control the slope $\partial\nu_{1,2}/\partial k_{||}$. The physical

interpretation of this parameter is that the phase velocity ($\propto \nu/k$) and the group velocity ($\propto \partial\nu/\partial k$) are different.

The avoided resonance crossing in Fig. 6.3 is well described by a center frequency of 0.5210±0.0001 and a frequency splitting of 0.0130±0.0002 for *s*-polarized light, and a center frequency of 0.5250±0.0001 and a frequency splitting of 0.0099±0.0001 for *p*-polarized light. The corresponding values for α are 0.733±0.004 and 0.577±0.002 respectively. The resulting dispersion using this relatively simple model is represented by the solid lines for *s*-polarized light and with dashed lines for *p*-polarized light in the figure. We stress that the complete band structure of the leaky modes can be obtained by using for instance finite difference time domain (FDTD) simulation software package MEEP [61]. These calculations will correctly predict the dispersion of the modes and the coupling between the *s*- and *p*-polarized modes, but do not give physical insight. Our model gives an analytical expression for the resonance frequency of the mode close to the laser (fundamental) frequency. This expression allows to quantify the detuning $\Delta\nu_F(k_{||})$ of the leaky mode relative to the fundamental frequency. It is this detuning, in units of the linewidth of the resonance, that controls the power that leaks into the resonant mode and thus plays an important role in second harmonic experiments. The amplitude of the fundamental field in the leaky mode, excited by the fundamental beam at frequency ν_F, as a function of $k_{||}$ is described by a Lorentzian [60]

$$
\begin{aligned}
E_F(k_{||}) \quad &\propto \quad \frac{g_1(k_{||})}{(\nu_1(k_{||}) - \nu_F) + ig_1(k_{||})} \\
&= \quad \frac{1}{i + \Delta\nu_F(k_{||})/g_1(k_{||})},
\end{aligned}
$$

where $\nu_1(k_{||})$ and $g_1(k_{||})$ represent the dispersion relation and the linewidth of the leaky mode close to the fundamental frequency.

Neglecting resonances at the second harmonic frequency, the intensity of the second harmonic signal I_{SH} as a function of the in-plane wave vector $k_{||}$ is given by

$$
I_{SH}(k_{||}) = I_D + \left(\frac{A_F}{1 + \frac{\Delta_F(k_{||})^2}{g_1(k_{||})^2}} \right)^2 . \tag{6.3}
$$

The first term in the sum (I_D) represents the direct (non-resonant) contribution, while the second term in the sum represents the resonantly enhanced second harmonic signal with an amplitude A_F.

Figure 6.4 shows the measured second harmonic signal in transmission for various angles of incidence. The data are plotted as a function of the in-plane

wave vector $k_{||}$ of the s-polarized fundamental beam (blue circles). As a result of the resonant coupling to leaky modes of the structure, four distinct peaks are clearly observed in the logarithmic plot at $k_{||} = 0$, $k_{||} = \pm 0.085$, and $k_{||} = -0.38 \times 2\pi/a$. At normal incidence ($k_{||} = 0$), the fundamental beam couples resonantly to the structure (see Fig. 6.3), and we measure the highest second harmonic value of 72000 ± 2000 cts/s. This value is more than $10000 \times$ larger than the measured non-resonant contribution of 6.9 ± 0.2 cts/s, determined by taking the averaged value of the measured signal in the interval $k_{||} \in [-0.28, -0.22] \times 2\pi/a$. For $k_{||} \sim 0.25 \times 2\pi/a$ the detuning of the fundamental beam from the leaky modes is maximum. A secondary maximum in the SH signal at $k_{||} = -0.38 \times 2\pi/a$ ($\theta = -45°$) with a value of around 7500 cts/s,
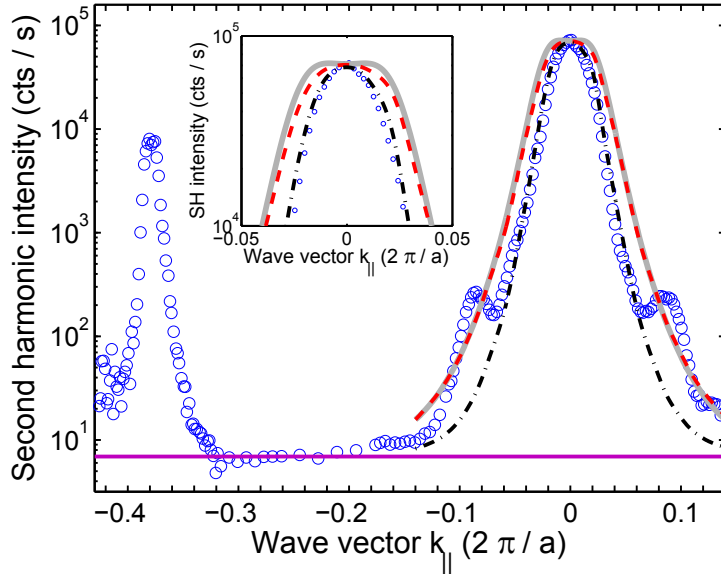
Figure 6.4. Measured second harmonic (SH) intensity in transmission as a function of the wave vector $k_{||}$ of the s-polarized fundamental beam (blue circles). The resonantly enhanced signal is more than $10000 \times$ larger than the non-resonant signal (horizontal line). The solid gray and the dashed red line are calculations taking into account the measured linewidth and dispersion of the mode that is resonant at the fundamental frequency. The dash-dot black line is a fit to the data using the linewidth as the only adjustable parameter. Both models fail to explain the peaks at $k_{||} = \pm 0.085 \times 2\pi/a$, which are due to resonant leaky modes at the second harmonic frequency. The inset zooms in on second harmonic intensity at normal incidence ($k_{||} = 0$).

is due to the resonant coupling of the fundamental beam to the (-1,-1) leaky mode of the structure. This resonant contribution to the SH signal disappears for the *p*-polarized fundamental beam (not shown), because the structure does not support leaky modes at the fundamental frequency in that case (Fig. 4.5 of Chapter 4).

The solid gray line in Figure 6.4 is the second harmonic signal calculated using Equation 6.3 with no adjustable parameters. We use the dispersion relation of the *s*-polarized leaky mode close to the fundamental frequency as given by Eq. 6.2, and take the measured average quality factor of the leaky mode $Q_1 = 90$ as a measure of the linewidth. For a fundamental frequency $\nu_F = 0.5342$ c/a this translates to a linewidth of $g_1 = \nu_F/(2Q_1) = 0.003$ c/a. For the amplitude of the resonant contribution we substitute $A_F = 268 \sqrt{\text{cts/s}}$, which is the square root of the measured SH signal at normal incidence, and for the non-resonant contribution we use the measured value of $I_D = 6.9$ cts/s. The calculated function has a local minimum at $k_{||} = 0$ instead of a maximum (see the inset of Fig. 6.4), and therefore doesn't explain the measured SH peak at normal incidence. This artefact occurs because the dispersion relation given by the coupled mode theory crosses the fundamental frequency twice, which is not true for the experimental data. Using a spline fit instead of the coupled mode theory to describe the dispersion relation of the leaky mode results in a second harmonic intensity which has a maximum at normal incidence (dashed red line) and matches better the measured signal. However, the model fails to predict the correct width of the measured SH signal and does not reproduce the peaks at $k_{||} = \pm \, 0.085 \times 2\pi/a$.

The main peak of the SH signal can be explained by Eq. 6.3 if the linewidth of the leaky mode close to the fundamental frequency is used as a fit parameter. The best fit, represented by the black dash-dot line in Figure 6.4, gives a linewidth of $g_1 = 0.00185 \pm 0.00006 \times c/a$, which is a factor 1.6 smaller than the value obtained from the linear transmission measurements.

The two peaks in the SH signal that occur at $k_{||} = \pm \, 0.085 \times 2\pi/a$, and have a value of ≈ 240 cts/s, cannot be explained by a relatively simple model that only considers the leaky mode at the fundamental frequency. As the in-plane wave vector of the incident fundamental beam is tuned away from $k_{||} = 0$ the power of the fundamental in the slab drops, and as a consequence the second harmonic intensity is expected to drop monotonically as well. Instead, the generated second harmonic field in the photonic crystal slab also couples to leaky modes of the structure. This double resonant coupling is the origin of the reduced width of the measured second harmonic signal at normal incidence and of the two additional peaks at $k_{||} = \pm \, 0.085 \times 2\pi/a$.

The incident laser beam couples to the fundamental TE mode of the photonic crystal slab waveguide. This mode has its **E**-field components predominantly in the plane of periodicity [82], i.e., in the x- and y-directions. The nonlinear tensor properties of the material are related to the cubic $4\bar{3}$m symmetry of the AlGaAs crystal. For this crystal symmetry the only nonzero tensor elements are $d_{14} = d_{25} = d_{36}$ [29]. Therefore, the generated second harmonic wave has the main **E**-field component in the z-direction, perpendicular to the plane of periodicity [29], and couples most efficiently to TM waveguide modes. The second harmonic intensity can be written in this case as:

$$
\begin{aligned}
I_{SH}(k_{||}) \;=\; & I_D + \left(\frac{A_F}{1 + \frac{\Delta_F(k_{||})^2}{g_1(k_{||})^2}} \right)^2 \times \frac{1}{1 + \frac{\Delta_{SH}(k_{||})^2}{g_3(k_{||})^2}} \\
& \times L^2 \frac{\sin^2(\Delta k L/2)}{(\Delta k L/2)^2}.
\end{aligned}
$$

Here, the first term is the direct contribution from the slab, while the second term is a product of the resonant contribution at the fundamental frequency, the resonant contribution at the second harmonic frequency, and a term related to the phase mismatch Δk between the waveguide modes involved. The phase mismatch $\Delta k = |2\mathbf{k}_{||}(\nu_F) - \mathbf{k}_{||}(\nu_{SH}) + \mathbf{G}|$, where $\mathbf{k}_{||}(\nu_F)$ is the in-plane wave vector of the fundamental beam, and $\mathbf{k}_{||}(\nu_{SH})$ is the in-plane wave vector of the wave at the second harmonic frequency ν_{SH}. The length L is the length of the sides of our square structure. The dispersion relation and the linewidth of the leaky mode close to the second harmonic frequency, $\nu_3(k_{||})$ and $g_3(k_{||})$, define the frequency detuning $(\nu_3(k_{||}) - \nu_{SH})/g_3(k_{||}) = \Delta_{SH}/g_3$, which determines how efficiently the generated second harmonic couples to external radiation. To understand the measured second harmonic signal, it is important to identify the leaky mode to which the second harmonic wave couples.

To find out which TM leaky modes can be excited at the second harmonic frequency, we use the nearly free photon picture introduced by Sakoda et al. [82]. In this picture, the photonic crystal slab is approximated with a dielectric slab with an effective dielectric permittivity that takes into account the effect of holes and different polarizations. The dispersion of the leaky modes of the photonic crystal slab is obtained by folding the dispersion of the waveguide modes of the dielectric slab back to the first Brillouin zone by adding an appropriate reciprocal lattice vector. Figure 6.5 shows the dispersion relation of relevant fundamental TE and fundamental TM leaky modes plotted over the measured transmission spectra for s-polarized light (from Fig. 6.2(a)). Figure 6.6 shows the dispersion relation of relevant fundamental

TE and fundamental TM leaky modes plotted over the measured transmission spectra for p-polarized light (from Fig. 6.2(b)). The dispersion of the TE leaky modes (dash-dot lines) is obtained by folding the dispersion of the fundamental TE waveguide mode of the slab with an effective dielectric permittivity $\epsilon_{TE} = 0.89 \times \epsilon$, where ϵ is the dielectric permittivity of $\mathrm{Al_{0.35}Ga_{0.65}As}$ [62]. Similarly, by folding the dispersion of the fundamental TM waveguide mode of a slab with an effective dielectric permittivity $\epsilon_{TM} = 0.95 \times \epsilon$ the dispersion of TM leaky modes (dashed lines) is obtained. Each leaky mode is denoted with a reciprocal lattice vector (G_x, G_y) used for folding of the guided modes back into the first Brillouin zone. For clarity, only the relevant leaky modes at the fundamental and at the second harmonic frequency are shown. The nearly free photon approximation doesn't take into account the interaction between the leaky modes, and as a consequence it cannot describe the frequency splitting between the modes of the photonic crystal slab. As can be seen, good agreement between the nearly free photon picture and measured spectra is obtained away from the crossings.

The horizontal purple lines in Figures 6.5 and 6.6 indicate the fundamental and second harmonic frequencies. The s-polarized fundamental wave couples to a mode of the family of (1,0) TE modes. The figures show that the generated SH signal could couple to one or more modes of the family of (2,1) TM modes at normal incidence. We stress that the leaky modes due to TM waveguide modes are generally less visible in transmission spectra than resonances due to TE modes. Therefore, we need to resort to the nearly free photon picture in order to resolve these modes. In the nearly free photon picture, the family of (2,1) TM modes is 8-fold degenerate at normal incidence, and it is impossible to say with certainty to which modes the second harmonic radiation is most likely to couple to. For nonzero angles of incidence, the dispersions of the (-2,-1) and (1,-2) modes are resonant with the second harmonic frequency. Therefore, we speculate that the generated second harmonic wave couples to one of these modes at angles of incidence of $\theta = \pm\, 9.1°$, indicated by the dotted lines in Figures 6.5 and 6.6. Since the measured second harmonic signal is elliptically polarized, we conclude that the second harmonic wave couples to both s- and p-polarized leaky modes of the structure.

Unfortunately, it is not possible to resolve the dispersion relations and the linewidths for the modes at the second harmonic frequency from the measured transmission spectra. The main reason for this is that there are other resonances due to TE modes around the second harmonic frequency. All these modes interact, and as a consequence the transmission spectra do not consist of isolated and easily recognizable Fano lineshapes superimposed on top of the
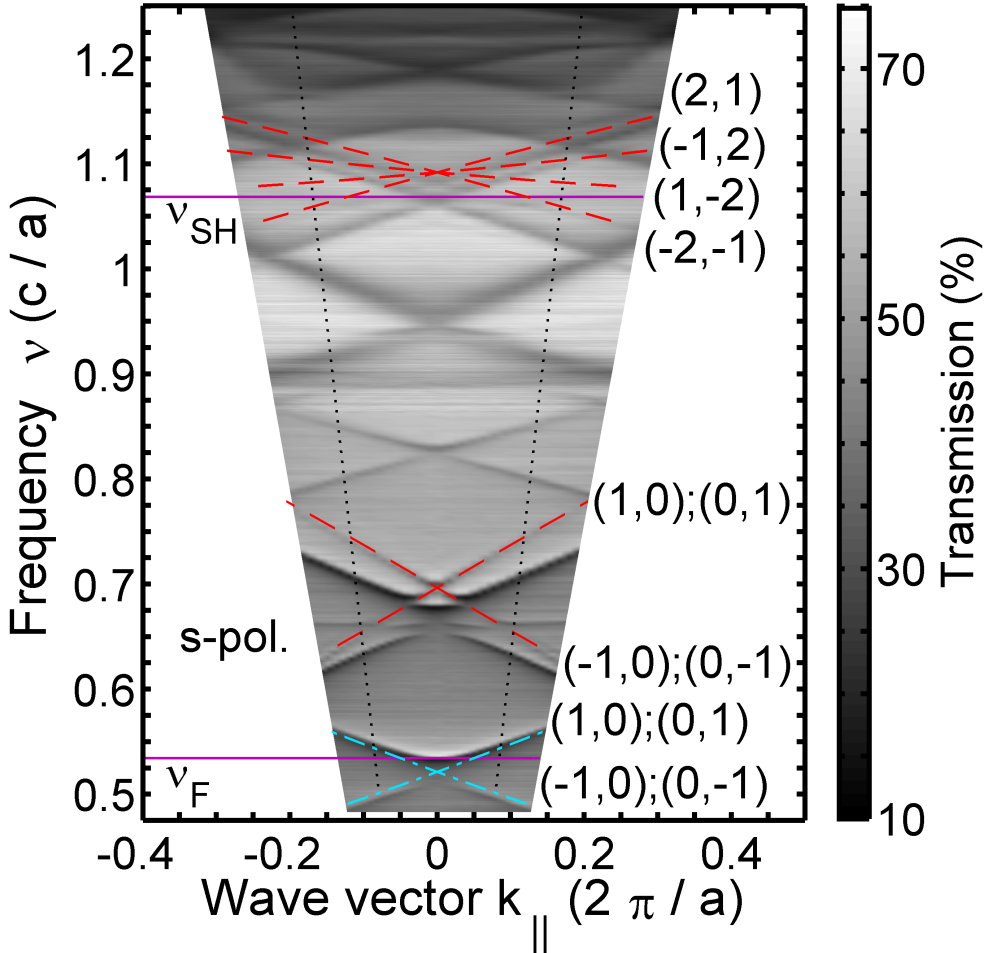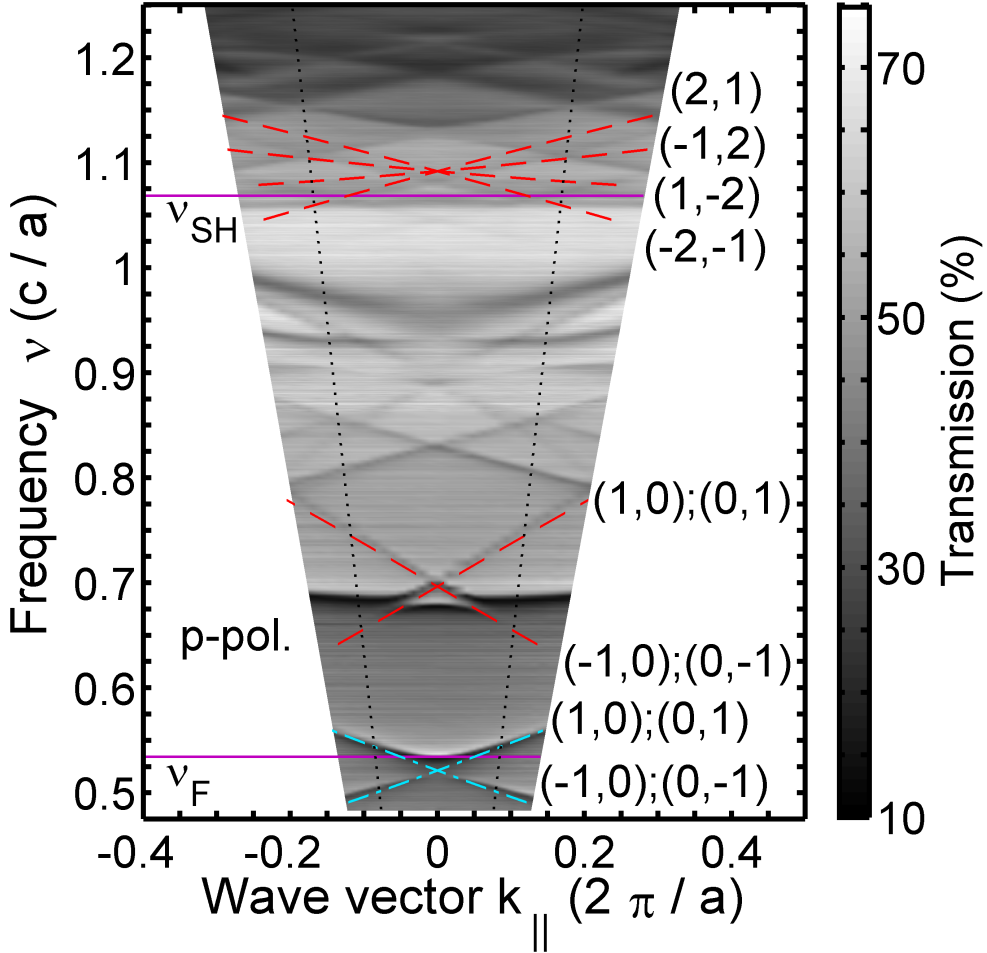
Figure 6.5. Dispersion relation of leaky TE (dash-dot lines) and TM (dashed lines) modes in the nearly free photon picture, plotted on top of the measured transmission data for *s*-polarized light (from Fig. 6.2(a)). The dispersion relations are obtained by folding the dispersions of the fundamental TE and TM waveguide modes of a dielectric slab on a gel back to the first Brillouin zone. The fundamental and second harmonic frequencies, $\nu_F = 0.5342$ c/a and $\nu_{SH} = 1.0684$ c/a, are indicated by horizontal purple lines. The dotted lines indicate constant angles of incidence $\theta = \pm 9.1°$.

Figure 6.6. Dispersion relation of leaky TE (dash-dot lines) and TM (dashed lines) modes in the nearly free photon picture, plotted on top of the measured transmission data for *p*-polarized light (from Fig. 6.2(b)). The dispersion relations are obtained by folding the dispersions of the fundamental TE and TM waveguide modes of a dielectric slab on a gel back to the first Brillouin zone. The fundamental and second harmonic frequencies, $\nu_F = 0.5342 \ c/a$ and $\nu_{SH} = 1.0684 \ c/a$, are indicated by horizontal purple lines. The dotted lines indicate constant angles of incidence $\theta = \pm \ 9.1°$.

Fabry-Perot background.

In principle, the generated second harmonic field can couple to TE leaky modes as well. Unlike TE modes of an ideal, infinitely long photonic crystal, TE leaky modes of the photonic crystal slab can have a small component of the **E**-field perpendicular to the plane of the slab [63], related to the absence of the continuous translational symmetry in the direction perpendicular to the plane of periodicity. This small component of the fundamental electric field perpendicular to the plane of periodicity can give rise to a second harmonic field with an electric field component in the plane of periodicity which can efficiently couple to TE leaky modes. We estimate that this effect is much smaller compared to the contribution to the SH signal due to resonant coupling of the second harmonic waves to TM leaky modes.

6.5   Conclusions

We investigate the influence of leaky modes on the second harmonic signal generated in transmission from a two-dimensional $Al_{0.35}Ga_{0.65}As$ photonic crystal slab on a gel substrate. By tuning the angle of incidence of the fundamental beam we probe the resonant coupling of the fundamental and the second harmonic wave to leaky modes of the structure. At normal incidence, both the fundamental and the second harmonic wave resonantly couple to the structure, and we measure a second harmonic enhancement of more than $10000 \times$ compared to the measured non-resonant contribution. This is more than eight times larger than the experimental enhancement measured in reflection by Mondia et al. [48]. Two additional maxima can be clearly seen in the measured second harmonic for angles of incidence of $\pm 9.1°$. We explain this effect by a resonant coupling of the second harmonic wave to leaky modes of the photonic crystal slab. Compared to experimental results reported in References [48, 49], our measurements convincingly show the influence of resonant effects at second harmonic frequency.

Using a relatively simple coupled mode theory rather than full numerical calculations we analyze the effects of resonant coupling of waves at the fundamental and the second harmonic frequency to leaky modes of the structure on the second harmonic generation. This coupled mode approach offers valuable physical insight and is applicable to less-than-perfect structures. This makes it a very useful tool for future analysis and design of both linear and nonlinear optical properties of photonic crystal slabs.

Bibliography

[1] P. Vukusic, J. R. Sambles, C. R. Lawrence, and R. J. Wootton, *Quantified interference and diffraction in single Morpho butterfly scales*, Proceedings of the Royal Society of London. Series B: Biological Sciences **266**, 1403 (1999).

[2] J. W. Galusha, L. R. Richey, J. S. Gardner, J. N. Cha, and M. H. Bartl, *Discovery of a diamond-based photonic crystal structure in beetle scales*, Phys. Rev. E **77**, 050904 (2008).

[3] J. V. Sanders, *Colour of Precious Opal*, Nature **204**, 1151 (1964).

[4] P. Vukusic and J. R. Sambles, *Photonic structures in biology*, Nature **424**, 852 (2003).

[5] E. Yablonovitch, *Inhibited spontaneous emission in solid-state physics and electronics*, Phys. Rev. Lett. **58**, 2059 (1987).

[6] S. John, *Strong localization of photons in certain disordered dielectric superlattices*, Phys. Rev. Lett. **58**, 2486 (1987).

[7] E. Yablonovitch, T. J. Gmitter, and K. M. Leung, *Photonic band structure: The face-centered-cubic case employing nonspherical atoms*, Phys. Rev. Lett. **67**, 2295 (1991).

[8] T. F. Krauss, R. M. D. L. Rue, and S. Brand, *Two-dimensional photonic-bandgap structures operating at near-infrared wavelengths*, Nature **383**, 699 (1996).

[9] T. F. Krauss and R. M. De la Rue, *Photonic crystals in the optical regime - past, present and future*, Prog. Quant. Electron. **23**, 51 (1999).

[10] K. Busch, G. von Freymann, S. Linden, S. Mingaleev, L. Tkeshelashvili, and M. Wegener, *Periodic nanostructures for photonics*, Physics Reports **444**, 101 (2007).

[11] Masaya Notomi, Reports on Progress in Physics **73**, 096501 (2010).

[12] Neil W. Ashcroft and N. David Mermin, *Solid state physics*, Thomson Learning, Inc., 1976.

[13] Marcel A. Verheijen, George Immink, Thierry de Smet, Magnus T. Borgström, and Erik P. A. M. Bakkers, *Growth kinetics of heterostructured GaP–GaAs nanowires*, J. Am. Chem. Soc. **128**, 1353 (2006).

[14] Michael H. Huang, Samuel Mao, Henning Feick, Haoquan Yan, Yiying Wu, Hannes Kind, Eicke Weber, Richard Russo, and Peidong Yang, *Room-temperature ultraviolet nanowire nanolasers*, Science **292**, 1897 (2001).

[15] Justin C. Johnson, Heon-Jin Choi, Kelly P. Knutsen, Richard D. Schaller, Peidong Yang, and Richard J. Saykally, *Single gallium nitride nanowire lasers*, Nature Mater. **1**, 106 (2002).

[16] Xiangfeng Duan, Yu Huang, Ritesh Agarwai, and Charles M. Lieber, *Single-nanowire electrically driven lasers*, Nature **421**, 241 (2003).

[17] Matt Law, Donald J. Sirbuly, Justin C. Johnson, Josh Goldberger, Richard J. Saykally, and Peidong Yang, *Nanoribbon waveguides for sub-wavelength photonics integration*, Science **305**, 1269 (2004).

[18] L. Tong, R. R. Gattass, J. B. Ashcom, S. He, J. Lou, M. Shen, I. Maxwell, and E. Mazur, *Subwavelength-diameter silica wires for low-loss optical wave guiding*, Nature **426**, 816 (2003).

[19] Jianfang Wang, Mark S. Gudiksen, Xiangfeng Duan, Yi Cui, and Charles M. Lieber, *Highly polarized photoluminescence and photodetection from single indium phosphide nanowires*, Science **293**, 1455 (2001).

[20] Hannes Kind, Haoquan Yan, Benjamin Messer, Matthew Law, and Peidong Yang, *Nanowire ultraviolet photodetectors and optical switches*, Adv. Mater. **14**, 158 (2002).

[21] Y. Gu, E.-S. Kwak, J. L. Lensch, J. E. Allen, T. W. Odom, and L. J. Lauhon, *Near-field scanning photocurrent microscopy of a nanowire photodetector*, Appl. Phys. Lett. **87**, 043111 (2005).

[22] M. Law, L. E. Greene, J. C. Johnson, R. Saykally, and P. Yang, *Nanowire dye-sensitized solar cells*, Nat Mater **4**, 455 (2005).

[23] B. Tian, X. Zheng, T. J. Kempa, Y. Fang, N. Yu, G. Yu, J. Huang, and C. M. Lieber, *Coaxial silicon nanowires as solar cells and nanoelectronic power sources*, Nature **449**, 885 (2007).

[24] J. C. Johnson, H. Yan, R. D. Schaller, P. B. Petersen, P. Yang, and R. J. Saykally, *Near-Field Imaging of Nonlinear Optical Mixing in Single Zinc Oxide Nanowires*, Nano Letters **2**, 279 (2002).

[25] Y. Nakayama, P. J. Pauzauskie, A. Radenovic, R. M. Onorato, R. J. Saykally, J. Liphardt, and P. Yang, *Tunable nanowire nonlinear optical probe*, Nature **447**, 1098 (2007).

[26] Y. Cui, Q. Wei, H. Park, and C. M. Lieber, *Nanowire Nanosensors for Highly Sensitive and Selective Detection of Biological and Chemical Species*, Science **293**, 1289 (2001).

[27] O. L. Muskens, M. T. Borgström, E. P. A. M. Bakkers, and J. Gómez Rivas, *Giant optical birefringence in ensembles of semiconductor nanowires*, Appl. Phys. Lett. **89**, 233117 (2006).

[28] J. P. van der Ziel, *Phase - matched harmonic generation in a laminar structure with wave propagation in the plane of the layers*, Appl. Phys. Lett. **26**, 60 (1975).

[29] Robert W. Boyd, *Nonlinear optics*, Academic Press, second edition edition, 2003.

[30] M. M. Fejer, *Nonlinear optical frequency conversion*, Phys. Today **47(5)**, 25 (1994).

[31] I. Shoji, T. Kondo, A. Kitamoto, M. Shirane, and R. Ito, *Absolute scale of second-order nonlinear-optical coefficients*, J. Opt. Soc. Am. B **14**, 2268 (1997).

[32] V. G. Dmitriev, G. G. Gurzadyan, and D. N. Nikogosyan, *Handbook of Nonlinear Optical Crystals*, Springer, 1999.

[33] N. Bloembergen and A. J. Sievers, *Nonlinear optical properties of periodic laminar structures*, Appl. Phys. Lett. **17**, 483 (1970).

[34] G. P. Agrawal, *Nonlinear Fiber Optics*, Academic Press, third edition, 2001.

[35] M. Yazawa, M. Koguchi, and K. Hiruma, *Heteroepitaxial ultrafine wire-like growth of InAs on GaAs substrates*, Appl. Phys. Lett. **58**, 1080 (1991).

[36] Otto L. Muskens, Silke L. Diedenhofen, Maarten H. M. van Weert, Magnus T. Borgström, Erik P. A. M. Bakkers, and Jaime Gómez Rivas, *Epitaxial growth of aligned semiconductor nanowire metamaterials for photonic applications*, Adv. Funct. Mater. **18**, 1039 (2008).

[37] A. Fiore, V. Berger, E. Rosencher, P. Bravetti, and J. Nagle, *Phase matching using an isotropic nonlinear optical material*, Nature **391**, 463 (1998).

[38] private communication with Silke L. Diedenhofen.

[39] J. C. Maxwell Garnett, *Colours in Metal Glasses and in Metallic Films*, Philos. Trans. R. Soc. London Ser. A **203**, 385 (1904).

[40] J. C. Maxwell Garnett, *Colours in Metal Glasses, in Metallic Films, and in Metallic Solutions. II*, Philos. Trans. R. Soc. London Ser. A **205**, 237 (1906).

[41] P. D. Maker, R. W. Terhune, M. Nisenoff, and C. M. Savage, *Effects of dispersion and focusing on the production of optical harmonics*, Phys. Rev. Lett. **8**, 21 (1962).

[42] C. J. Novotny, C. T. DeRose, R. A. Norwood, and P. K. L. Yu, *Linear Electrooptic Coefficient of InP Nanowires*, Nano Letters **8**, 1020 (2008).

[43] J. A. Armstrong, N. Bloembergen, J. Ducuing, and P. S. Pershan, *Interactions between Light Waves in a Nonlinear Dielectric*, Phys. Rev. **127**, 1918 (1962).

[44] M. M. Fejer, G. A. Magel, D. H. Jundt, and R. L. Byer, *Quasi-phase-matched second harmonic generation: tuning and tolerances*, IEEE J. Quantum Electron. **28**, 2631 (1992).

[45] V. Berger, *Nonlinear Photonic Crystals*, Phys. Rev. Lett. **81**, 4136 (1998).

[46] M. Scalora, M. J. Bloemer, A. S. Manka, J. P. Dowling, C. M. Bowden, R. Viswanathan, and J. W. Haus, *Pulsed second-harmonic generation in nonlinear, one-dimensional, periodic structures*, Phys. Rev. A **56**, 3166 (1997).

[47] A. R. Cowan and Jeff F. Young, *Mode matching for second-harmonic generation in photonic crystal waveguides*, Phys. Rev. B **65**, 085106 (2002).

[48] J. P. Mondia, H. M. van Driel, W. Jiang, A. R. Cowan, and J. F. Young, *Enhanced second-harmonic generation from planar photonic crystals*, Opt. Lett. **28**, 2500 (2003).

[49] J. Torres, D. Coquillat, R. Legros, J. P. Lascaray, F. Teppe, D. Scalbert, D. Peyrade, Y. Chen, O. Briot, M. Le Vassor d'Yerville, E. Centeno, D. Cassagne, and J. P. Albert, *Giant second-harmonic generation in a one-dimensional GaN photonic crystal*, Phys. Rev. B **69**, 085105 (2004).

[50] C. Reese, B. Gayral, B. D. Gerardot, A. Imamoğlu, P. Petroff, and E. L. Hu, *High-Q photonic crystal microcavities fabricated in a thin GaAs membrane*, J. Vac. Sci. Technol. B **19**, 2749 (2001).

[51] Philips MiPlaza - Cedova, http://www.cedova.com.

[52] ZEON corporation, http://www.zeon.co.jp.

[53] T. Maeda, J. W. Lee, R. J. Shul, J. Han, J. Hong, E. S. Lambers, S. J. Pearton, C. R. Abernathy, and W. S. Hobson, *Inductively coupled plasma etching of III-V semiconductors in BCl_3-based chemistries I. GaAs, GaN, GaP, GaSb and AlGaAs*, Appl. Surf. Sci. **143**, 174 (1999).

[54] E. F. C. Driessen, *Coupling light to periodic nanostructures*, PhD thesis, Leiden University, 2009.

[55] J. H. Kim, D. H. Lim, and G. M. Yang, *Selective etching of Al-GaAs/GaAs structures using the solutions of citric acid/H_2O_2 and deionized H_2O/buffered oxide etch*, J. Vac. Sci. Technol. B **16**, 558 (1998).

[56] K. Hennessy, C. Reese, A. Badolato, C. F. Wang, A. Imamoğlu, P. M. Petroff, E. Hu, G. Jin, S. Shi, and D. W. Prather, *Square-lattice photonic crystal microcavities for coupling to single InAs quantum dots*, Appl. Phys. Lett. **83**, 3650 (2003).

[57] S. Fan and J. D. Joannopoulos, *Analysis of guided resonances in photonic crystal slabs*, Phys. Rev. B **65**, 235112 (2002).

[58] M. Kanskar, P. Paddon, V. Pacradouni, R. Morin, A. Busch, J. F. Young, S. R. Johnson, J. MacKenzie, and T. Tiedje, *Observation of leaky slab modes in an air-bridged semiconductor waveguide with a two-dimensional photonic lattice*, Appl. Phys. Lett. **70**, 1438 (1997).

[59] V. N. Astratov, D. M. Whittaker, I. S. Culshaw, R. M. Stevenson, M. S. Skolnick, T. F. Krauss, and R. M. De la Rue, *Photonic band-structure effects in the reflectivity of periodically patterned waveguides*, Phys. Rev. B **60**, R16255 (1999).

[60] S. Fan, W. Suh, and J. D. Joannopoulos, *Temporal coupled-mode theory for the Fano resonance in optical resonators*, J. Opt. Soc. Am. A **20**, 569 (2003).

[61] A. Farjadpour, D. Roundy, A. Rodriguez, M. Ibanescu, P. Bermel, J. D. Joannopoulos, S. G. Johnson, and G. W. Burr, *Improving accuracy by subpixel smoothing in the finite-difference time domain*, Opt. Lett. **31**, 2972 (2006).

[62] Edward D. Palik, *Handbook of Optical Constants of Solids*, volume II, Academic Press, Inc., 1991.

[63] Steven G. Johnson, Shanhui Fan, Pierre R. Villeneuve, J. D. Joannopoulos, and L. A. Kolodziejski, *Guided modes in photonic crystal slabs*, Phys. Rev. B **60**, 5751 (1999).

[64] P. Paddon and J. F. Young, *Two-dimensional vector-coupled-mode theory for textured planar waveguides*, Phys. Rev. B **61**, 2090 (2000).

[65] U. Fano, *The theory of anomalous diffraction gratings and of quasi-stationary waves on metallic surfaces (Sommerfeld's waves)*, J. Opt. Soc. Am. **31**, 213 (1941).

[66] U. Fano, *Effects of Configuration Interaction on Intensities and Phase Shifts*, Phys. Rev. **124**, 1866 (1961).

[67] E. F. C. Driessen, D. Stolwijk, and M. J. A. de Dood, *Asymmetry reversal in the reflection from a two-dimensional photonic crystal*, Opt. Lett. **32**, 3137 (2007).

[68] John D. Joannopoulos, Steven G. Johnson, Joshua N. Winn, and Robert D. Meade, *Photonic Crystals: Molding the Flow of Light*, Princeton University Press, 2nd edition, 2008.

[69] K. B. Crozier, V. Lousse, O. Kilic, S. Kim, S. Fan, and O. Solgaard, *Air-bridged photonic crystal slabs at visible and near-infrared wavelengths*, Phys. Rev. B **73**, 115126 (2006).

[70] E. Chow, A. Grot, L. W. Mirkarimi, M. Sigalas, and G. Girolami, *Ultra-compact biochemical sensor built with two-dimensional photoniccrystal microcavity*, Opt. Lett. **29**, 1093 (2004).

[71] K. M. Ho, C. T. Chan, and C. M. Soukoulis, *Existence of a photonic gap in periodic dielectric structures*, Phys. Rev. Lett. **65**, 3152 (1990).

[72] R. D. Meade, K. D. Brommer, A. M. Rappe, and J. D. Joannopoulos, *Existence of a photonic band gap in two dimensions*, Appl. Phys. Lett. **61**, 495 (1992).

[73] C. Chan, S. Datta, K. Ho, and C. Soukoulis, *A7 structure: A family of photonic crystals*, Phys. Rev. B **50**, 1988 (1994).

[74] J. J. Wierer, A. David, and M. M. Megens, *III-nitride photonic-crystal light-emitting diodes with high extraction efficiency*, Nat Photon **3**, 163 (2009).

[75] T. van der Sar, E. C. Heeres, G. M. Dmochowski, G. de Lange, L. Robledo, T. H. Oosterkamp, and R. Hanson, *Nanopositioning of a diamond nanocrystal containing a single nitrogen-vacancy defect center*, Appl. Phys. Lett. **94**, 173104 (2009).

[76] J. R. Rabeau, P. Reichart, G. Tamanyan, D. N. Jamieson, S. Prawer, F. Jelezko, T. Gaebel, I. Popa, M. Domhan, and J. Wrachtrup, *Implantation of labelled single nitrogen vacancy centers in diamond using [sup 15]N*, Appl. Phys. Lett. **88**, 023113 (2006).

[77] F. Jelezko, A. Volkmer, I. Popa, K. K. Rebane, and J. Wrachtrup, *Coherence length of photons from a single quantum system*, Phys. Rev. A **67**, 041802 (2003).

[78] V. V. Dobrovitski, A. E. Feiguin, D. D. Awschalom, and R. Hanson, *Decoherence dynamics of a single spin versus spin ensemble*, Phys. Rev. B **77**, 245212 (2008).

[79] Ioffe Institute, "New semiconductor materials database.", http://www.ioffe.ru/SVA/NSM.

[80] Gel-Pak, http://www.gelpak.com.

[81] T. Ochiai and K. Sakoda, *Dispersion relation and optical transmittance of a hexagonal photonic crystal slab*, Phys. Rev. B **63**, 125107 (2001).

[82] T. Ochiai and K. Sakoda, *Nearly free-photon approximation for two-dimensional photonic crystal slabs*, Phys. Rev. B **64**, 045108 (2001).

[83] W. L. Barnes, T. W. Preist, S. C. Kitson, and J. R. Sambles, *Physical origin of photonic energy gaps in the propagation of surface plasmons on gratings*, Phys. Rev. B **54**, 6227 (1996).

[84] C. Ropers, D. J. Park, G. Stibenz, G. Steinmeyer, J. Kim, D. S. Kim, and C. Lienau, *Femtosecond light transmission and subradiant damping in plasmonic crystals*, Phys. Rev. Lett. **94**, 113901 (2005).

[85] M. J. A. de Dood, E. F. C. Driessen, D. Stolwijk, and M. P. van Exter, *Observation of coupling between surface plasmons in index-matched hole arrays*, Phys. Rev. B **77**, 115437 (2008).

[86] J. Wiersig, *Formation of Long-Lived, Scarlike Modes near Avoided Resonance Crossings in Optical Microcavities*, Phys. Rev. Lett. **97**, 253901 (2006).

[87] Q. H. Song and H. Cao, *Improving Optical Confinement in Nanostructures via External Mode Coupling*, Phys. Rev. Lett. **105**, 053902 (2010).

[88] A. E. Miroshnichenko, S. Flach, and Y. S. Kivshar, *Fano resonances in nanoscale structures*, Rev. Mod. Phys. **82**, 2257 (2010).

[89] R. K. Adair, C. K. Bockelman, and R. E. Peterson, *Experimental Corroboration of the Theory of Neutron Resonance Scattering*, Phys. Rev. **76**, 308 (1949).

[90] K. Kobayashi, H. Aikawa, S. Katsumoto, and Y. Iye, *Tuning of the Fano Effect through a Quantum Dot in an Aharonov-Bohm Interferometer*, Phys. Rev. Lett. **88**, 256806 (2002).

[91] M. Mendoza, P. A. Schulz, R. O. Vallejos, and C. H. Lewenkopf, *Fano resonances in the conductance of quantum dots with mixed dynamics*, Phys. Rev. B **77**, 155307 (2008).

[92] C. Genet, M. P. van Exter, and J. P. Woerdman, *Fano-type interpretation of red shifts and red tails in hole array transmission spectra*, Opt. Commun. **225**, 331 (2003).

[93] A. Bärnthaler, S. Rotter, F. Libisch, J. Burgdörfer, S. Gehler, U. Kuhl, and H.-J. Stöckmann, *Probing Decoherence through Fano Resonances*, Phys. Rev. Lett. **105**, 056801 (2010).

[94] M. Galli, M. Agio, L. C. Andreani, M. Belotti, G. Guizzetti, F. Marabelli, M. Patrini, P. Bettotti, L. Dal Negro, Z. Gaburro, L. Pavesi, A. Lui, and P. Bellutti, *Spectroscopy of photonic bands in macroporous silicon photonic crystals*, Phys. Rev. B **65**, 113111 (2002).

[95] A. A. Clerk, X. Waintal, and P. W. Brouwer, *Fano Resonances as a Probe of Phase Coherence in Quantum Dots*, Phys. Rev. Lett. **86**, 4636 (2001).

[96] S. Klaiman, N. Moiseyev, and H. R. Sadeghpour, *Interpretation of the Fano lineshape reversal in quantum waveguides*, Phys. Rev. B **75**, 113305 (2007).

[97] M. Galli, S. L. Portalupi, M. Belotti, L. C. Andreani, L. O'Faolain, and T. F. Krauss, *Light scattering and Fano resonances in high-Q photonic crystal nanocavities*, Applied Physics Letters **94**, 071101 (2009).

[98] S. Fan, *Sharp asymmetric line shapes in side-coupled waveguide-cavity systems*, Appl. Phys. Lett. **80**, 908 (2002).

[99] E. Flück, *Local interaction of light with periodic photonic structures*, PhD thesis, University of Twente, 2003.

[100] H. A. Haus, *Waves and fields in optoelectronics*, Prentice-Hall, New Jersey, 1984.

[101] M. Born and E. Wolf, *Principles of Optics*, Pergamon Press, 6th edition, 1980.

[102] Michiel J. A. de Dood, William T. M. Irvine, and Dirk Bouwmeester, *Nonlinear photonic crystals as a source of entangled photons*, Phys. Rev. Lett. **93**, 040504 (2004).

[103] A. D. Bristow, J. P. Mondia, and H. M. van Driel, *Sum and difference frequency generation as diagnostics for leaky eigenmodes in two-dimensional photonic crystal waveguides*, J. Appl. Phys. **99**, 023105 (2006).

[104] J. von Neumann and E.P. Wigner, *Über das Verhalten von Eigenwerten bei adiabatischen Prozessen*, Z. Physik **30**, 467 (1929).

Summary

Frequency conversion in two-dimensional photonic structures

With the advent of nanotechnology it became possible to structure semiconductor materials on a wavelength and subwavelength scale. This opened a door to novel materials called photonic structures with exciting linear and nonlinear optical properties. Semiconductor photonic crystals and nanowires are examples of these photonic structures. Photonic crystals are periodic dielectric structures with features on a wavelength and subwavelength scale with the periodicity in one, two, or all three spatial directions. Nanowires are essentially one-dimensional structures with diameters ranging from a few to several hundred nanometers and typical lengths of several micrometers. They can be grown in a random as well as in a periodic fashion on a suitable substrate.

This thesis presents an experimental study of second harmonic generation in two-dimensional aluminum gallium arsenide photonic crystal slabs (Chapters 3–6) and second harmonic generation in ensembles of aligned gallium phosphide nanowires (Chapter 2). The motivation behind using these III-V semiconductor photonic structures for frequency conversion is their relatively large nonlinearity. The extra dispersion due to the special arrangement of dielectric material in these novel structures may be used to compensate a phase mismatch in the nonlinear process.

Gallium phosphide nanowires are randomly grown on a gallium phosphide substrate by epitaxy at elevated temperatures using ~ 20 nm gold droplets as a catalyst. As-grown nanowires have a diameter determined by the size of gold droplets and a length determined by the growth time. A typical length of these wires is several micrometers. The high length-to-width aspect ratios of the

nanowires combined with the high refractive index of gallium phosphide can lead to strong birefringence. In Chapter 2 we investigate if this birefringence can be used to phase-match second harmonic generation. The enhancement of the second harmonic signal is only effective for nanowires that are much longer than the coherence length. However, long nanowires (> 10 μm) have a significantly reduced birefringence due to the bending of the wires. We also discuss a number of experiments that aim at separating the second harmonic generated in the substrate from the second harmonic generated in nanowires that are shorter than the coherence length. Unfortunately, we were not able to separate these two contributions.

Chapter 3 describes the fabrication of freestanding, two-dimensional photonic crystal slabs with a square lattice of holes perforated in a ~ 150 nm thick $Al_{0.35}Ga_{0.65}As$ slab. Samples that are investigated in this chapter have a hole radius of $r \sim 150$ nm, a lattice constant $a = 890$ nm, and a surface area of $\sim 300 \times 300$ μm^2. The freestanding slabs are supported by a GaAs substrate. The linear optical properties of these structures are investigated by measuring the reflection spectra as a function of angle of incidence. These spectra show dispersive, asymmetric lineshapes superimposed on top of a slowly oscillating background. The lineshapes can be understood in terms of the Fano model. Within this model, the interference between a direct (non-resonant) and an indirect (resonant) contribution gives rise to the asymmetric lineshape in the spectra. The direct contribution is due to the Fresnel reflection of the incident light from the slab, and the resonant contribution is due to the coupling of the incident light to a leaky waveguide mode via diffraction from the lattice. By using the Fano model it is possible to obtain the dispersion relation and the quality factor of the resonance from the experimental reflection spectra. The nonlinear optical properties of the photonic crystal slabs are investigated by measuring the nonlinear reflection spectra as a function of angle of incidence. We show that the resonant coupling of a pulsed laser at a wavelength of 1.535 μm can significantly enhance the second harmonic signal. A second harmonic enhancement of more than 4500 $\times$ compared to the non-resonant contribution is measured when the pulsed laser beam is tuned into resonance with one of the leaky modes of the structure.

Freestanding photonic crystal slabs are not flat, but they buckle because of a small lattice mismatch (0.05%) between the $Al_{0.35}Ga_{0.65}As$ material of the slab and the GaAs substrate. In Chapter 4, we present a novel technique to transfer a freestanding photonic crystal slab to a transparent gel layer. In contrast to the freestanding structures, the transferred structures are almost perfectly flat, and they allow for transmission measurements. Most importantly,

the resonant features in the measured reflection spectra of a structure on a gel are much more visible than those of a freestanding structure. Therefore, the transferred structures are more attractive for investigating the resonant coupling of light to photonic crystal slabs. In addition, we study in more detail an avoided crossing between two modes in experimental transmission spectra. At the avoided crossing one of the modes becomes long-lived (subradiant) and the other mode becomes short-lived (superradiant). For the subradiant mode we measure quality factors as high as $Q = 300$. This value is limited by the finite size of the structure, which suggests an excellent optical quality of the photonic crystal slabs transferred to the gel substrate.

The linear reflection and transmission spectra of a two-dimensional photonic crystal slab consist of asymmetric Fano lineshapes due to the resonant coupling of light to leaky modes of the photonic crystal slab via diffraction from the photonic lattice. The coupling of a continuum of modes to a single resonant channel leads to interference between the direct (non-resonant) and the indirect (resonant) channel. This is described by the Fano model. The generally accepted picture is that for a lossless system the sign of a real-valued parameter q of the Fano model determines the asymmetry of the lineshape. For a lossless and symmetric air-slab-air structure, the sign of q changes if the amplitude reflection coefficient of the direct contribution goes through zero. As a consequence, the asymmetry of the Fano lineshape in the reflection spectra for p-polarized light can be reversed by tuning the angle of incidence through Brewster's angle for the symmetric system. In Chapter 5 we show that for a lossless and asymmetric air-slab-gel structure it is also possible to change the asymmetry of the Fano lineshape by angle tuning without reaching the condition of zero amplitude. However, this requires a complex-valued parameter q and shows that the picture of a real-valued parameter q that controls the asymmetry is not complete. More importantly, this demonstrates that a Fano type resonance, characterized by a complex-valued parameter q is not necessarily a sign of microscopic processes of decoherence and/or dephasing.

Chapter 6 studies in more detail second harmonic generation from photonic crystal slabs transferred on a gel substrate. In contrast to Chapter 3, we use a collimated laser beam, and we measure the second harmonic signal in transmission instead in reflection as a function of angle of incidence. Compared to Chapter 3 we go a step further in understanding the importance of leaky modes at both the fundamental and second harmonic frequency for the nonlinear process of second harmonic generation. The main features of the experimental second harmonic signal as a function of angle of incidence are explained in terms of a relatively simple coupled mode theory. Unlike

full numerical calculations, our model offers direct insight into the underlying physical mechanism. Furthermore, the model does not assume parameters of an ideal two-dimensional photonic crystal slab. Instead, it uses measured dispersion relations and quality factors of relevant modes as well as the measured non-resonant second harmonic signal. This makes the model applicable to less-than-perfect structures with a finite size and a number of fabrication imperfections. At normal incidence, both the fundamental and the second harmonic field resonantly couple to leaky modes of the structure, and we measure second harmonic enhancements as large as $10000 \times$ compared to the non-resonant contribution. In addition, the measurements convincingly show the effect of the resonant coupling of the second harmonic wave to a leaky mode of the structure. The angular width of the measured second harmonic signal is a factor of 1.6 smaller than the width deduced from the linear optical properties of the leaky mode at the fundamental frequency. More obviously, two additional satellite peaks appear at angles of incidence of $\pm 9.1°$. These satellites can be explained by considering the resonant coupling of both the fundamental beam and the second harmonic beam to leaky modes of the photonic crystal slab. This accounts for the reduced width of the measured second harmonic signal at normal incidence and for the two satellite peaks, and shows the importance of a double resonant condition for efficient second harmonic generation from a photonic crystal.

Samenvatting

Frequentieconversie in tweedimensionale fotonische structuren

Moderne nanotechnologie maakt het mogelijk om halfgeleiderstructuren te bouwen op golflengte- en subgolflengteschaal. Dit heeft geleid tot nieuwe materialen, de zogenaamde fotonische structuren, met spannende lineaire en niet-lineaire optische eigenschappen. Voorbeelden van deze fotonische structuren zijn fotonische kristallen en nanodraadjes van halfgeleider materiaal. Fotonische kristallen bestaan uit een zich periodiek herhalende diëlectrische structuur, waarbij de periode in één, twee, of alledrie ruimtelijke richtingen vergelijkbaar of zelfs kleiner is dan de golflengte van licht. Nanodraadjes zijn min of meer ééndimensionale structuren, met een diameter tussen een paar nanometer en enkele honderden nanometers. Men kan ze laten groeien op zowel willekeurige als periodieke wijze op een geschikt substraat.

Dit proefschrift presenteert experimenteel onderzoek naar frequentieverdubbeling in platen van tweedimensionale aluminium-galliumarsenide fotonisch kristallen (hoofdstukken 3–6) en frequentieverdubbeling in gelijjkgerichte verzamelingen galliumfosfidenanodraadjes (hoofdstuk 2). De motivatie om deze III-V halfgeleidende structuren te gebruiken voor frequentieconversie is hun relatief grote niet-lineariteit. De extra dispersie, die optreedt wegens de bijzondere rangschikking van diëlectrisch materiaal in deze nieuwe structuren, kan worden gebruikt om te compenseren dat de fases in het niet-lineaire proces niet op elkaar aansluiten.

Galliumfosfidenanodraadjes worden bij verhoogde temperaturen door middel van epitaxie willekeurig gedeponeerd op een galliumfosfidesubstraat, met ~ 20 nm grote gouddruppeltjes als catalysator. De diameter van de zo ontstane

nanodraadjes wordt bepaald door de gouddruppeltjes, en de lengte door de groeitijd. De lengte van zulke draadjes is typisch enkele micrometers. De hoge lengte-breedteverhouding van de nanodraadjes, gecombineerd met de hoge brekingsindex van galliumfosfide, kan leiden tot zeer sterke dubbelbrekendheid. In hoofdstuk 2 onderzoeken we of deze dubbelbrekendheid gebruikt kan worden om faseaansluiting teweeg te brengen bij frequentieverdubbeling. Deze verbetering van het frequentieverdubbelingssignaal is alleen effectief bij nanodraadjes die veel langer zijn dan de coherentielengte. Bij langere nanodraadjes (> 10 μm) is de dubbelbrekendheid echter aanzienlijk lager door het buigen van de draadjes. Wij bespreken ook een aantal experimenten met als doel het frequentieverdubbelingssignaal dat gegenereerd wordt in het substraat te onderscheiden van het signaal dat gegenereerd wordt in de nanodraadjes die korter zijn dan de coherentielengte. Helaas is het niet gelukt deze twee bijdragen te onderscheiden.

Hoofdstuk 3 gaat over de fabricage van vrijstaande, tweedimensionale platen van fotonisch kristal met een vierkant gatenrooster in een ~ 150 nm dikke plaat van $Al_{0.35}Ga_{0.65}As$. De in dit hoofdstuk onderzochte preparaten hebben gaten met een straal van $r \sim 150$ nm, een roosterconstante $a = 890$ nm, en een oppervlakte van $\sim 300 \times 300$ μm^2. De vrijstaande platen worden ondersteund door een GaAs-substraat. De lineaire optische eigenschappen van deze systemen worden onderzocht door de reflectiespectra te meten als functie van de invalshoek. Deze spectra vertonen dispersieve, asymmetrische curves bovenop een langzaam oscillerende achtergrond. We kunnen deze curves door middel van het Fanomodel uitleggen. In dit model veroorzaakt de interferentie tussen een rechtstreekse (niet-resonante) en een indirecte (resonante) bijdrage de asymmetrische curve van het spectrum. De rechtstreekse bijdrage komt door de Fresnelreflectie van het invallende licht aan de plaat, en de resonante bijdrage komt door de koppeling van het invallende licht aan een lekkende geleide mode via diffractie aan het rooster. Door het Fanomodel te gebruiken, is het mogelijk om de dispersierelatie en de kwaliteitsfactor van de resonantie te verkrijgen uit de experimentele reflectiespectra. De niet-lineaire optische eigenschappen van de fotonische kristallen worden onderzocht door de niet-lineaire reflectiespectra te meten als functie van de hoek van inval. Wij tonen aan dat de resonante koppeling van een laserpuls bij een golflengte van 1.535 μm het frequentieverdubbelingssignaal aanzienlijk kan versterken. Wij meten een versterking van de frequentieverdubbeling van meer dan 4500 keer, vergeleken met de niet-resonante bijdrage, wanneer de bundel van laserpulsen zo ingesteld wordt dat hij resoneert met een van de lekkende modes van de structuur.

Vrijstaande platen van fotonisch kristal zijn niet vlak; ze buigen doordat de roosters van het $Al_{0.35}Ga_{0.65}As$-materiaal van de plaat en het GaAs-substraat net niet (op 0.05% na) op elkaar aansluiten. In hoofdstuk 4 presenteren we een nieuwe techniek om een vrijstaande plaat van fotonisch kristal over te brengen op een transparante laag gel. In tegenstelling tot de vrijstaande structuren, zijn de zo overgebrachte structuren bijna altijd vlak. Het belangrijkste is dat de resonanties in de gemeten reflectiespectra van een structuur op gel veel zichtbaarder zijn dan die van een vrijstaande structuur. Daardoor zijn de overgebrachte structuren veel bruikbaarder voor het onderzoek aan de resonante koppeling van licht aan de platen van fotonisch kristal. Daarbij onderzoeken we ook in meer detail een ontweken kruising tussen twee modes in de experimentele transmissiespectra. Bij de ontweken kruising krijgt één van de modes een lange levensduur (wordt subradiant) en de andere mode een korte (superradiant). Voor de subradiante mode meten we kwaliteitsfactoren tot aan $Q = 300$. Deze waarde wordt beperkt door de eindige grootte van de structuur, wat suggereert dat de platen van fotonisch kristal die overgebracht zijn op het gelsubstraat van uitstekende optische kwaliteit zijn.

De lineaire reflectie- en transmissiespectra van een tweedimensionale plaat van fotonisch kristal bestaan uit asymmetrische Fanocurves door de resonante koppeling van licht aan lekkende modes van het fotonisch kristal door diffractie aan het fotonisch rooster. De koppeling van een continuüm aan modes aan een enkel resonant kanaal leidt tot interferentie tussen het directe (niet-resonante) en het indirecte (resonante) kanaal. Dit wordt beschreven door het Fanomodel. De algemeen geaccepteerde interpretatie is dat het teken van een reële parameter q van het Fanomodel de asymmetrie van de curve bepaalt voor een systeem zonder verliezen. Voor een symmetrische lucht-plaat-lucht structuur zonder verliezen verandert het teken van q als de amplitudereflectiecoëfficiënt van de directe bijdrage door nul gaat. Als gevolg daarvan kan de asymmetrie van de Fanocurve in het reflectiespectrum voor p-gepolariseerd licht worden gespiegeld door de hoek van inval voorbij de Brewsterhoek in te stellen, in het symmetrische systeem. In hoofdstuk 5 laten we zien dat het ook mogelijk is om de asymmetrie van de Fanocurve door de hoek in te stellen zonder aan de voorwaarde van nul amplitude te voldoen, voor een asymmetrische lucht-plaat-gel structuur zonder verliezen. Dit vereist echter een complexe parameter q en toont aan dat de interpretatie van een reële q die de asymmetrie bepaalt niet volledig is. Nog belangrijker is dat dit aantoont dat een Fano-achtige resonantie die gekarakteriseerd wordt door een complexe q niet noodzakelijk wijst op microscopische processen van decoherentie en/of defasering.

In hoofdstuk 6 wordt in meer detail ingegaan op frequentieverdubbeling

in platen van fotonisch kristal overgebracht op een gelsubstraat. In tegenstelling tot hoofdstuk 3, gebruiken we een gecollimeerde laserbundel, en we meten het doorgelaten frequentieverdubbelingssignaal in plaats van het gereflecteerde als functie van de hoek van inval. Vergeleken met hoofdstuk 3 gaan we een stap verder in het begrijpen hoe belangrijk de lekkende modes zijn voor het niet-lineaire proces van frequentieverdubbeling, bij zowel de grond- als de verdubbelde frequentie. De belangrijkste verschijnselen van het experimentele frequentieverdubbelingssignaal worden verklaard aan de hand van een betrekkelijk eenvoudige gekoppelde-modetheorie. In tegenstelling tot volledige numerieke berekeningen, biedt ons model inzicht in het fysisch mechanisme dat eraan ten grondslag ligt. Bovendien maakt het model geen aannames over de parameters van een ideale plaat van fotonisch kristal. In plaats daarvan gebruikt het zowel de gemeten dispersierelaties en de kwaliteitsfactoren van de relevante modes als het gemeten niet-resonante frequentieverdubbelingssignaal. Hierdoor is het model toepasbaar op niet-ideale structuren met een eindige grootte en een aantal fabricagedefecten. Bij loodrechte inval koppelen de velden van zowel de grond- als de verdubbelde frequentie resonant aan de lekkende modes van de structuur, en we meten een versterking van de frequentieverdubbeling tot aan 10000 keer zo groot vergeleken met de niet-resonante bijdrage. Bovendien laten de metingen op overtuigende wijze het effect zien van de resonante koppeling van de frequentieverdubbelde golf aan een lekkende mode van de structuur. De hoekbreedte van het gemeten frequentieverdubbelingssignaal is een factor 1.6 kleiner dan de breedte die zou volgen uit de lineaire optische eigenschappen van de lekkende mode bij de grondfrequentie. Nog duidelijker zijn de twee bijkomende zijpieken die verschijnen bij hoeken van inval van $\pm$ 9.1°. Deze zijpieken kunnen worden verklaard door de resonante koppeling te beschouwen van zowel de grondfrequentiebundel als de frequentieverdubbelde bundel aan de lekkende modes van de plaat. Dit verklaart de versmalde hoek van het gemeten frequentieverdubbelingssignaal bij loodrechte inval en de twee zijpieken, en toont het belang aan van een dubbele resonantievoorwaarde voor efficiënte frequentieverdubbeling in een fotonisch kristal.

Curriculum Vitæ

Ljubiša Babić was born on the 1ˢᵗ of April 1982 in the city of Dubrovnik, Croatia. In the period between 1997 and 2001, he attended the Gymnasium Ivan Goran Kovačić in Herceg Novi, a coastal town in Montenegro. During that time he became interested in physics winning the first place in the Montenegrin National Physics Olympiad two times in a row, in 1998 and 1999. In 2001, he entered the Faculty of Electrical Engineering of the University of Belgrade in Serbia and enrolled in the Master's program. For his Master's research project Ljubiša investigated theoretically the electronic transport in a p-n junction made in gallium arsenide. The research was carried out in the Department of Physical Electronics under supervision of Prof. Dr. P. Matavulj and Prof. Dr. J. Radunović.

In Belgrade he became very interested in the physics of nanostructures, in particular their electronic and optical properties. Therefore, he decided to continue his education abroad and learn more about experimental research in the field of photonics. In September 2006, he started his Ph.D. research in experimental physics in the Quantum Optics Group at Leiden University under supervision of Dr. M. J. A. de Dood and Prof. Dr. J. P. Woerdman. The aim of the research was to experimentally investigate linear and nonlinear optical properties of semiconductor III-V photonic crystals and nanowires. Ljubiša fabricated photonic crystals in the Kavli Nanolab Delft, whereas the nanowire samples were fabricated in the facilities of Philips Research. The results of the research are presented in this thesis.

List of publications

Journal articles

- Lj. Babić and M. J. A. de Dood, *Interpretation of Fano lineshape reversal in the reflectivity spectra of photonic crystal slabs*, Opt. Express **18**, 26569–26582 (2010). (*Chapter 5 of this thesis*)

- Lj. Babić, R. Leijssen, E. F. C. Driessen, and M. J. A. de Dood, *Method to transfer photonic crystals to a transparent gel substrate*, in preparation. (*Chapter 4 of this thesis*)

- Lj. Babić, L. T. H. van Dellen, and M. J. A. de Dood, *Second harmonic generation in transmission from photonic crystals on a gel substrate*, in preparation. (*Chapter 6 of this thesis*)

Conference proceedings

- Lj. Babić, P. Matavulj, and D. Radunović, *Analysis of fast transient processes during formation of the pn junction made of a two-valley semiconductor*, Proceedings 50th ETRAN Conference, Vol. IV, p. 80 (2006).

- M. J. A. de Dood and Lj. Babić, *Leaky Modes of Two-Dimensional Photonic Crystals Transferred to a Low Refractive Index Substrate*, in Frontiers in Optics, OSA Technical Digest (CD) (Optical Society of America, 2010), paper FThJ6. (*Chapters 4 and 5 of this thesis*)

- Lj. Babić and M. J. A. de Dood, *Fano lineshape reversal in the reflectivity spectra of photonic crystals transferred to a gel substrate*, Proceedings Annual Symposium of the IEEE Photonic Benelux Chapter, p. 53 (2010). (*Chapters 4 and 5 of this thesis*)

Acknowledgements